Marius Hornnes

Application of the Theory of Critical Distances for Fatigue Assessment of Notched Additively Manufactured Inconel 718

Master's thesis in Mechanical Engineering
Supervisor: Filippo Berto
June 2019

Master's thesis

NTNU
Norwegian University of
Science and Technology

Marius Hornnes

Application of the Theory of Critical Distances for Fatigue Assessment of Notched Additively Manufactured Inconel 718

NTNU

Norwegian University of
Science and Technology

Preface

This Master's thesis was written in the spring of 2019 at the Department of Mechanical and Industrial Engineering at the Norwegian University of Science and Technology. The thesis is a part of the M.Sc. program in Mechanical Engineering with specialization in Product Development and Materials Engineering. The work in this thesis builds on the specialization project "Structural Integrity of Additively Manufactured Inconel 718", conducted in the fall of 2018.

Marius Hornnes

Trondheim, June 2019

Acknowledgement

I would like to thank my supervisor professor Filippo Berto at the Norwegian University of Science and Technology for helping me shape the task, as well as giving me the freedom to work independently. I am thankful for having received valuable guidance and feedback during the course of this work.

I would also like to thank my co-supervisor, Ph.D student Klas Solberg at NTNU, for supporting me in my lab work and for always being available when I have needed assistance and guidance.

Abstract

Inconel 718 is a nickel based superalloy well suited for high temperature and corrosive environments. However, the material properties of Inconel 718 also makes it difficult to manufacture complex parts using conventional methods, making alternative production methods a relevant topic. Additive Manufacturing (AM), or 3D printing, is a production approach whose popularity has increased rapidly in recent years. It allows for the production of components with intricate geometries that cannot be produced with conventional manufacturing methods, effectively giving the designers more freedom in the development process. The complex geometries produced by AM will often contain notches, which can lead to a reduction of the structural integrity of the part. The Theory of Critical Distances (TCD) is a group of methods used for design and assessment of notched components, that utilizes a material length parameter, L, referred to as the critical distance. With reference to the critical distance, the linear-elastic stress fields at the vicinity of the stress raising features are used to predict both brittle and fatigue failure.

In this work, two TCD approaches were evaluated in terms of their applicability for fatigue assessment of notched as-built Inconel 718 specimens produced by Selective Laser Melting (SLM). This was done based on fatigue data of four different specimen geometries taken from literature. The results revealed promising accuracy when predicting the fatigue limit, with an absolute error bellow 20 %. One of the TCD approaches was also used to modify the fatigue data of three notched specimens, giving a resulting combined fatigue plot with little scatter. This modified fatigue data was discussed in terms of its applicability for fatigue assessment. In addition, fatigue testing of heat treated specimens was performed to investigate the effect of heat treatment on the critical distance of the material. The results showed that the heat treatment had a clear effect at lower number of cycles to failure, and that this effect decreased with increasing number of cycles to failure.

After obtaining promising results when applying the two TCD approaches on the AMed Inconel 718 specimens, an engineering approach based on the TCD was proposed. The engineering approach was presented as an alternative procedure for acquiring the stresses at a distance from the stress raising features present in a given component. Some possible applications of the procedure were also suggested, including fatigue assessment, critical region identification and design decision making. Finally, some limitations and a possible improvement of the procedure were presented and discussed.

Sammendrag

Inconel 718 er et materiale som er velegnet til bruk ved høye temperaturer og i korrosivt miljø. Materialet har i tillegg egenskaper som gjør det vanskelig å produsere komponenter med komplekse geometrier ved bruk av konvensjonelle produksjonsmetoder. Dette gjør det relevant å benytte alternative produksjonsmetoder for å produsere Inconel 718-komponenter. Additiv tilvirkning, eller 3D-printing, er en fellesbetegnelse på en gruppe produksjonsteknikker som har utviklet seg raskt de siste årene. 3D-printing gjør det mulig å produsere strukturer og komponenter med kompliserte geometrier som ikke kan produseres med konvensjonelle produksjonsmetoder. Disse komplekse geometriene gir designere større frihet i utviklingsprosessen, men kan ofte inneholde kjerver som reduserer den strukturelle integriteten til komponenten. Theory of Critical Distances (TCD) er en guppe med metoder som brukes til å vurdere egenskapene til komponenter som inneholder kjerver, og baserer seg på en lengdeparameter, L, som kalles materialets kritiske avstand. Metodene benytter seg av spenningsfeltene i bunnen av spenningskonsentrasjonene, samt den kritiske avstanden til materialet, og kan brukes til å predikere sprøbrudd eller utmattingsbrudd.

I denne oppgaven ble to TCD-metoder evaluert med tanke på deres egnethet til å vurdere utmattingsegenskapene til additivt tilvirkede Inconel 718-deler med kjerver, produsert med selektiv lasersmelting (SLM). Dette ble gjort basert på utmattingsdata av fire forskjellige prøvestykke-geometrier, hentet fra literaturen. Resultatene viste lovende nøyaktighet med tanke på å anslå utmattingsgrensen, med en feilmargin under 20 %. En av TCD-metodene ble også brukt til å modifisere utmattingsdataene til tre av prøvestykkene som inneholder kjerver. Dette resulterte i et samlet utmattingsplott med lite spredning. Muligheten for å bruke dette utmattingsplottet til å vurdere utmattingsegenskapene til Inconel 718 ble duskutert. I tillegg ble det gjennomført utmattingstesting av varmebehandlede prøvestykker med den hensikt å studere effekten av varmebehandling på materialets kritiske avstand. Resultatene viste at varmebehandlingen hadde stor effekt ved lavt antall lastsykluser, og at denne effekten avtok med høyere antall lastsykluser.

Etter å ha oppnådd lovende resultater ved å bruke de to TCD-metodene på utmattingsdata for 3D-printet Inconel 718, ble det foreslått en alternativ TCD-basert metode for å studere spenningene ved en avstand fra spenningskonsentrasjoner i en gitt komponent. Denne alternative metoden er ment som et ingeniør-verktøy for å gjøre det lettere å bruke TCD-prinsipper til praktiske formål. Noen mulige bruksområder for metoden ble presentert og diskutert. Disse bruksområdene innebærer utmattingsvurdering av komponenter, identifisering av kritiske regioner i komponenter og som grunnlag for design-avgjørelser. Til slutt ble noen begrensninger ved metoden samt en mulig forbedring presentert og diskutert.

Abbreviations and Nomenclature

Abbreviations

AM	=	Additive Manufacturing
DED	=	Direct Energy Deposition
DMLS	=	Direct Laser Metal Sintering
EBM	=	Electron Beam Melting
FCG	=	Fatigue Crack Growth
FEA	=	Finite Element Analysis
FEM	=	Finite Element Method
HCF	=	High Cycle Fatigue
HIP	=	Hot Isostatic Pressing
LCF	=	Low Cycle Fatigue
LED	=	Linear Energy Density
LEFM	=	Linear Elastic Fracture Mechanics
LM	=	Line Method
LPBF	=	Laser Powder Bed Fusion
NSIF	=	Notch Stress Intensity Factor
PBF	=	Powder Bed Fusion
PM	=	Point Method
SEM	=	Scanning Electron Microscope
SIF	=	Stress Intensity Factor
SLM	=	Selective Laser Melting
TCD	=	Theory of Critical Distances
VED	=	Volume Energy Density

Nomenclature

δ	$=$	Delta Phase
$\Delta\sigma$	$=$	Stress Range
$\Delta\sigma_0$	$=$	Critical Stress Range
$\Delta\sigma_{eff}$	$=$	Effective Stress Range
ΔK	$=$	Stress Intensity Range
ΔK_{th}	$=$	Fatigue Crack Growth Threshold
γ	$=$	Gamma Phase
γ'	$=$	Gamma Prime Phase
γ''	$=$	Gamma Double Prime Phase
ϵ	$=$	Strain
θ	$=$	Angle
σ	$=$	Stress
σ_0	$=$	Critical Stress
σ_a	$=$	Stress Amplitude
σ_{eff}	$=$	Effective Stress
σ_{max}	$=$	Maximum Stress
σ_{min}	$=$	Minimum Stress
σ_m	$=$	Mean Stress
σ_{UTS}	$=$	Ultimate Tensile Strength
σ_{YS}	$=$	Yield Strength
E	$=$	Young's Modulus
K	$=$	Stress Intensity Factor
k_f	$=$	Fatigue Notch Factor
K_{IC}	$=$	Fracture Toughness
k_t	$=$	Stress Concentration Factor
L	$=$	Critical Distance Value
N_f	$=$	Number of Cycles to Failure
R	$=$	Load Ratio
r	$=$	Polar Coordinate Distance

Contents

1 Introduction

1.1 Background

Inconel 718 is a nickel based superalloy with properties that makes it an attractive material for applications prone to high temperatures and corrosion [1]. The material has high strength and good corrosion resistance at both elevated and room temperature, and it is the preferred material for certain components in the aerospace, nuclear, and petrochemical industry. However, Inconel 718 also exhibits properties which makes it difficult to manufacture parts of complex geometries using conventional machining methods. For this reason, additive manufacturing (AM) of Inconel 718 is a relevant topic. Additive manufacturing is a production approach that has advanced rapidly in the recent years. AM gives the designers freedom to manufacture complex parts that cannot be produced by conventional production methods. However, additively manufactured (AMed) components have certain drawbacks in terms of mechanical properties when compared to those manufactured by conventional methods. This especially applies for components subjected to repeated loads, where fatigue strength is the deciding factor. Poor surface finish and the presence of defects stemming from the AM process, serve as initiation sites for fatigue failure. The production of complex geometries enabled by AM technology are also likely to introduce geometric features such as notches, whose behavior have to be determined. Having suitable fatigue assessment approaches for determining the fatigue life of AMed components is important.

The Theory of Critical Distances (TCD) [2] is a set of approaches used for design and assessment of notched components subjected to static or fatigue loading. In terms of accuracy, the TCD has been shown to yield promising results. The approaches are based on the linear elastic stress fields at the vicinity of the stress raiser, and uses a material length parameter, L, referred to as the critical distance, for determining the severity of the stress situation. With today's availability of commercial FE software, the stress fields can be easily obtained by creating node paths in the critical regions of the component to be assessed. However, identification of the critical regions can in some cases be a challenging task, leading to potential difficulties when determining the locations of the node paths. For this reason, investigating alternative approaches for obtaining these stresses is a relevant topic.

1.2 Problem Description / Project Scope

The main goal of this thesis is to determine the applicability of the TCD for fatigue assessment of notched AMed Inconel 718 specimens, as well as proposing an alternative engineering approach based on the TCD. The alternative approach should serve as a convenient engineering tool that can be used for design and assessment purposes.

1.3   Approach

In order to evaluate the applicability of the TCD for fatigue assessment, two slightly different TCD approaches will be used based on experimentally obtained fatigue data of AMed Inconel 718 specimens. The specimens include four different geometries produced in the same batch, where some of them were heat treated and some were kept as-built from the AM process. The fatigue results of the as-built specimens were taken from literature, while the fatigue results of the heat treated specimens were obtained by tests conducted in this work. In addition, the difference in post-processing of the test-specimens allows for an investigation of the effect of heat treatment on the critical distance.

1.4   Literature

In this thesis, the literature used is mainly based on three different types of sources. These sources include scientific papers, text books, and the specialization project [3] conducted in the fall of 2018. Parts of the specialization project are included because the thesis is a continuation of the specialization project, and some of the content is still relevant for the thesis. In addition, some sections in the thesis are based entirely on one particular reference. For these cases, the respective reference is cited at the beginning of the section.

1.5   Structure of the Thesis

The rest of the thesis is divided into the following chapters:

Chapter 2 presents the basic concepts of additive manufacturing, with main focus on metals.

Chapter 3 consists of the fundamental theory considered most relevant for this thesis. The theory includes an overview of static and fatigue properties of materials, as well as some concepts related to fracture mechanics. A short introduction to the finite element method is also provided, before the TCD is explained. A brief literature review of the TCD is also included.

Chapter 4 includes an explanation of the properties and microstructure of Inconel 718. The most common heat treatment processes for Inconel 718 are also explained.

Chapter 5 contains a literature review of the static and fatigue properties of AMed Inconel 718. This chapter is included primarily to provide a better understanding of the properties and behavior of the material in question.

Chapter 6 presents the specimens used for the experimental testing, as well as an explanation of how the fatigue tests were carried out. Static tests are included in addition to the fatigue tests, in order to get an understanding of the static properties of the material.

Chapter 7 presents the results from the tests described in chapter 6.

Chapter 8 includes the TCD calculations based on the fatigue data of as-built and heat treated Inconel 718. The chapter contains both an explanation of the procedures, as well the obtained results. First, the fatigue data taken from literature is presented together with the numerical calculations. Then, two TCD approaches are used to determine the critical distance of the material. The critical distance-determination is then used to make fatigue limit predictions, as well as modifying the fatigue data as a basis for fatigue assessment based on the TCD. Finally the two TCD approaches are used to investigate the effect of heat treatment on the critical distance of Inconel 718.

Chapter 9 presents a proposed engineering approach based on the TCD. The approach is explained in detail and the steps are visualized and described in Appendix A.

Chapter 10 includes a discussion of the procedures and findings from chapter 8, as well as a discussion of some possible applications and the limitations of the approach described in chapter 9.

Chapter 11 contains the conclusion of the thesis together with recommendations for further work.

2 Additive Manufacturing

This chapter includes an overview of AM as a manufacturing method, as well as a more detailed description of some specific AM methods relevant for this work.

2.1 Introduction to Additive Manufacturing

Additive manufacturing is a manufacturing approach highly applicable when creating complex three-dimensional parts. Due to the significant nature of the process, it does not have the geometry limitations of the conventional manufacturing methods, such as those for casting or extruding. The AM process benefits from the advantages related to building parts layer-by-layer, and it does not require setting up machines or creating tools or molds for production of different parts. This makes AM suitable for a just-in-time production approach, or for producing prototypes and mock-ups. All parts produced by AM are based on digital models that are designed using a software, and then uploaded to the AM production system.

Additive manufacturing can be used for a wide range of materials, and there are several different AM methods available. Some methods are based on fusing solid materials, while others solidify parts from inside of a liquid.

2.2 Additive Manufacturing of Metals

For additive manufacturing of metals, there are mainly four categories of methods available; Powder Bed Fusion (PBF), Direct Energy Deposition (DED), Binder Jetting, and Sheet Lamination [4]. Both PBF and DED have several sub-categories of the manufacturing methods available, while binder jetting and sheet lamination are exclusive methods. Binder jetting uses a liquid binding agent to join the powder-based material together. The binding agent fuses one layer of material, and a new layer of powder is added for the next fusing step to take place. In figure 2.1, a typical setup for the Binder Jetting process is shown. Powder is fed layer-by-layer into the powder bed, from the powder stock, by means of the powder roller. Once the new layer of powder is added to the powder bed, the liquid binder fuses the desired parts of the new layer. Sheet lamination uses different techniques in order to join sheets of material in a layer-by-layer manner. The layers can be given the desired shape before joining or they can be machined once they are added to the build. Figure 2.2 shows a typical setup for the sheet lamination process. In this case, sheets are fed into the build by means of spools and cut into shape using a laser, and the fusing mechanism is ultrasonic welding. Other fusing methods, such as heating or the use of fusing agents, can also be employed.
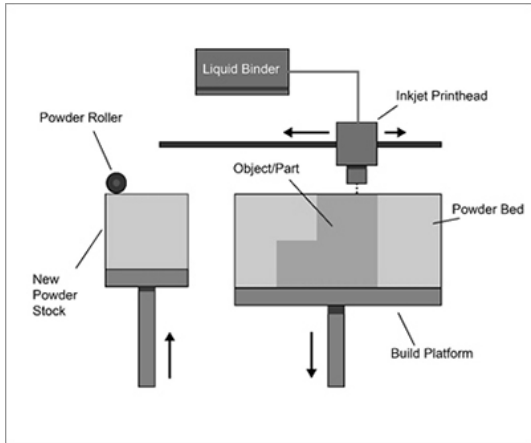
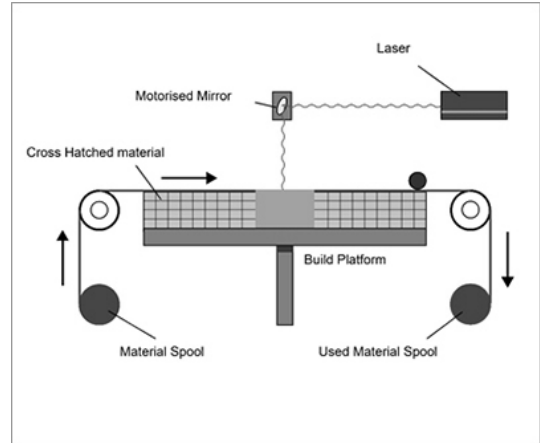**Figure 2.1:** Illustration of the Binder Jetting setup [5].

Figure 2.2: Illustration of the Sheet Lamination setup [6].

The difference between PBF and DED essentially lies in the method of material supply. In PBF, the powder is placed in a container, while a heat source fuses together the powder at the desired locations inside the powder-bed, as illustrated in figure 2.3. For DED, the material can be in both powder and wire form, and is continuously fed through a nozzle and joined as it leaves the feeding mechanism, as illustrated in figure 2.4. Both PBF and DED come with a set of possible configurations and process parameters, with some of them being; type of heat source, material type and form, pre-heating temperature, printing environment, and heat input.
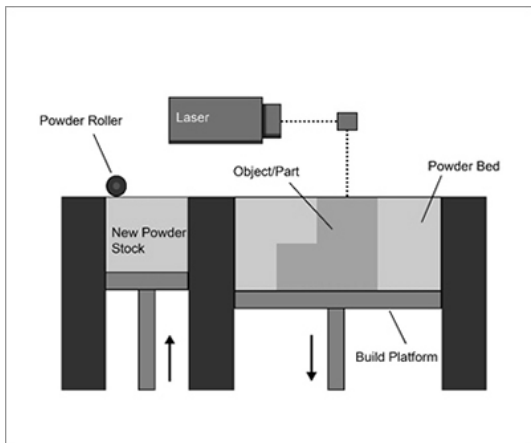

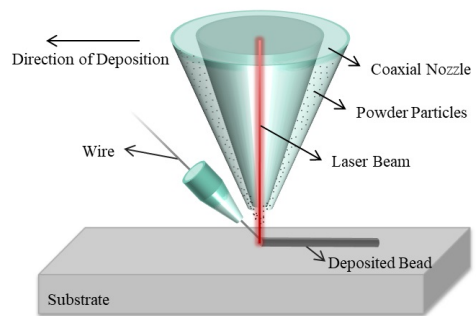**Figure 2.3:** Illustration of a PBF setup utilizing a laser [7].

Figure 2.4: Illustration of a DED setup utilizing a laser [8]. The raw material can be either wire or powder, as illustrated.

Three common PBF methods for additive manufacturing of Inconel 718 are selective laser melting (SLM), direct laser metal sintering (DMLS) and electron beam melting (EBM) [9]. Both SLM and DMLS utilizes a laser in order to fuse the metal powder, and uses a similar setup as the one in figure 2.3. Since both SLM and DMLS uses a laser to fuse the powder, they are often referred to as laser powder bed fusion (LPBF) methods. The main difference between the two methods is the fusing-mechanism. For SLM, the laser completely melts the powder in order to fuse it, while DMLS only sinters the particles to complete the part. The main advantage of DMLS is that it creates parts with no residual

stress, while SLMed parts has the advantage of being very dense and strong [10]. Electron beam melting does not use a laser in order to fuse the powder. Instead, an electron beam is used to melt the metal powder. This is done inside a vacuum chamber and with metal powder heated to high temperatures [11]. Vacuum is used in order to avoid energy loss from collisions between electrons and gas molecules.

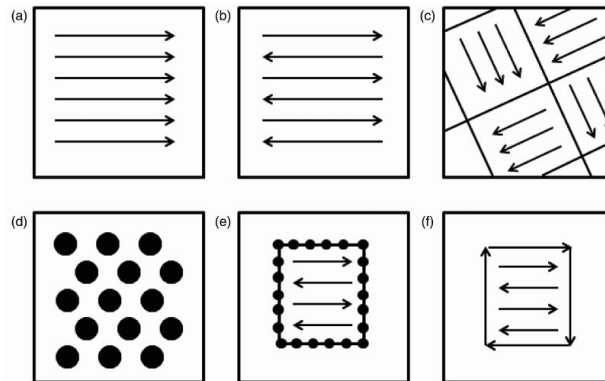## 2.3 Printing Pattern and Parameters

Figure 2.5: Scanning pattern for AM [12]. (a) unidirectional hatching, (b) bi-directional hatching, (c) island scanning, (d) spot melting, (e) spot melting contours with bi-directional hatching, and (f) line contouring with bi-directional hatching.

When printing a component, there are several ways of adding a new layer to the build. Figure 2.5 shows some common patterns for how a new layer can be added to the part. The outer lines are called contours, while hatching patterns are used inside the contours. Hatching patterns come in a large variety of configurations.
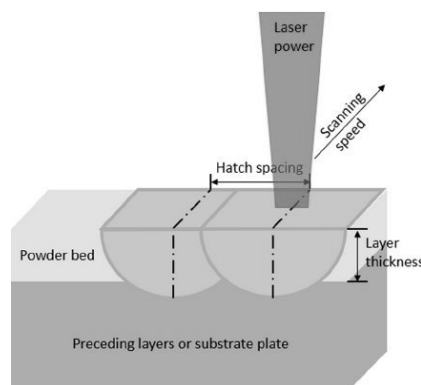

Figure 2.6: Hatching lines [13].

For laser powder bed fusion (LPBF), there are several parameters to be decided when adding a new layer to the build. The thickness of the layers (t), distance between the hatching-lines (h), laser power (P), and scanning speed (v) are all important parameters to be determined. Figure 2.6 illustrate these parameters. Volume energy density (VED) is a variable that includes the parameters, and describes the energy input from the scanning.

VED is defined in equation 2.1 [14]. Only considering laser power and scanning speed gives the linear energy density (LED), that is defined in equation 2.2.

$$VED = \frac{P}{v \cdot h \cdot t} \tag{2.1}$$

$$LED = \frac{P}{v} \tag{2.2}$$

2.4   Additive Manufacturing Defects and Limitations

Defects stemming from the additive manufacturing process can be detrimental to the performance and quality of the printed part. The defects can reduce the density of the part and at the same time act as stress raisers. For this reason, it is crucial that the correct parameters for the printing process are selected. The most common defects include [15]:

- **Gas Pores**
  Spherical gas pores can be found inside the printed part, and occurs as a consequence of trapped gases

- **Keyhole Pores**
  Keyhole pores are steep and deep melt pools that occurs at the start and end points of the scan tracks, or if the LED is too high

- **Lack-of-fusion**
  Lack-of-fusion defects appear as elongated pores between the printed layers, and the length of the pores is perpendicular to the build direction. Lack-of-fusion defects are caused by insufficient energy input unable to melt all the powder

- **Unstable Melt Pool**
  An unstable melt pool leads to the formation of irregular pores. This occurs at low scanning speeds with high energy density and at high scanning speeds. These two situations lead to hydrodynamic instability of the melt pool and instability of melt flow, respectively

- **Lack of Overlap**
  In order to obtain a high density of the printed part, the overlap between the hatching lines must be sufficiently large. Too large hatch space will cause porosity between the hatching lines

Overhang Surface
Additive manufacturing of components with overhang surfaces can be challenging and effectively reduce the design freedom of the component to be produced. Referring to figure 2.7, printing of surfaces with small overhang angles, α, can lead to high surface roughness [16, 17]. A high surface roughness can be crucial to the performance of the component, and can lead to the need for machining of the surface in order to obtain a sufficiently good surface finish. In some cases, supporting structures that have to be removed after the manufacturing process may be necessary for printing large overhangs.
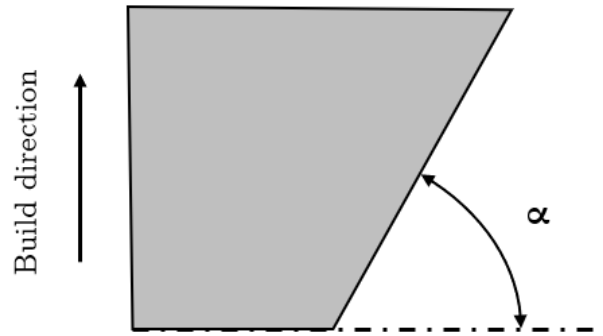
Figure 2.7: Overhang angle, α.

Residual Stresses

The significant nature of the AM process of metals can introduce residual stresses in the printed component, leading to inferior performance. If the printing operation involves complete melting of the material, residual stress can form as a result of the thermal cycle of the process [18]. The thermal cycle involves rapid heating, rapid solidification and re-melting of underlying layers in addition to the melting of the top layer. As for the EBM and SLM processes, components produced by EBM has significantly lower residual stresses than those produced by SLM [18]. This is due to the high preheating temperature of the powder in the EBM process, which causes lower cooling rates in the solidification step.

3 Theoretical Background

In this chapter, some of the fundamental theory relevant for this work is presented. In some sections, the included theory is entirely based on one text book. In these cases, the reference is given at the start of the section. Otherwise, references are included in the text.

3.1 Tensile Properties

The theory in this section is based on Norman E. Dowling's book Mechanical behavior of materials: Engineering methods for deformation, fracture, and fatigue [19].

When a material is subjected to a given stress, the material's response is strain. This strain is a measure of deformation and can be both elastic and plastic, depending on material properties and the amount of stress applied. The relationship between applied stress and resulting strain is often plotted as a stress-strain curve, revealing the behavior of the material.

For elastic deformation, the deformation is recovered upon unloading, and stress and strain are often proportional, resulting in a linear stress-strain curve. The proportional relationship of stress and strain is described by Hooke's law $\sigma = E\epsilon$, and introduces the modulus of elasticity, or Young's Modulus, E, which is a material constant that represents the slope of the linear region. The Young's Modulus is thus a measure of the material's resistance to elastic deformation. After the linear response of the material, when the yield strength, σ_{YS}, of the material is reached, the material will deform plastically. The plastic deformation of the material is not recoverable upon reloading and the relationship between stress and strain is no longer linear. The plastic region of the stress-strain curve is usually characterized by a decreasing slope, meaning that less stress is needed to further deform the material.
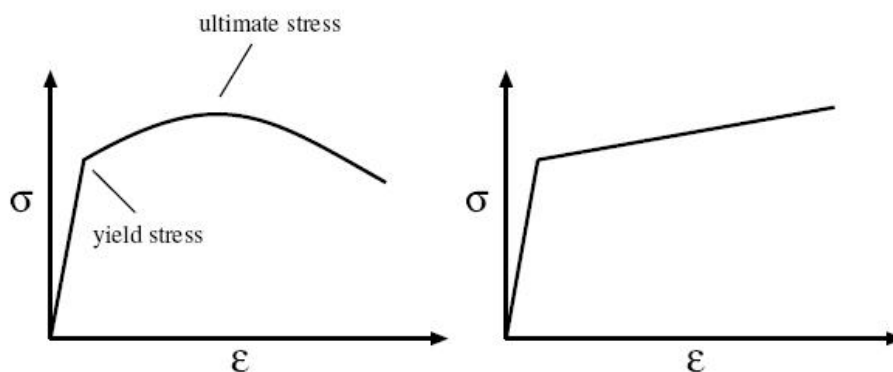

Figure 3.1: Engineering stress-strain (left) and true stress-strain (right) [20].

Figure 3.1 shows two different stress-strain curves. The left curve in shows the engineering

stress-strain response, where material behavior is calculated based on the assumption of a constant cross section throughout the loading process. The ultimate tensile strength of the material, σ_{UTS}, is the point of highest stress on the engineering stress strain curve, whereas the yield strength indicates the transition between elastic and plastic deformation. On the right is the true stress-true strain curve, where material behavior is calculated accurately, considering the reduction of the cross section. When the material reaches the true fracture strength, σ_f, final fracture will occur.

3.2 Fatigue Properties

The theory in this section is based on Norman E. Dowling's book Mechanical behavior of materials: Engineering methods for deformation, fracture, and fatigue [19].

When a component is subjected to a cyclic load, the possibility of failure due to fatigue occurs. The repeated load can be harmful even if the stress caused by it is well below the ultimate strength of the material. Accumulation of the microscopic damages caused by the repeated load can develop into a crack or macroscopic damage that leads to failure of the component. The fatigue strength of a material describes how many cycles to failure the material can withstand before failure, at a given stress amplitude.

In figure 3.2, a representation of two different loading conditions is provided. The curves indicate how the applied stress changes with time, and maximum stress (σ_{max}), minimum stress (σ_{min}), and mean stress σ_m , are indicated. Stress range is given as $\Delta\sigma=\sigma_{max}$ - σ_{min}, and stress-amplitude is $\sigma_a=\sigma_{max}$ - σ_m. The load ratio, R, is defined as the ratio between minimum stress and maximum stress: R=$\sigma_{min}/\sigma_{max}$. For the load situation on the left, the load is symmetrical to the time-axis, hence, the load ratio is R=-1 and σ_m=0. With an increasing tension mean stress, the load ratio will increase, such as in the load situation to the right in figure 3.2.
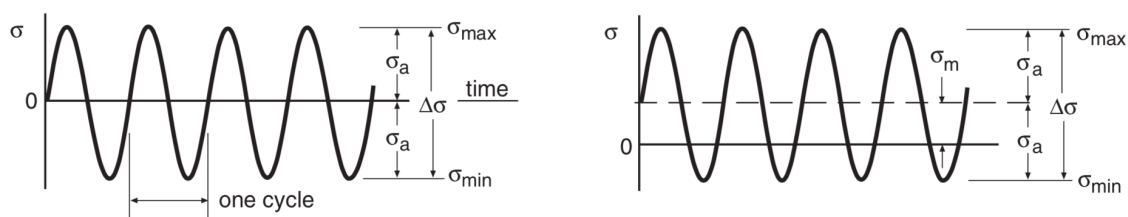

Figure 3.2: Cyclic loading.

Low Cycle Fatigue
Low cycle fatigue describes the situation where relatively few cycles leads to failure of a component. The number of cycles is in the order of tens, hundreds, or thousands, and the load is often large enough to cause a significant amount of plastic deformation. Due to the presence of plastic deformations, the strain-based approach for fatigue assessment is often applied for LCF. Strain-based approach establishes a relationship between strain amplitude and cycles to failure, presented as strain-life curves, as seen in figure 3.3. By cyclically loading between constant strain limits and measuring stress, a more detailed study of local yielding is obtained, giving an improved estimation of intermediate and

especially short fatigue lives. The approach also applies for long lives with little plasticity. A boundary value, called transition fatigue life Nt, defines the boundary between a situation involving a significant amount of plasticity (plastic curve), and a situation of little plasticity (elastic curve).
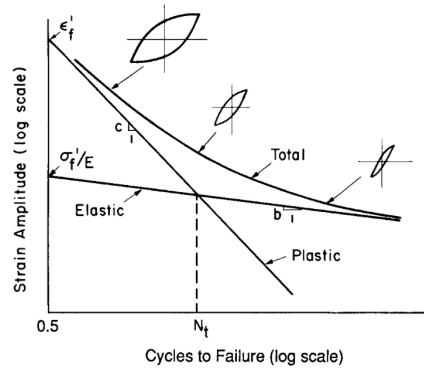

Figure 3.3: Curves for elastic, plastic, and total strain versus life [19].

High Cycle Fatigue

High cycle fatigue is one of the main failure modes in practical industry applications [21]. For components experiencing relatively small deformations that are primarily elastic, High Cycle Fatigue properties are used to determine the life of the component. The previously mentioned strain-based approach can be used to describe high cycle fatigue behavior, but the stress-based approach is more commonly used. Stress-based approach is based on the nominal stress at the affected region of the component. In order to identify the nominal stress a component can withstand, the effect of mean stress and stress raisers must be considered. By controlling the applied stress-amplitude and measuring number of cycles to failure for the component, a stress-life relationship can be established. This relationship is presented in a stress versus life curve, or S-N curve, showing the amount of cycles to failure at a given stress amplitude. Two typical S-N curves are illustrated in figure 3.4, with both linear- and log-scales. When plotting the S-N curves in log-scale, a linear trend is often seen, and the curve can be fitted with the Basquin-equation: $\sigma_a = AN_f^b$, where N_f is the number of cycles to failure at a given stress amplitude, and A and b are fitting constants. The log-plots are useful due to the high number of cycles usually involved.
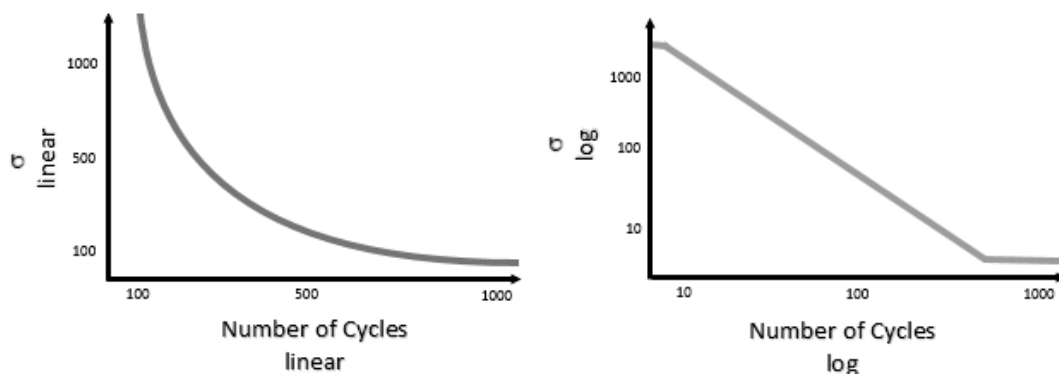

Figure 3.4: S-N curves [22].

If the component subjected to cyclic loading contains a notch, the fatigue notch factor, k_f, is introduced. The fatigue notch factor is defined as the fatigue strength of the notched member divided by the fatigue strength of the smooth member, as seen in equation 3.1.

$$k_f = \frac{\sigma_{a,notched}}{\sigma_{a,smooth}} \tag{3.1}$$

The influence of a notch can also be described by the stress concentration factor, k_t, which is defined as the local maximum stress at the notch divided by the nominal (average) stress, as seen in equation 3.2.

$$k_t = \frac{\sigma_{max}}{\sigma_{nominal}} \tag{3.2}$$

The relationship between the fatigue notch factor and the stress concentration factor is given by equation 3.3, and introduces the notch sensitivity, q. The definition of q presented in equation 3.3 is an empirical formulation proposed by R.E. Peterson, and includes a material constant α and the notch radius ρ. Other empirical formulations of q also exist.

$$q = \frac{k_f - 1}{k_t - 1} = \frac{1}{1 + \frac{\alpha}{\rho}} \tag{3.3}$$

3.3 Linear Elastic Fracture Mechanics

The theory in this section, except from the theory of the notch stress intensity factor, is based on Ted L. Anderson's book Fracture Mechanics: Fundamentals and Applications [23].

The presence of cracks, or crack-like features, can have detrimental effects on the performance of an engineering component. When a crack is present, failure by fracture can occur even at loads well below the material's yield strength, making failure difficult to predict with conventional methods. A crack can be subjected to one, or a combination of the three load-modes illustrated in figure 3.5. The modes I, II and II are referred to as opening, in-plane shear and out-of-plane shear, respectively.
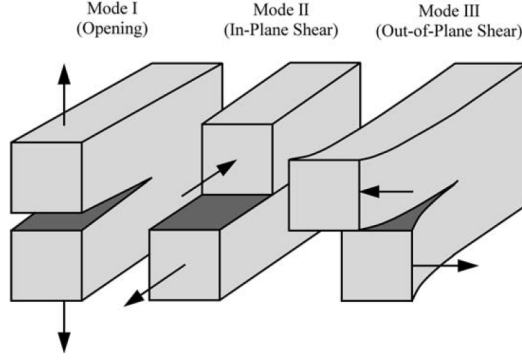
Figure 3.5: Loading modes I, II and III, from [23].

There are multiple examples of features that act like cracks. Cracks and other flaws can for example be introduced to the component during the manufacturing process in the form of porosities and inclusions, or they can form during operation in the form of deep scratches. In many situations it is difficult to avoid the presence of cracks, meaning that it is important to find a way to assess components containing cracks. This leads to the introduction of the fracture mechanics approach to failure.

In linear elastic fracture mechanics (LEFM), the stress intensity factor (SIF) K, is a value used to determine how critical the presence of a crack is. The SIF considers the crack size, geometry and stress, and it assumes a linear elastic material behavior described by Hooke's law. In the case of mode I loading of an infinite plate with W » a, where W is the plate-width and a is half of the crack length, a simple closed form solution for the SIF is given by equation 3.4. This loading situation is illustrated in figure 3.6, where σ is the applied stress and the crack is a through crack. If K_I reaches the critical SIF value K_{IC}, which is the fracture toughness of the material, then fracture will occur. In the case of other specimen geometries and loading modes, the correction factor Y can be introduced to account for these changes. Equation 3.5 shows how this factor can be applied to the original K-solution, also including all three modes.

$$K_I = \sigma\sqrt{\pi a} \tag{3.4}$$
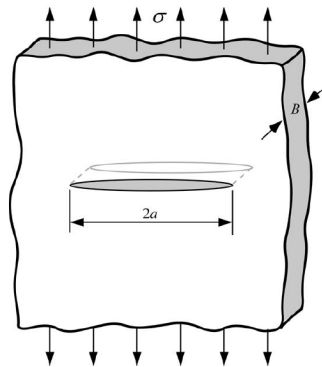
$$K_{I,II,III} = Y\sigma\sqrt{\pi a} \tag{3.5}$$

Figure 3.6: Wide plate with through crack, from [23].

Referring to the polar coordinate system illustrated in figure 3.7, the complete stress distribution at the vicinity of the notch can be calculated by knowing the SIF. In the case of mode I loading, as seen to the left in figure 3.5, the stress fields are given by equations 3.6, 3.7 and 3.8.
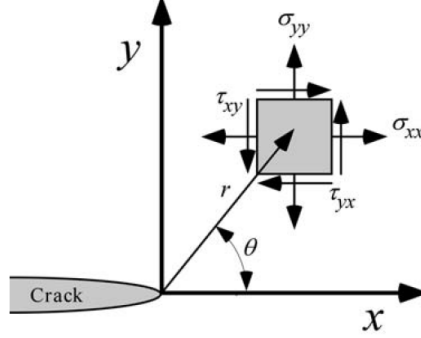

Figure 3.7: Stresses at the crack tip, from [23].

$$\sigma_{xx} = \frac{K_I}{\sqrt{2\pi r}} cos\left(\frac{\theta}{2}\right)\left[1 - sin\left(\frac{\theta}{2}\right)sin\left(\frac{3\theta}{2}\right)\right] \tag{3.6}$$

$$\sigma_{yy} = \frac{K_I}{\sqrt{2\pi r}} cos\left(\frac{\theta}{2}\right)\left[1 + sin\left(\frac{\theta}{2}\right)sin\left(\frac{3\theta}{2}\right)\right] \tag{3.7}$$

$$\tau_{xy} = \frac{K_I}{\sqrt{2\pi r}} cos\left(\frac{\theta}{2}\right)sin\left(\frac{\theta}{2}\right)cos\left(\frac{3\theta}{2}\right) \tag{3.8}$$

Notches

When working with notches, a different type of SIF is introduced, namely the notch stress intensity factor (NSIF). A method for calculating the NSIF that applies for both blunt and sharp notches, as well as cracks, was proposed by Lazzarin and Filippi [24]. The method is based on the K-formulation in equation 3.4, but it is designed to consider the geometric features of notches, such as notch radius and opening angle. For mode I loading, the NSIF is given by equation 3.9 and refers to the coordinate system in figure 3.8. The origin of the coordinate system is located at a distance r_0 from the notch tip, and r is defined as the distance from the coordinate system origin. λ_1, ω_1 and μ_1 depend on the notch opening angle, while σ_θ is the stress along the notch bisector line at the distance r from the coordinate system origin. The stress can easily be obtained using a FEA software.

$$K_{\rho,I}^V = \sqrt{2\pi} r^{1-\lambda} \frac{\left(\sigma_\theta\right)_{\theta=0}}{1 + \widetilde{\omega}\left(\frac{r}{r_0}\right)^{\mu-\lambda_2}} \tag{3.9}$$
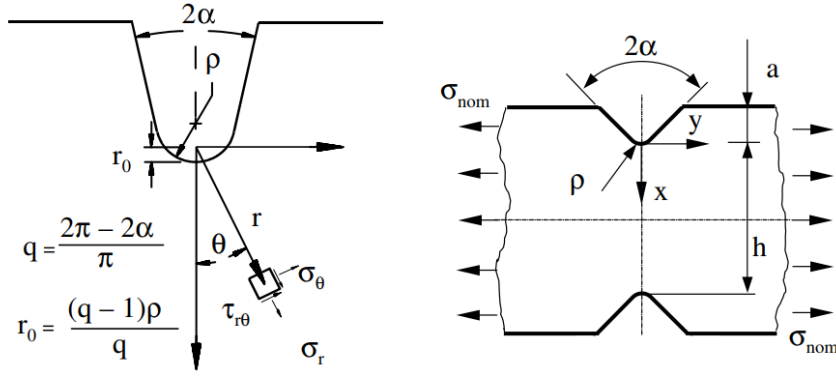
Figure 3.8: Coordinate system and parameters, from [24].

3.4 Fatigue Crack Growth

The theory in this section is based on Ted L. Anderson's book Fracture Mechanics: Fundamentals and Applications [23].

Fatigue crack growth can be considered as the fracture mechanics approach to fatigue. The method uses the stress intensity factor K given by equation 3.10, as introduced in section 3.3, and focuses on the growth of an initial flaw in the material, caused by cyclic loading. The initial flaw is small in size but can grow into a crack and then propagate until it reaches a critical size where brittle fracture will occur. By going from stress to stress range, as seen in equation 3.10, an expression for the stress intensity range is obtained.

$$K = Y\sigma\sqrt{\pi a} \rightarrow \Delta K = Y\Delta\sigma\sqrt{\pi a} \tag{3.10}$$

The behavior of the crack growth can be described as the relationship between the stress intensity range ΔK, and crack growth rate da/dN. Figure 3.9 shows a typical log-log plot of the crack growth rate with respect to the stress intensity range. In the intermediate region, a linear trend is observed. This linear region can be described by the Paris' Law given in equation 3.11, where m is the slope of the curve and C is a constant. The fatigue crack growth threshold ΔK_{th}, along with the fracture toughness K_C, is also indicated in figure 3.9. ΔK_{th} is a limit value for ΔK, indicating the threshold of which crack growth is expected to start, while K_C is the value where failure occurs.

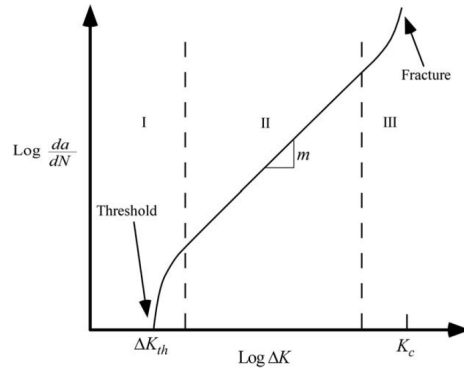$$da/dN = C(\Delta K)^m \tag{3.11}$$

Figure 3.9: Fatigue crack growth, from [23].

3.5   The Finite Element Method

The majority of problems in engineering and physics cannot be solved using analytical methods. When the complexity is high and large amounts of partial differential equations must be solved, the Finite Element Method (FEM) can be used to discretize the problem by introducing numerical methods. The discretization divides the problem into simpler and smaller parts and serves as an approximation of the original problem.

When using the FEM in structural analysis, the structure is divided into a finite number of elements containing nodes. These nodes can be placed at the corners, along the edges, or inside of the elements. The external nodes connect the different elements and have degrees of freedom (DOF) that can be rotations or translations. When the nodes are displaced, the displacements within the element are interpolated from the nodal displacements. Depending on the element type, the interpolation is either first or second order. For linear elements, nodes are placed at the corners and the interpolation is first order, while quadratic elements have nodes on both corners and on the midsides, and use a second order interpolation between the nodes. When a component is meshed, a certain amount of elements are assigned to the component. The density of the mesh dictates the number of elements, hence the accuracy of the results, as well as the computational time of the calculations. The elements can be 1D, 2D and 3D. Figure 3.10 shows two variants of 2D triangle and quadrilateral elements.
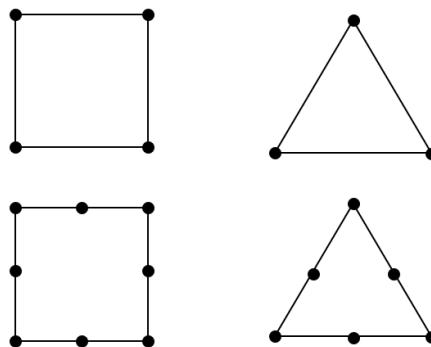

Figure 3.10: Quadrilateral (left) and triangle (right) elements.

16

Today, computers are often used when solving problems using the FEM. In this work, the Abaqus CAE software is used for numerical calculations. Abaqus is a finite element analysis (FEA) software that can be used in engineering tasks, including modelling, analysis and results visualization. The software is divided into modules, where each module contains specific tools for setting up the FEA task [25]. There are a total number of ten modules.

Shape Optimization in Abaqus

The Tosca Structure software can be implemented in the optimization module in Abaqus to perform different optimization tasks of a given geometry. Tosca Structure can be used to perform topology optimization, shape optimization, size optimization and bead optimization. These optimization modules are used to find the optimal solution to a given problem, and serve as powerful tools when designing or improving components in engineering tasks.

In this work, the shape optimization module is the most relevant [26]. Shape optimization is used to make final design improvements with respect to stress, strain and durability, without drastically changing the shape of the component. When setting up the shape optimization task, design area, design responses, objective function and constraints must be defined. Design area is the region to be optimized, while the design responses are the variables to include in the optimization task, typically volume and maximum stress or strain for shape optimization. The objective function and constraints are both defined based on the design responses. For example, the objective function can be to minimize a stress design response, while the constraint can be to keep a volume design response constant. By slightly changing the positions of the surface nodes in the design area, the aim is to minimize the design response defined by the objective function, and at the same time stay within the constraint.

3.6 The Theory of Critical Distances

This section includes an introduction to the Theory of Critical Distances (TCD), starting with the general concept of the theory. Then, some approaches of the TCD are presented, followed by a brief literature review of the TCD.

3.6.1 Basics of the Theory of Critical Distances

Performing a failure analysis of a component can be a challenging task and several factors have to be taken into account. Factors that are commonly highly influential on the cause of failure can originate from the manufacturing process, or they can be related to poor design. Causes of failure stemming from the manufacturing process are often cracks or pores, while failure due to poor design is mostly related to stress raising features, such as sharp edges and corners. All the aforementioned causes of failure create high local stresses, with the stress decreasing with the distance from the stress raising feature.

The TCD [27] is a group of methods, some of which were introduced as early as the mid-twentieth century, used predict brittle failure and fatigue of components containing stress raisers. With the basis of a material length parameter L, the material's critical

distance, the TCD methods postulate that failure occurs not only due to an excessive stress at the notch root, but rather due to the stress situation at a distance from the maximum stress. As shall be seen later in this chapter, some TCD methods also use the stress intensity factor by introducing LEFM principles. An important aspect of the TCD methods is that L only depends on the material of a given component and not on its geometric features.

In order to predict failure of a component using the TCD methods, a failure criterion must be established. For brittle fracture, this leads to the introduction of two additional material constants, namely the material's critical stress σ_0 and the fracture toughness K_C. In the case of fatigue failure, the critical stress can simply be changed to the cyclic critical stress $\Delta\sigma_0$, while the fatigue crack propagation ΔK_{th} is used instead of the critical stress intensity. For metallic materials, $\Delta\sigma_0$ is equal to the plain specimen fatigue strength, while σ_0 is larger than the ultimate tensile strength σ_{UTS} of the material [27]. The relationship between the critical distance, the critical stress and stress intensity will be further discussed below.

3.6.2 The Critical Distance Approaches

The TCD methods can roughly be divided into two main categories [28]; stress based methods and methods based on fracture mechanics, both of which can be used to predict either brittle fracture or fatigue. The stress-based methods can again be divided into three separate methods that consider the linear elastic stress field at the vicinity of the notch, aiming to determine the effective stress, σ_{eff} as a function of L. After the σ_{eff}-determination, the effective stress is compared to the material's critical stress σ_0. As previously mentioned, the stresses can be described as cyclic values in case of fatigue. The three stress-based TCD methods for fatigue are listed below [29], followed by a short explanation of the fracture mechanics approaches.
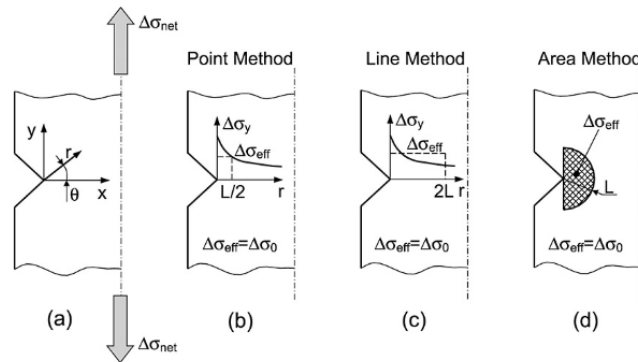

Figure 3.11: Local coordinate system for the notch and visualization of the three stress based TCD approaches, from [29].

The Point Method
The simplest of the four stress-based TCD methods is referred to as the point method (PM). The PM defines σ_{eff} as the stress at a distance L/2 from the notch root, as illustrated in figure 3.11 (b). According to the PM, the effective stress can be described

by equation 3.12, where $\Delta\sigma_y$ is the stress range perpendicular to the notch bisector line.

$$\Delta\sigma_{eff} = \Delta\sigma_y\left(\theta = 0, r = \frac{L}{2}\right) \tag{3.12}$$

The Line Method

In the line method (LM), the effective stress is calculated by averaging the stress field over a distance 2L, starting from the notch root. Figure 3.11 (c) illustrates how σ_{eff} is obtained according to the LM, and equation 3.13 shows the mathematical formulation.

$$\Delta\sigma_{eff} = \frac{1}{2L}\int_0^{2L}\Delta\sigma_y(\theta = 0, r)dr \tag{3.13}$$

The Area Method

The area method describes the effective stress as the average of the maximum principal stress over a given area at the vicinity of the notch. This area is shown in figure 3.11 (d) and defined as a semicircular area with its center at the notch tip, and a radius of 1.32L. Equation 3.14 shows the mathematical formulation of the effective stress according to the area method, where $\Delta\sigma_1$ is the maximum principal stress range.

$$\Delta\sigma_{eff} = \frac{4}{\pi L^2}\int_0^{\pi/2}\int_0^L \Delta\sigma_1(\theta, r)\cdot r\cdot dr\cdot d\theta \tag{3.14}$$

Fracture Mechanics Approaches

By introducing LEFM principles into the TCD formulations, a relationship between the critical distance, the critical stress and the stress intensity factor can be established. This relationship is described by equation 3.15 and equation 3.16, used for brittle fracture and fatigue respectively. As can be seen from the equations, and as previously mentioned, $\Delta\sigma_0$ is used instead of σ_0 and ΔK_{th} is used instead of K_C, when going from brittle fracture to fatigue. These formulas are valid for central through cracks in infinitely large plates, but the geometry factor Y can be introduced to take into account other types of cracks.

$$L = \frac{1}{\pi}\left(\frac{K_C}{\sigma_0}\right)^2 \tag{3.15}$$

$$L = \frac{1}{\pi}\left(\frac{\Delta K_{th}}{\Delta\sigma_0}\right)^2 \tag{3.16}$$

The TCD methods based on fracture mechanics can be divided into two slightly different approaches, where both of them uses the stress intensity factor as the critical parameter [30]. The first approach is referred to as the "introduced crack method" and assumes the presence of an actual crack at the notch root. However, this method is not well suited when predicting the behavior of a notch if the length of the crack is equal to or smaller than L. This leads to the introduction of the second method, the "imaginary crack method" (ICM), where an imaginary crack is introduced to the notch root and the crack is assumed to obey the laws of LEFM. Taylor [30] has summarized how the predictions based ICM gives similar results to that of the PM and LM.

3.6.3   Literature Review of the Theory of Critical Distances

This section includes some information found in the literature in order to get a better understanding of the mechanisms and applicability of the TCD.

Finding L
In order to make predictions based on the TCD, the material's critical distance must be determined. This can be a challenging task and requires experimental data as well as numerical or analytical calculations. Several procedures for obtaining L are reported in the literature, covering a wide range of complexity.

With today's availability of FE software, obtaining the stress fields of different notch geometries is often a straightforward task. This provides a solid foundation for the application of the stress-based TCD methods outlined above, considering that the stress field at the vicinity of the notch is an essential part of these methods. Taylor et al. [31] and Louks and Susmel [29] have applied FE software to determine the critical distance by means of the PM when solving fatigue problems. With the basis of fatigue tests of specimens with different notch geometries, including one unnotched specimen, both studies create combined plots of the stress fields of the different geometries. This is done by constructing linear elastic stress fields that represent the stress situation at the fatigue limit of the specimens. Figure 3.12 and figure 3.13, taken from [31] and [29] respectively, show the resulting stress field plots and reveal how the curves intersect at approximately the same point.
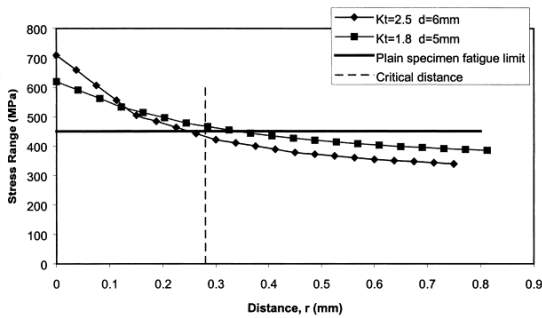
Figure 3.12: Stress fields for different specimens at the fatigue limit, from Taylor et al. [31].
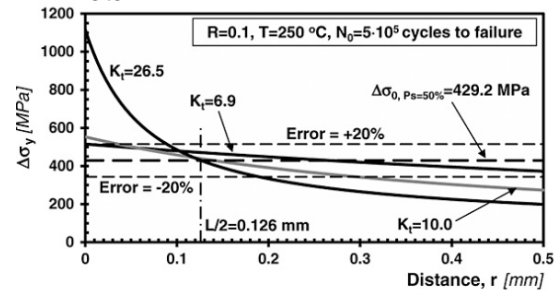
Figure 3.13: Stress fields for different specimens at fatigue limit, from Louks and Susmel [29].

Recalling that the PM postulates that the critical stress range equals the plain specimen fatigue strength at the half of the critical distance for metals, the intersection between the unnotched and notched specimens can be considered as L/2. Taylor et al. [31] defined L/2 as the midpoint between the intersection of the two notched specimens and the unnotched specimen, while Louks and Susmel [29] defined L/2 as the intersection between the unnotched specimen and the notched specimen with the highest stress concentration factor.

A more sophisticated approach to determine the critical distance has been proposed by Benedetti and Santus [32]. In their approach, the fatigue critical distance is found by means of both the PM and LM, using the inverse search procedure illustrated in figure 3.14. The resulting critical distances are denoted L and L', based on the LM and PM

respectively. A cylindrical V-notched specimen with a notch root radius of 0.2 mm and an unnotched specimen are used for the calculations. The procedure involves a stepwise process where the initial dimensionless critical distances, l_0 and l_0', are found in the first step by assuming the stress as the singular term ahead of an ideally sharp V-notch. This is done by introducing the dimensionless notch-stress intensity factor (N-SIF) $K_{N,UU}$, the Williams power law singularity exponent s, and the fatigue stress concentration factor K_f. The N-SIF is obtained through a numerical analysis using FE software, while K_f is found by performing fatigue tests on the two specimens. K_f is the only experimental input needed and is defined as the fatigue strength of the unnotched specimen divided by the fatigue strength of the notched specimen.

In the second step of the inverse search procedure, correction functions are introduced in order to take into account the effect of the notch radius. This correction effectively gives the dimensionless critical distances, l and l', calculated for the LM and PM respectively. After finding the dimensionless values, the real critical distance values, L and L', can simply be found by multiplying the dimensionless values with the radius of the specimen. A more in-depth description of the entire procedure is provided in [33].
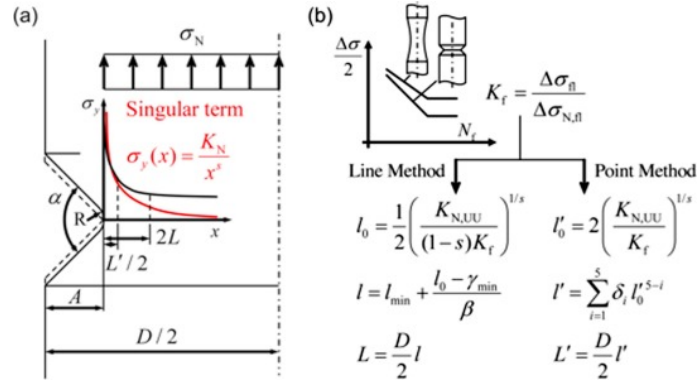
Figure 3.14: Visualization of the TCD approach proposed by Benedetti and Santus [32].

In the same study [32], the critical distance is also determined by using the fracture mechanics approach given by equation 3.16. This procedure requires information about the full range of the unnotched specimen fatigue limit $\Delta\sigma_0$, and the threshold stress intensity factor range ΔK_{th}, obtained through fatigue crack growth (FCG) rate tests. As pointed out by the authors, ΔK_{th} can be challenging to measure, introducing high uncertainty when calculating the critical distance. This problem is confirmed by the results in the study, where the inverse procedure summarized above gives better results than those of the fracture mechanics approach.

Critical Distance Values for Metallic Materials
Atzori et al. [34] has summarized the critical distance values for a wide range of materials. The values are calculated based on fatigue testing and show that the critical distance can vary with orders of magnitude between different metals. The lowest reported value is 0.004 mm for 16F steel tested at a load ratio of R=0.1, while the largest value is 4.410 mm for grey cast iron tested at R=0.5. For steels, the L values ranges from 0.004 mm to 0.782 mm, while the L values for aluminum alloys ranges from 0.011 mm to 0.396 mm. Cast irons have the largest critical distance values, spanning from 0.105 mm to 4.410 mm.

As for Inconel 718, Louks and Susmel [29] determined the critical distance based on data from Chen et al. [35]. The fatigue testing was performed by means of rotating bending at elevated temperatures on both notched and unnotched specimens, and the critical distance was calculated to be 0.154 mm.

Influencing factors on the Critical Distance

Taylor [36] reported the relationship between the material's critical distance and its grain size. Based on data from Yokobori and Konosu [37], where the material was heat treated to obtain different grain sizes, he calculated the critical distance based on brittle fracture and compared it to the grain size. The results are reported in figure 3.15 and shows a clear relationship between critical distance and grain size, where the critical distance increases with grain size.
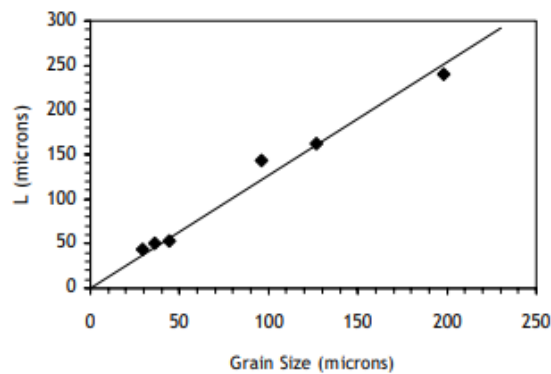
Figure 3.15: Relationship between L and grain size, from [36].

The notch effect on PUR, which is a polymer material, was investigated by Negru et al. [38]. By performing tests on notched samples with different densities, the static properties were determined by means of the TCD, based on two notch geometries. Figure 3.16 shows the stress fields of U-notched and V-notched specimens and reveals a relationship between the critical distance and the density of the material. The results are summarized in table 3.1. It is evident that the critical distance decreases with increasing density, indicating that the microstructural features of the PUR material related to density influences the material's critical distance. A possible explanation for this is that a high density gives smaller cell diameters for the cellular structure of PUR, which in turn leads to a shorter critical distance.
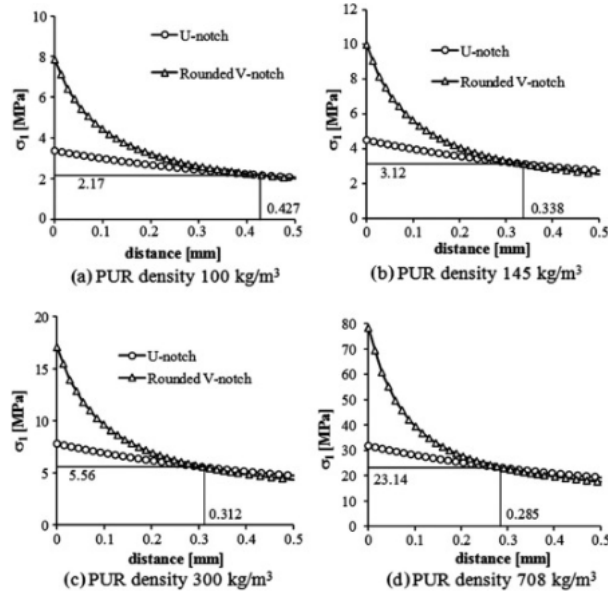
Figure 3.16: Stress fields for PUR-specimens with different density and L/2 indicated. Data from [38].

PUR density [kg/m^3]	100	145	300	708	1218
Length, L [mm]	0.854	0.676	0.624	0.570	0.296

Table 3.1: Relationship between the density and critical distance of PUR. Data from [38].

Another influencing factor on the critical distance is the load ratio R. It is well known that R affects both $\Delta\sigma_0$ and ΔK_{th}, and referring to the relationship described by equation 3.16, it is to be expected that also the critical distance should change with R. Figure 3.17 shows typical values for how the fatigue limit and threshold changes with R for steel. By calculating L for different R ratios using equation 3.16, a relationship between L and R can be established. This relationship is plotted in figure 3.18 and shows that L decreases linearly with increasing R until R reaches a limit value. This limit value is determined by the relationship between the threshold stress intensity range and R ratio, which is set to R=0.5 in this case. After the limit value, the critical distance increases rapidly.
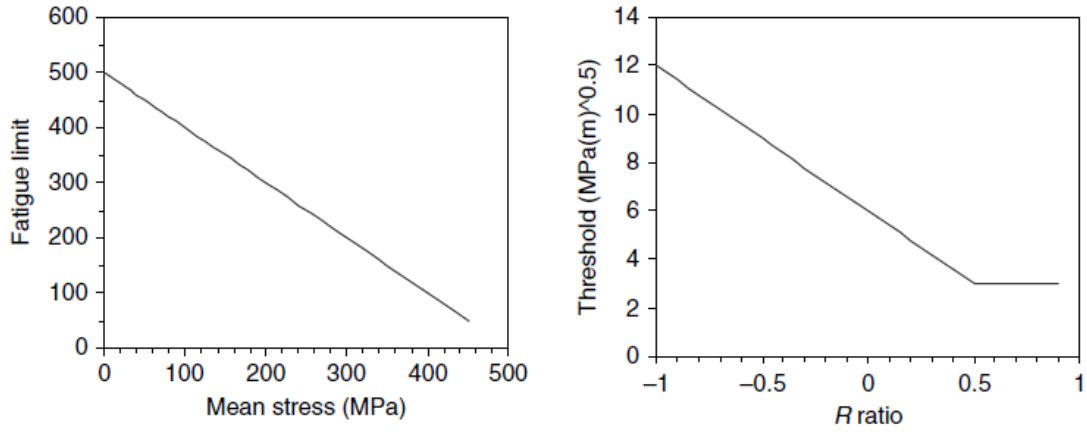
Figure 3.17: Graphs showing the dependency of fatigue limit (left) and threshold (right) on load ratio, R. Data for steel from [39].
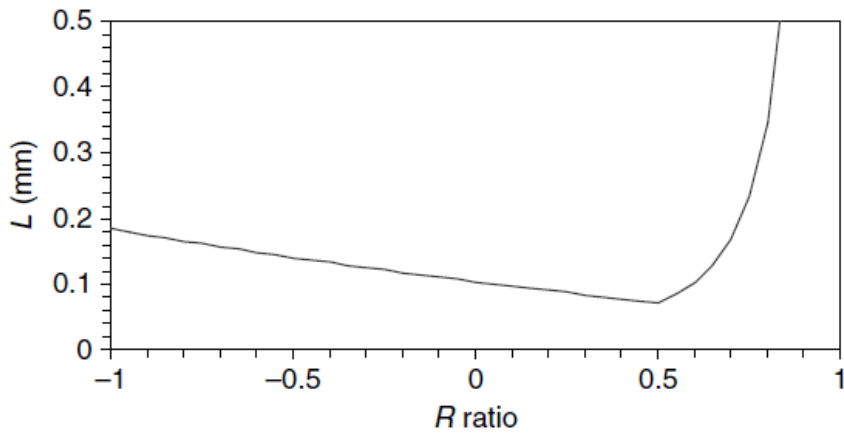
Figure 3.18: Relationship between critical distance, L, and load ratio, R, from [39].

It should be mentioned that the change in $\Delta\sigma_0$ and ΔK_{th} with respect to R, illustrated in figure 3.17, are simplistic and these trends do not apply for all materials. Taylor [40] investigated the relationship between R and L for cast iron and found little variation in L for R-values between 0.1 and 0.7. This result is shown in figure 3.19.
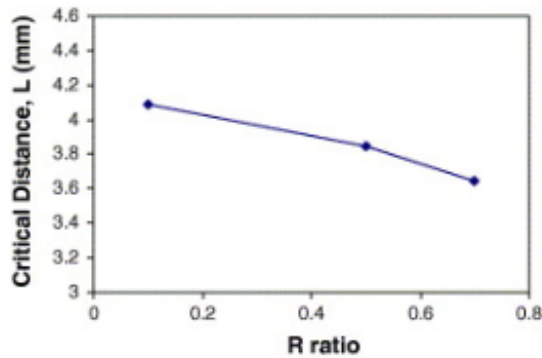
Figure 3.19: Relationship between L and R for iron, from [39].

24

The fact that L changes with different load ratios may seem as a problem when applying the TCD to data where R is not constant. However, Taylor [39] investigated the ability of the PM to predict the fatigue limit of a steel material loaded with different R ratios, using a constant L-value. These results are presented in figure 3.20 and shows that a constant value for L can be used to assess the fatigue limit over a large span of R ratios.
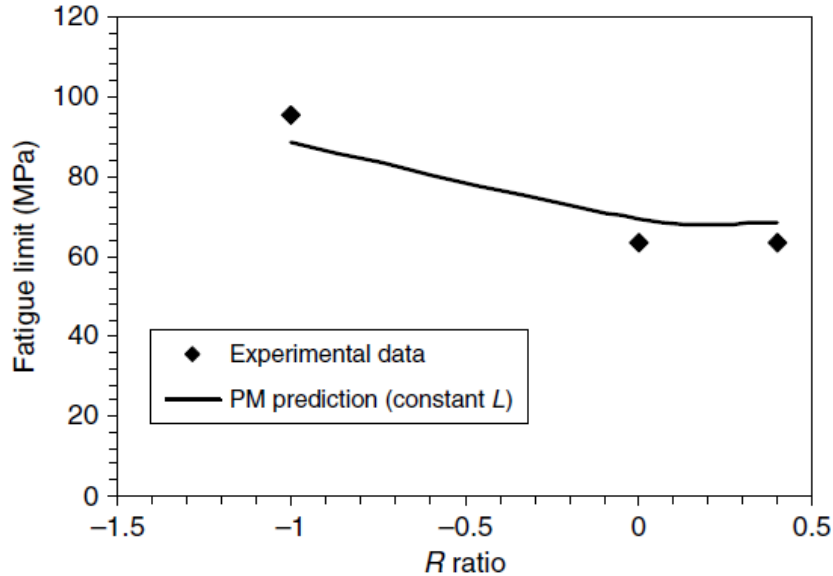
Figure 3.20: PM prediction of fatigue limit for steel for different R, from [39].

Accuracy of the Theory of Critical Distances

Using the inverse search procedure previously described, Benedetti and Santus [32] predicted the high cycle fatigue strength of blunt-notched specimens produced by SLM. First, the critical distance of two different sharp-notched specimens were obtained using the inverse procedure for both the PM and LM. The sharp-notched specimens were different in that the notches were either built directly from the printer or machined from a plain surface. Second, the critical distances were used to assess the fatigue limit of blunt-notched specimens whose notches were created in the same way as for the sharp-notched specimens. Table 3.2 lists the prediction results and distinguishes between as-built notch and machined notch. The results show that the predicted values are all below a 10% error of the experimental fatigue limit results, both for the PM and LM. As for the difference in accuracy between the PM and LM, the PM yields slightly more accurate results. However, it must be stressed that the results are generally satisfactory.

	Experimental [MPa]	LM Predicted [MPa]	Error [%]	PM Predicted [MPa]	Error [%]
Turned blunt notch	116.6	126.0	8.0	120.0	2.9
SLM blunt notch	144.8	145.9	0.8	142.1	-1.9

Table 3.2: Results of prediction of the fatigue strength of blunt notched specimens at 5×10^5 cycles to failure [32], based on L values obtained through the PM and LM. The predicted fatigue strength is compared with the experimentally obtained fatigue strength.

In the same study [32], the critical distance was also obtained by performing fatigue crack growth tests and applying the fracture mechanics approach described in section

3.6.2, using equation 3.16. This critical distance was then used to assess the fatigue limit of the blunt-notched specimens, using both the PM and LM, giving the results presented in table 3.3. These results reveal a slightly inferior prediction accuracy with respect to the results obtained by using the PM and LM inverse procedure, but the error is well below 20%.

		LM		PM	
	Experimental [MPa]	Predicted [MPa]	Error [%]	Predicted [MPa]	Error [%]
Turned blunt notch	116.6	101.0	-13.4	98.0	-15.9
SLM blunt notch	144.8	125.9	-13.0	123.6	-14.7

Table 3.3: Results of prediction of the fatigue strength of blunt notched specimens at 5×10^5 cycles to failure [32], based on L value obtained through the fracture mechanics approach. The predicted fatigue strength is compared with the experimentally obtained fatigue strength.

Louks and Susmel [29] investigated the accuracy of the stress based critical distance approach described in section 3.6.2. By means of the PM, the critical distance was determined based on axially loaded unnotched and sharp V-notched specimens at elevated temperature, using their stress fields and fatigue limits. This critical distance value was then applied to the PM, LM and area method in order to find the effective stress $\Delta\sigma_{eff}$, which was compared to the plain specimen fatigue limit. The error was then calculated as shown in equation 3.17, and all results are presented in table 3.4. The results reveal that the TCD is able to predict the fatigue limits with an absolute error below 15%, and that the PM yields slightly superior prediction results.

$$Error = \frac{\Delta\sigma_{eff} - \Delta\sigma_0}{\Delta\sigma_0}[\%] \tag{3.17}$$

Specimen	$\Delta\sigma_0$ [MPa]	PM		LM		Area Method	
		$\Delta\sigma_{eff}$ [MPa]	Error [%]	$\Delta\sigma_{eff}$ [MPa]	Error [%]	$\Delta\sigma_{eff}$ [MPa]	Error [%]
Plain	429.2	-	-	-	-	-	-
Blunt U-notch	-	471.0	9.7	436.4	1.7	476.6	11.1
Sharp U-notch	-	439.8	2.5	380.0	-11.5	449.1	4.6
Sharp V-notch	-	429.2	0.0	369.9	-13.8	439.5	2.4

Table 3.4: Results from [29] showing the accuracy of the stress based TCD methods when predicting the fatigue limit of different specimens.

In the same study [29], the same TCD approach was adopted in order to predict the fatigue limits of specimens found in the literature. The results confirm the good prediction accuracy of the TCD methods, with an absolute error generally well below 20%. Only one estimated value had an error above 20%. For the sake of brevity, the results are not included here.

4   Inconel 718

Inconel 718 is a high strength corrosion-resistant nickel chromium superalloy, and is the most commonly used among the Ni based superalloys [41]. Due to its excellent properties in high temperatures and resistance to corrosive environments, it has a wide range of applications. It is used in temperatures ranging from -250°C to 700°C [1] and has low price/performance ratio, good formability and weldability properties [42]. Conventionally manufactured Inconel 718 is mostly adopted by industries such as aerospace, nuclear and petrochemical, with more specific applications being; gas-turbines, jet engines and high-speed airframe parts, exhaust manifolds or turbochargers [43]. One issue with Inconel 718 is that the low thermal conductivity, high hardness, high strength at high temperature, and tendency to react with tool materials, make it challenging to produce parts using conventional machining methods [44]. This especially applies for parts of complex geometries, and makes it relevant to introduce an alternative manufacturing method that does not rely on conventional machining methods, such as additive manufacturing. The composition ranges of Inconel 718 is given in table 4.1.

Element	Chemical Composition, %
Ni (+Co)	50.00-55.00
Cr	17.00-21.00
Fe	Balance
Nb (+Ta)	4.75-5.50
Mo	2.80-3.30
Ti	0.65-1.15
Al	0.20-0.80
Co	1.00 max.
C	0.08 max.
Mn	0.35 max.
Si	0.35 max.
P	0.015 max.
S	0.015 max.
B	0.006 max.
Cu	0.30 max.

Table 4.1: Typical composition limits for Inconel 718. Data from [1].

4.1   Microstructure of Inconel 718

Inconel 718 is a precipitation strengthened alloy, which in essence means that the strength of the material increases by precipitation of secondary phases. These phases strengthen the material by acting as obstacles to dislocation movement [45]. Inconel 718 generally consist of three phases; γ' (Ni3(Al, Ti) with face-centered cubic ($L1_2$) ordered structure,

γ'' (Ni_3Nb) with body centered tetragonal ($D0_{22}$) structure, and γ phase with face centered cubic structure. γ' and γ'' act as the hardening precipitation phases, with γ'' serving as the major hardening phase due to its larger volume fraction [46]. The volume fractions of γ' and γ'' in commercial Inconel 718 are approximately 0.13 and 0.04, respectively [47]. Both γ' and γ'' precipitate between 600°C and 900°C and are uniformly distributed [48]. γ'' is a metastable phase, and its stability is limited to the temperature range between 650°C and 700°C [49]. For operation temperatures above this, γ'' phases coarsen fast and transforms into either γ' or δ phases, leading to reduction of strength thus limiting application temperature [43].

δ is the third precipitation phase for wrought Inconel 718 and has the same composition as γ'', namely Ni_3Nb, but with a different crystal structure; orthorhombic crystal structure [50]. It grows with a corresponding loss of γ'' phase, because both phases are Nb-based. As opposed to γ' and γ'' precipitates that are uniformly distributed, the δ phase precipitate at the grain boundaries [43, 48], and it precipitates between temperatures if 700°C and 1000°C. With increasing temperature, the size and amount of δ phase increases [46]. In conventional Inconel 718, the precipitation of δ phase is found to be proportional to the aging time [51]. As previously indicated, precipitation of δ phase related to inferior mechanical properties [49]. This is mainly due to the transformation from the γ'' phase to δ phase at grain boundaries, leading to lower strength particularly in grain boundary regions [51]. In case a fine grain structure is required, δ phase can be used to control the grain growth [52]. For fatigue properties, the influence of δ phase has been researched in several studies, but no agreement has been established on whether it has a positive or negative impact [53].

Intermetallic phases, known as topologically close-packed (TCP) phases, can be unfavorable with respect to the mechanical properties of the superalloy [54]. One of these TCP phases is Laves phase, which segregates during solidification of Inconel 718. During the additive manufacturing process, Laves phases form at the end of the solidification process due to microsegregation of the alloying elements. B. P. Bewlay et al., [55] reports that Laves phase have exceptional mechanical properties at high temperatures. Laves phases are hard and brittle with irregular shape and S. Sui et al., [53] claim that they are generally detrimental to physical properties of Inconel 718 (tensile, stress rupture, and low-cycle fatigue properties). The same authors also report that microscopic holes often start at Laves during persistent and tensile testing, and that they aid in easy crack initiation and propagation during LCF tests. In addition, the authors inform that a post-process heat treatment is used in order to eliminate the Laves phases in laser additively manufactured parts. High cooling rate and low heat input has also shown to be beneficial in avoiding segregation of Laves phase [56].

4.2   Heat Treatment of Inconel 718

This section, except from the part about HIP, is based on Matthew J. Donachie and Stephen J Donachie's book Superalloys: A Technical Guide, 2nd Edition [57].

By definition, heat treatment is any procedure where a sufficiently high temperature is affecting a material for a given time. In order to obtain the desired properties and attributes of a metallic material, a specific heat treatment process is often needed. The

process serves to accomplish one of the following: reduce stresses; promote grain growth; allow atom movements to redistribute existing alloy elements; promote new recrystallized grain formation; produce new phases, owing to precipitation from solid solution; dissolve phases; cause alloys surface chemistry to change by introduction of foreign atoms; cause new phases to form by introduction of foreign atoms. For additive manufactured components, additional heat treatment methods are often executed to make up for the characteristic attributes specifically related to this manufacturing process. For Inconel 718, the most common heat treatment processes are as follows:

- **Solution annealing**
  The solution treatment process has the purpose of dissolving secondary phases and is normally the first step of the heat treatment of precipitation hardened alloys. The dissolution of secondary phases is done in order to obtain maximum corrosion resistance, or to prepare the alloy for subsequent aging. In order to achieve the desired properties of an alloy, the solution treatment temperature is an important factor. A high temperature results in optimal creep-rupture properties; a lower temperature leads to optimal short-time tensile properties at elevated temperature, improved fatigue resistance due to the finer grain size, and improved resistance to notch rupture sensitivity.

- **Full annealing**
  Full annealing is conducted in order to obtain complete recrystallization and attainment of maximum softness of the material. The main purpose of the annealing process is increase in ductility and reduction of hardness.

- **Precipitation (age) hardening**
  The precipitation treatment is performed in order to strengthen precipitation strengthened alloys. This is done through the precipitation of secondary phases that has been developed by the solution treatment process and retained by cooling from the solution treatment temperature. In the case of Inconel 718, the strengthening phases are called γ' and γ''. Another purpose of precipitation treatment is controlling detrimental secondary phases, such as carbides and TCP phases [54]. By changing the temperature of the precipitation process, the type and size distribution of precipitates can be controlled. A higher aging-temperature leads to more rapid coarsening of γ' and γ'' phases [58]. It is common to perform multiple precipitation processes for wrought alloys, and a double-aging can be employed to produce different sizes and types of precipitates.

- **Hot isostatic pressing (HIP)**
  Due to the porosity often present in additively manufactured components, hot isostatic pressing, or HIP, is usually performed after the printing process. With a pressure between 100 and 200MPa and temperatures from 900°C to 1250°C for steels and superalloys, the HIP-process serves to provide isotropic properties and 100% densification [59], as well as preventing lack-of-fusion defects between layers. HIP is also applied in other powder metallurgy processes, such as metal injection molding or pressing and sintering. It has been suggested that the high temperature involved in HIP leads to a homogenous phase structure with a fine grain structure, as well as precipitation of γ' and γ'' phases if followed by the aging procedure, leading to improvement in σ_{YS} and σ_{UTS} and lower ductility [43].

5 Literature Review of Additively Manufactured Inconel 718

In this chapter, a literature review is carried out on both the static and fatigue properties of AMed Inconel 718. This is done to get a better understanding of the properties and mechanisms of the material.

5.1 Static Properties

This section includes a selection of papers and experiments where the static properties of AMed Inconel 718 are investigated. Only what is considered to be relevant figures and information is included here, and it is suggested to review each article for further understanding and investigation. Each subsection is given the title of the relevant article or experiment.

5.1.1 On the microstructural and mechanical properties of post-treated additively manufactured Inconel 718 superalloy under quasi-static and cyclic loading

By performing different post-treatment processes on SLM Inconel 718, the mechanical properties of the material have been determined [51]. Tensile tests were performed on dogbone-specimens using a servo-hydraulic testing machine at room temperature. The specimens were printed in the direction vertical to the building platform and subjected to several conventional heat treatment methods; solution annealing (S) 1000°C/1h AC, HIP (H) 1150°C/4h 100MPa FC, and double aging (A) 720°C/8h $\rightarrow$ FC at 50°C/h to 620°C/8h AC. The combination of the different heat treatments is done in order to study the effect of post process heat treatments on mechanical properties. A coating treatment was also conducted on the HIPed specimens, but it did not improve the mechanical properties of the specimens. Thus, the effect of the this procedure will not be discussed further in this project.

From the micrographs in figure 5.1, a relationship between grain structure and heat treatment method can be seen. The solution annealed and the as built specimens exhibit similar microstructure, while HIPed specimens have a different condition. The solution annealed, and as built specimens have elongated columnar grains parallel to building direction, whereas specimens subjected to HIP have a microstructure of coarser grains without columnar morphology, indicating that the HIP-temperature is high enough to start recrystallization.
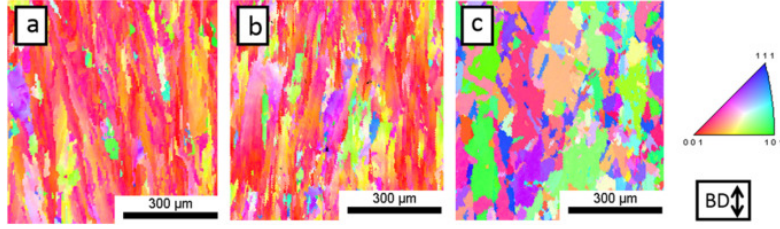
Figure 5.1: Microstructure of the material for (a) as-built, (b) solution annealed, and (c) HIP. Similar oriented grains have similar colors [51].

The results show that the HIP process is able to close most of the internal pores, while surface pores still are present after HIP. Additionally, both solution annealing and HIP caused complete dissolution of the Laves phase. The Laves phases in the as-built specimens are illustrated in figure 5.2, and can be seen as white particles and secondary reflections. It also seems that solution annealing removed most of the sub-micron cell structures and secondary phases present in the as-built condition, while HIP treatment dissolved all of them. The nature of the sub-micron cell structures is not defined in the article, but the author suggests further research to be done to understand these structures.
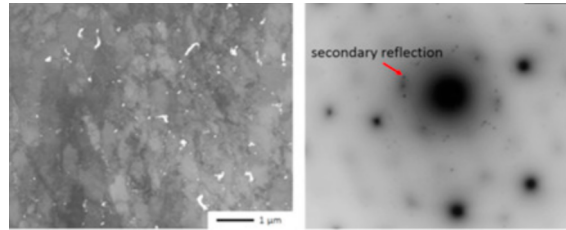
Figure 5.2: Laves phases in the microstructure. Shown as white particles (left) and secondary reflections (right) [51].

After being subjected to either solution annealing or HIP, some specimens also underwent aging. As previously mentioned, this is done in order to promote the precipitation of strengthening phases. The results show that aging upon solution annealing leads to precipitation of coherent γ'' phase throughout the matrix, but there is no sign of δ phase. The γ'' precipitates were also observed in the HIPed + aged specimens, but in this case also δ phase is present, even though the specimens underwent the same aging process.

A clear relationship between the heat-treatment methods and mechanical properties is revealed. From the stress-strain curves in figure 5.3 it can be seen that aging, as expected, leads to superior strength for aged specimens than that of those not subjected to aging. It can also be seen that the superior strength comes at the cost of lower ductility.
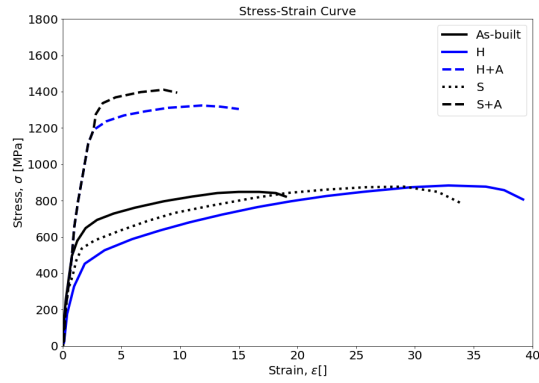
Figure 5.3: Stress-strain curves for different heat treatments. Data from [51].

5.1.2 Technical report from NASA

The NASA tests [60] were performed at room temperature on SLMed tensile specimens subjected to post processing heat treatment. This heat treatment included four different steps; stress relief 1165°C/1.5h FC, HIP 1165°C/100MPa/1h AC, solution 1066°C/1h AC, and double aging 760°C/10h → FC to 650°C/20h.

From the micrographs in figure 5.4, it becomes clear that the post process heat treatment has a big impact on the microstructure of the specimens. The as-built specimens exhibit a microstructure where the layer-by-layer characteristics are clearly visible. For the heat treated micrographs, the microstructure seems to be recrystallized with no typical orientation of the grains.
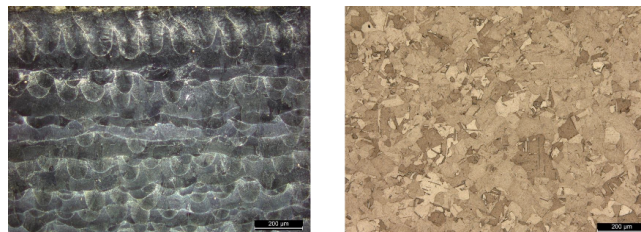
Figure 5.4: Microstructure of the material: Left is as-built, and right is heat treated [60].
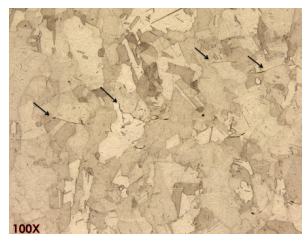
Figure 5.5: The arrows indicate the lack of fusion defects in the microstructure [60].

The metallographic examination also uncovers defects in the material identified as lack of fusion defects, and illustrated in 5.5. The effect of these effects is clearly visible in the stress-strain curves seen in 5.6, where the defects in essence lead to a shorter elongation at failure.
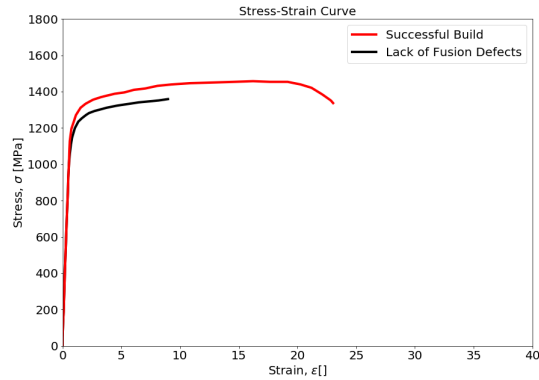
Figure 5.6: Stress-Strain curve with defect and non-defect specimens. Data from [60].

5.1.3 Low cycle fatigue behavior of direct metal laser sintered Inconel alloy 718

Using the direct metal laser sintering method, tensile specimens were produced in two different orientations with respect to the build direction as seen in figure 5.7 [41]. One set of specimens was produced parallel to the building platform, while the other specimens were printed 45°with respect to the platform. In addition, all specimens were machined to their final shape. A set of wrought heat treated specimens are also included in the test for comparison reasons. After the DMLS process, all specimens underwent heat treatment, while only a few specimens were subjected to HIP as well. The heat treatment was performed in the following steps; solution 954°C/1h argon cooling, and double aging 718°C/8h→FC at 50°C/h to 621°C/8h AC. The HIP process was conducted at 1163°C for 4 hours under a pressure of 100 MPa.
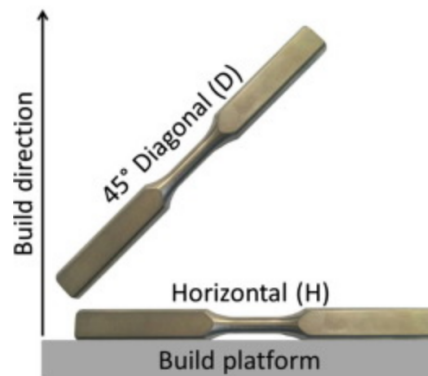
Figure 5.7: The two specimen-types with indicated build direction [41].

Evaluation of the microstructure in figure 5.8 reveals an elongated microstructure in the build direction for DMLS heat treated specimens, which leads to different microstructure for the specimens produced in different directions. Both heat-treated and as-built specimens show a fairly low content of porosity. For the HIPed specimens the microstructure is evaluated to have an equiaxed structure with no typical orientation, and the level of porosity is classified as negligible. The grain structure for HIPed specimens is also substantially coarser compared to grain size of the heat treated specimens. For wrought

33

specimens the grains are smaller than for HIP and their structure is also equiaxed. The porosity level for wrought is also considered to be zero.
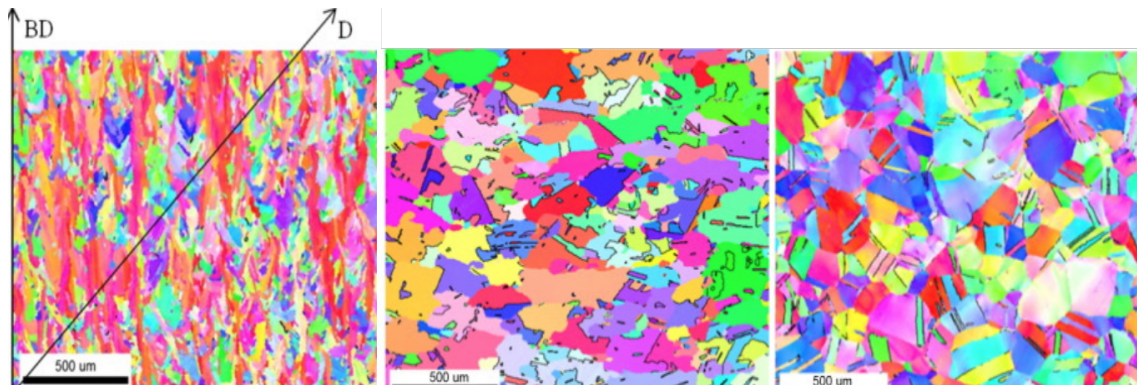
Figure 5.8: Microstructure of DMLS heat treated (left), DMLS HIP (center), and wrought (right). Build direction (BD) and orientation of diagonal specimen (D) is indicated. Similar oriented grains have similar colors [41].

The true stress-true strain curves in figure 5.9 show that the specimens subjected only to heat treatment have the highest strength. At the same time, the difference between building direction for heat treated specimens is obvious. Specimens with building direction parallel to the building platform show a longer elongation at failure than its 45°-counterpart. Even though the HIPed specimens exhibit a lower strength, the elongation at failure is superior to that of the heat treated specimens. In addition, it can be seen that wrought and HIPed specimens have comparable properties, with HIP having a higher elongation at failure.
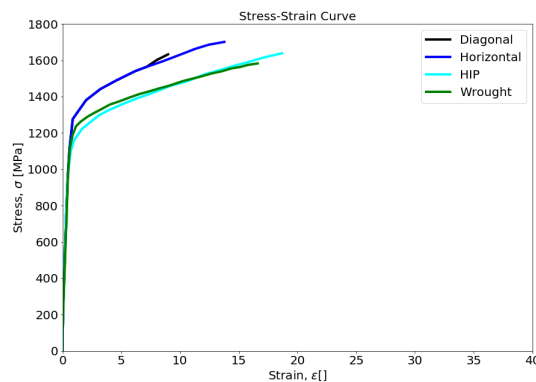
Figure 5.9: True stress-Strain curves for different directions and HIP, with wrought as reference. Data from [41].

5.1.4 Bending fatigue life characterisation of direct metal laser sintering nickel alloy 718

Two different types of plates, one with heat treatment and one without, were produced by means of DMLS [61]. The first plate is denoted V1, and was heat treated with the following process; stress relieving 1065°C/1.5h argon cooling, HIP 1177°C 103 MPa, solution treatment 968°C/1.5h, double aging 718°C/8h→to 612°C/8h and cooling. The

second plate, V2, did not undergo any post process heat treatment. Tensile test dog-bone specimens were machined from each plate, both parallel and perpendicular to the build platform, in order to investigate the influence of build direction on the mechanical properties. The directions of machining is shown in figure 5.10.
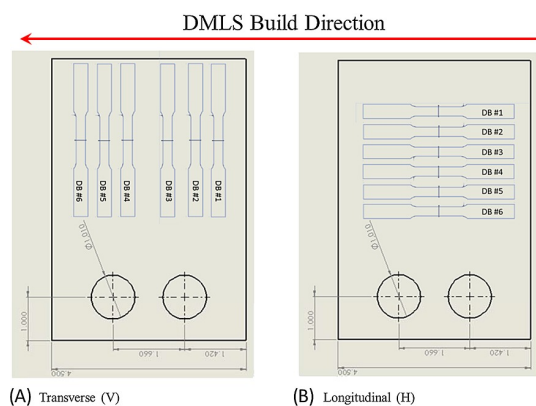
Figure 5.10: Plates with build direction and specimen orientations [61].
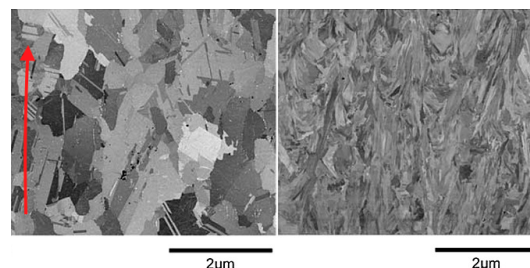
Figure 5.11: Microstructure of V1 (left) and V2 (right), with arrow indicating build direction [61].

Micrographs in figure 5.11 show that the heat treated material, V1, has relatively coarse equiaxed grains, while the as-built material, V2, contain columnar elongated grains in the building direction. The results presented in table 5.1, indicate that there is a difference in mechanical properties between materials V1 and V2. Generally, it can be seen V1 exhibits a higher ultimate strength than V2. At the same time, elongation to failure is higher for V2 materials. The results also show that the material properties partly rely on the building direction. For both V1 and V2, the ultimate strength is higher for the vertical specimens, but the strength-difference between horizontal and vertical specimens is more outspoken for material V1.

Plate-type	σ_{UTS} (MPa)	Elongation %	Col3
V1 - H	1316	18	787
V1 - V	1331	20	5415
V1 - V	1322	20	7507
V1 - H	1293	17	7560
V2 - H	1059	31	7560
V2 - V	1162	26	7560
V2 - H	1034	31	7560
V2 - V	1148	26	6344

Table 5.1: Ultimate strength and elongation at failure for the two plate-types. Direction with respect to build platform is indicated as H (horizontal) and V (vertical). Data from [61].

5.1.5 On the Tensile Properties of Inconel 718 Fabricated by EBM for As-Built and Heat-Treated Components

The production of dogbone tensile specimens was done by using electron beam manu-facturing, EBM, to print blocks measuring 15mm x 15mm x 35mm, with build direction

along the 35mm length and a preheat temperature of 1050°C [62]. Three different types of blocks were produced by employing three different sets of process parameters. These changes in parameters included changing of beam power and scan velocity, while keeping hatch distance and layer thickness constant. The different process parameters in essence led to a change in the Volume Energy Density (VED). The three types of specimens with their associated VED are reported in table 5.2. Before machining out the tensile specimens from the blocks, one block from each block-type was subjected to the following heat treatment: annealing 1000°C/1h, and double aging 720°C/8h → FC at 50°C/h to 621°C/8h AC. The specimens were machined from the blocks in such a way that the loading direction was parallel to the build direction.

Material	VED (J mm^{-3})
1	120
2	40
3	36

Table 5.2: Ultimate strength and elongation at failure for the two plate-types. Direction with respect to build platform is indicated as H (horizontal) and V (vertical). Data from [62].

The micrographs in figure 5.12 of the as-built specimens show elongated columnar grains in the build direction for all, but the amount of porosities depend on the energy input. The specimens with highest and lowest volume energy density show the highest amount of porosity.
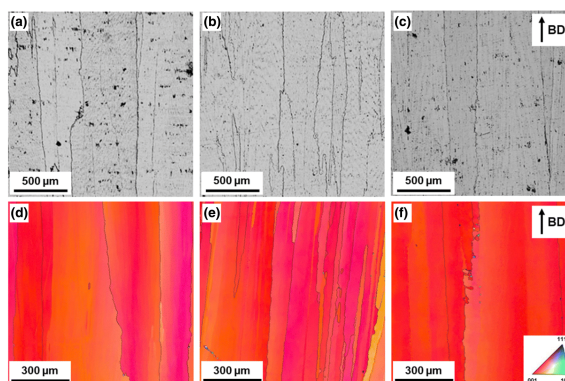
Figure 5.12: Micrographs of as-built specimens (a) 1, (b) 2, and (3). Illustrations (d), (e), and (f) showing orientation of microstructure of specimens 1, 2, and 3, respectively [62].

The tensile tests were conducted at room temperature, and the stress-strain curves in figure 5.13 show that the processing parameters have little influence on the as-built specimens. Both strength and ductility seem to be fairly similar for all three specimen-types. For the heat treated specimens, the strength is increased compared to as-built, but this does not come at the cost of lower ductility. The heat treated specimens have almost the same elongation at failure as the as-built specimens. It can also be observed that the heat treated specimens with highest and lowest volume energy density exhibit an inferior strength compared to the specimens with intermediate energy density.
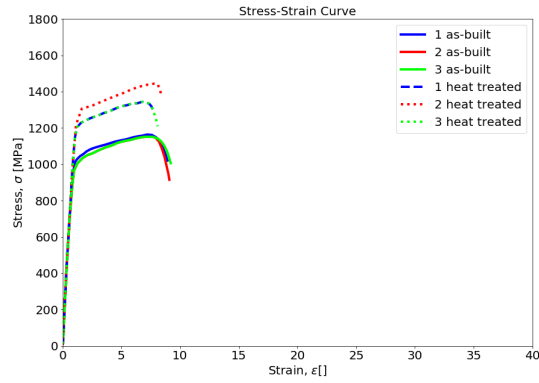
Figure 5.13: Stress-Strain curves for different as built and heat treated specimens. Data from [62].

5.1.6 Microstructure Development in Electron Beam-Melted Inconel 718 and Associated Tensile Properties

The tensile test specimens were machined out of 100 x 100 x 20 mm blocks, transversal to the build direction [63]. In order to investigate the effect of distance from build platform on mechanical properties, five specimens were machined from different heights in the block. The blocks were produced using EBM with a pre-heat temperature of 975°C. Tensile testing was conducted both at room temperature and at 650°C, and no heat treatment was performed on the specimens.

The micrographs reveal a microstructure which in essence is divided into three regions; region 1 reaches 0.6-0.75 mm from top of build, region 2 spans over the next 3.5 mmm, and region 3 that starts 5 mm from the top of the build and continues through the remaining length of the build. The locations of the regions are illustrated in 5.14. In region 1, Laves phase together with the γ'' precipitates have been observed in the microstructure. In region 2, the Laves phase has transitioned into δ needles along the grain boundaries. Region 3 has a columnar grain structure with δ precipitating at the grain boundaries, and the amount of δ phase increasing with distance from top of build.
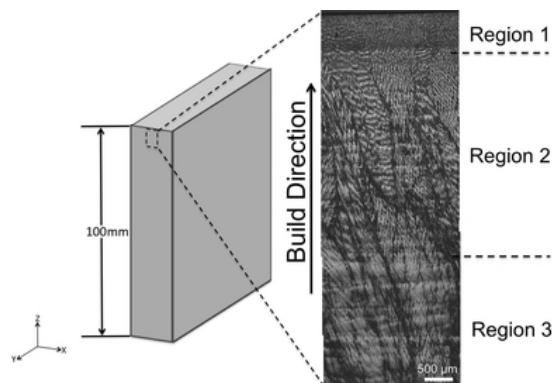
Figure 5.14: Illustration of the observed regions of the microstructure [63].
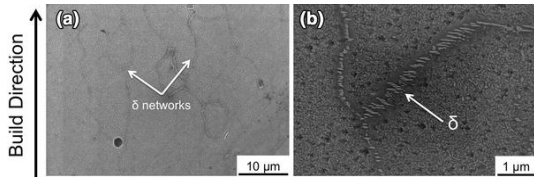
Figure 5.15: Microstructure in region 2 with δ phase along grain boundaries. (a) x2500 magnification, (b) x20 000 magnification [63].
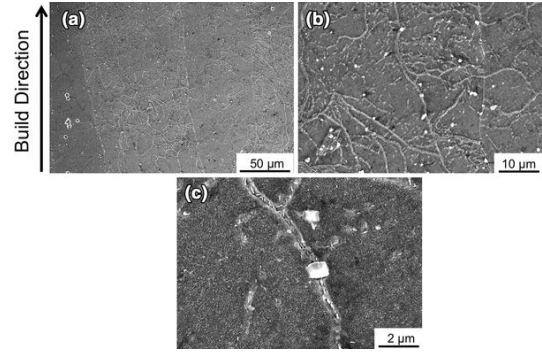
Figure 5.16: Microstructure in region 3 with δ phase seen as white networks. (a) x500 magnification , (b) x2000 magnification, (c) x10 000 magnification [63].

The tensile test results in figure 5.17 show an increase in strength and elongation at failure, for the room-temperature tested specimens, as the distance from the build platform increases.
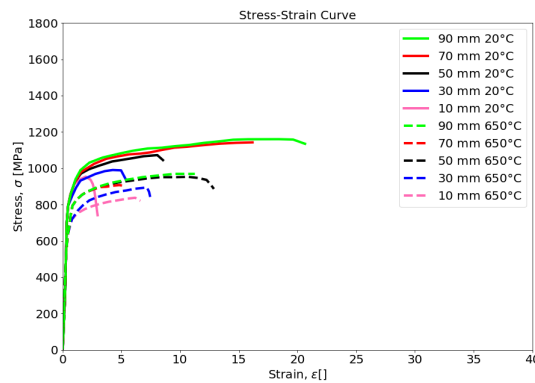
Figure 5.17: Stress-Strain curves with test-temperature and distance from build platform indicated. Data from [63].

5.1.7 Discussion

Based on the above articles, this section includes a discussion of the relevant findings.

Heat treatment
As can be seen from several of the articles above, heat treatment has an impact on monotonic properties of Inconel 718. In reference [51], presented in section 5.1.1, the HIP treatment leads to recrystallization of the SLMed Inconel 718 specimens, removing the grain-orientation found in as-built and solution annealed. It seems as if the temperature of solution annealing, 1000°C, is not high enough to promote recrystallization in the material, thus leaving the material more brittle than the HIPed specimens. The lower ductility can be seen by comparing the elongation at failure values for the two cases.

It can be observed that the S+A specimens did not contain δ phase, while H+A did, even though they were subjected to the same aging procedure. This is an interesting finding,

considering that the amount δ phase precipitation depends on aging time, as described in 4.1. The absence of δ phase in S+A can possibly be explained by the different temperature and time exposure of the treatment, with respect to HIP-treatment.

When considering the stress-strain results, having in mind the microstructure characteristics, the anisotropy of the microstructure seems to be of minor importance. This is because S and as-built demonstrate different mechanical properties while having the same degree of anisotropy as seen in figure 5.1, leaving the presence of sub-micron cell structures and secondary phases to be the most likely deciding factors. For the solution annealed specimens, the slightly lower σ_{YS} and significantly higher ductility can be related to the dissolution of Laves phase and decrease of dislocation density compared to as-built. The slightly lower σ_{YS} for HIP compared to solution annealed, can again be related to sub-micron cell structures. These cell structures act as barriers for dislocations under monotonic loading.

HIP specimens exhibit the highest ductility and the lowest σ_{YS}. This is due to the full recrystallization, eliminating all microstructural features from SLM process. After aging, the HIPed specimens exhibit an increase in σ_{YS} and σ_{UTS} and decrease in ductility due to precipitation of γ'' phase. For aged condition, the lower strength and higher ductility for HIPed specimens (H+A), compared to solution annealed specimens (S+A), can be explained by the presence of sub-micron cell structures in S+A specimens (they act as barriers for dislocations). In addition, the lower strength and higher ductility for HIPed specimens can be related to the presence of δ phases, which are present at the cost of γ'' phase. These findings are similar to what S. Gribbin et. al. [41] found; when including HIP in the heat treatment process, the specimens exhibit lower strength and higher ductility than solution treated and aged specimens, as illustrated in figure 5.9.

When comparing the results from Aydinöz et. al. [51] with the results for SLMed specimens from NASA [60] in figure 5.18, it can be seen that the stress-strain characteristics are different between the two experiments. Having in mind that of lack of fusion defects led to inferior monotonic properties within the NASA-experiment, it is interesting to see that the defect specimens compare quite well with S+A and H+A specimens in [51]. It can also be seen that the defect-free specimens from NASA are superior in terms of both strength and ductility. An in-depth explanation of this observation is difficult, considering the lack of information regarding the presence of sub-micron cell structures in the NASA experiments. Information about the amount of δ phases present in the NASA specimens is also lacking. Aydinöz et. al. [51] found sub-micron cell structures in the S+A specimens and δ phases in the H+A specimens, and their impact on monotonic properties has already been addressed. It is possible that the more comprehensive heat treatment process at NASA has led to the superior properties, considering that this is the most outspoken difference between the two experiments. However, it is difficult to say exactly what this heat treatment has led to in terms of precipitate phases and other microstructural characteristics, other than eliminating grain orientation, as seen in figure 5.4.
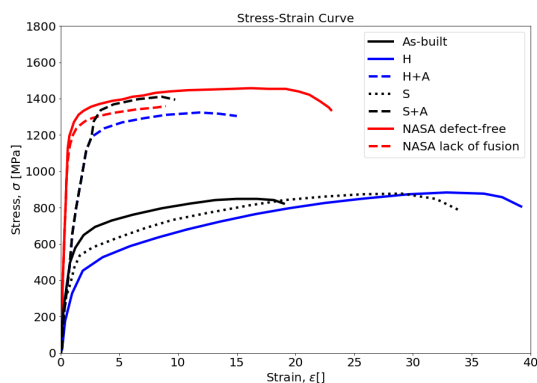
Figure 5.18: Combination of the curves from figure 5.3 and 5.6 (In red).

Al-Juboori et. al. [62], found that the heat treated specimens exhibit higher strength than the as-built specimens, but the elongation at failure is almost the same as for as-built. The increase in strength is in line with the observations made by Aydinöz et. al. [51], but the unaffected elongation at failure is not comparable. The observations in 5.1.5 can be explained by the presence of Laves phase in the as-built specimens, which is known to cause high brittleness. The presence of Laves phase in this case will be discussed further bellow. As heat treatment is carried out, the Laves phase will dissolve and cause an increase in ductility. However, upon heat treatment, the precipitation of γ' and γ'' strengthening phases will also take place, leading to a decrease in ductility. These two phenomena will in essence neutralize each other with respect to the ductility of the material. The higher heat input and lower cooling rates associated with the SLM process, is the most likely explanation to why the material response to heat treatment is different between SLMed and EBMed material.

Build-height dependent properties of EBMed specimens
From the articles involving EBM, mechanical properties of the printed material seems to depend on distance from the build platform.

Al-Juboori et. al. [62] has established a relationship between time, temperature, and build height. From figure 5.19, it can be seen that the temperature of the build platform decreases throughout the building process. The figure also illustrates that the different material layers are held at temperatures close to the building temperature for a different amount of time, with the layer closest to the platform having the longest dwell time. Total building time is not given in the article, but the author indicates that it amounts to several hours [62]. From the time-temperature-transformation diagram in figure 5.20, it can seen that material held at high temperatures for longer time will contain more Laves phase, leaving the layers closest to the building platform with higher content of Laves phase. The building temperature is also high enough (1050°) to expect high content of Laves phase. The author suggests that the building time is long enough to expect formation of γ' and γ'' as well as Laves phase in the intermediate layers of the build, which means that the total building time most likely amounts to tens of hours ,based on the TTT-diagram in figure 5.20.
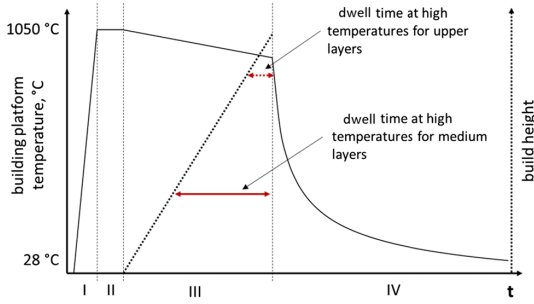
Figure 5.19: Temperature path for the building platform with respect to process-time. The three intervals indicated with roman numbers are: heating of platform (I), holding platform temperature (II), building time (III), and cooling (IV) [62].
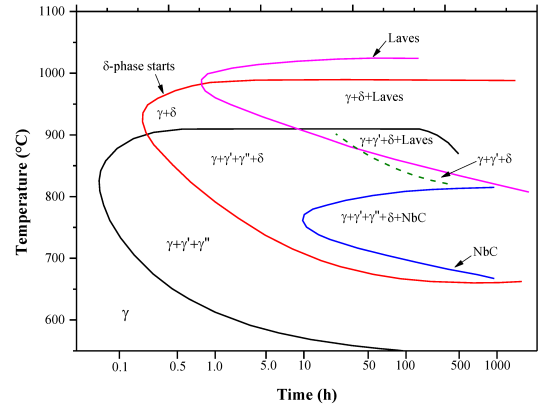
Figure 5.20: TTT-diagram for Inconel 718 [64].

From the tensile test results in reference [63], it is clear that strength and ductility decreases as distance from top of build increases. This is an expected finding, considering that the amount of δ phase increases closer to the build platform. The increasing amount of δ phase closer to the build platform can be attributed to the fact that the lower parts of the build is held at high temperature for a longer time. Consequently, as mentioned in 4.1, δ precipitation increases as aging time increases. It should also be mentioned that the microstructural characteristics in region 1 and 2 have little impact on the results. This is mainly because the two regions span over such a short distance, and thus they will control the mechanical behavior of any of the specimens. The two regions also contain a relatively low amount of δ phase.

With respect to the results in reference [62], it is interesting that no segregation of Laves phase is found in the intermediate areas of the build height in reference [63]. Regarding reference [62], it was discussed that the Laves phase had a substantial impact on the mechanical properties of the material, and that it had segregated due to the time-temperature characteristics of the process. The build-temperature in [63] is 975°C, which may not be high enough to promote segregation of Laves phase, considering the TTT-diagram in figure 5.20. This will of course depend on the building time, and the ability to keep a high temperature throughout the process. Due to the fact that no Laves phases are present, it is likely that the building time is relatively short, and the build-temperature decreases throughout the build.
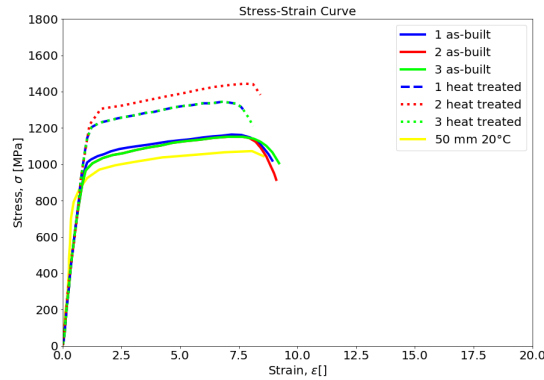
Figure 5.21: Stress-strain curves from figure 5.13 together with room temperature-tested center-specimen from figure 5.17 (yellow).

With respect to elongation to failure, the results in reference [62] are in accordance with the room-temperature tested specimens machined from the center of the plate in reference [63], as seen in figure 5.21. Since the specimens in reference [62] are machined out parallel to the build direction and are almost as long as the total build height, the gauge length of the specimen should have similar characteristics as that of the center-specimens in reference [63]. But these characteristics probably originate from different phenomena, because of the microstructural differences in the two situations. The relatively brittle results in reference [63] are due to the presence of δ phase, while the lack of ductility in reference [62] is due to the presence of Laves phase. It is an interesting observation that two different phenomena lead to almost the same elongation at failure.

Comparing the strength characteristics of the specimens in reference [62] and the center specimens in reference [63], certain differences can be seen. Only considering the room temperature tested specimens, the center specimens in the latter reference generally have a lower strength than the reference [62]-specimens, as seen in figure 5.21. This is most likely due to the absence of heat treatment in reference [63], as the difference is more pronounced when comparing with the heat treated specimens of reference [62]. The increase of strength after heat treatment has been seen in both reference [51] and [63].

The fact that the as-built specimens in reference [62] also exhibit higher strength than the reference [63]-specimens, can possibly be explained by difference in process parameters or other factors influencing the quality of the final build. Taking into account the build direction with respect to load direction, the transversal specimens in reference [63] should in theory exhibit a higher strength than the longitudinal specimens in reference [62]. This difference in strength due to build direction can be seen in reference [65], [66], and [61], where specimens machined perpendicular to the build direction exhibit a higher strength than those machined parallel. This is not observed when comparing reference [63] and [62]. The strength difference of the as-built specimens however is rather small, thus it will not be discussed any further.

An interesting topic for further research would be to heat treat EBMed material that does not contain Laves phase after production, such as the material in reference [63]. This would probably lead to an improvement of properties for the EBMed Inconel 718, considering the findings in reference [62]. Here it was discussed that the Laves phase had such a detrimental effect on mechanical properties and that heat treatment would only neutralize the negative effect of Laves phase. It is therefore suggested to carry out

a similar study as in reference [63] with heat treatment included in the process.

Effect of porostities

Since AMed components often contain porosities in the as-built state, it is important to address the effect of these porosities. In section 4.1, it was stated that hot isostatic pressing (HIP) could be performed in order to remove pores stemming from the AM process. Al-Juboori [62] found that the EBMed specimens contained porosities after printing, and that the amount of porosities depended on the volume energy density (VED). It was observed that high and low VED led to the highest amount of pores. This is in good agreement with the available theory saying that too low energy density leads to lack of fusion pores, and too high energy density leads to keyhole pores [15]. Since the HIP was not conducted as part of the heat treatment, it is reason to believe that the porosities are still present in the heat treated specimens. For the as-built specimens in figure 5.13, the pores doesn't seem to have an impact, but for the heat treated specimens, the specimens with the lowest amount of pores has the highest strength. This can be explained by the fact that heat treatment leads to precipitation of strengthening γ', γ'', and δ phase, thus increasing the strength. These phases are strong and brittle, and it is possible that their presence makes the material more sensitive to the stress-raising pores. This observation underlines the importance of HIP, especially if the amount of pores is high. The effect of lack of fusion pores was also seen in the NASA experiments [60], where these pores led to lower elongation at failure.

Comparison with wrought

In order to evaluate the overall static properties of the specimens included in this review, tensile properties of conventional wrought IN 718 is included. The reference material is taken from Special Metals Corporation [1], and the data for the wrought material is presented in table 5.3.

Material	Heat treatment	σ_{UTS} [MPa]	σ_{YS} [MPa]	Elongation [%]
1	954°C/1h + double aging	1385	1206	20
2	1065°C/1h + double aging	1296	1048	21

Table 5.3: Tensile properties for hot-rolled Inconel 718 bar with diameter of 1 in., tested at room temperature. Data from [1], and converted from [ksi] to [MPa].

Based on the data in table 5.3, the following observations can be made;

- The solution annealed and aged (S+A) SLMed material in figure 5.3 has a slightly higher strength than wrought material 1, but shorter elongation at failure

- The SLMed material from NASA in figure 5.6, has slightly higher strength and longer elongation at failure compared to wrought material 1

- The heat treated DMLSed material in table 5.1, have slightly lower strength and similar elongation at failure compared to wrought material 1

- The heat treated EBMed material in figure 5.13 have higher strength than wrought material 1, but elongation at failure is considerably lower

- The EBMed material in figure 5.17 has lower strength and similar elongation at failure, compared to wrought material 1

From these findings, its seems as if AMed Inconel 718 can reach similar tensile properties to that of wrought Inconel 718, with the right process parameters and post-process heat treatment.

Main findings:

- HIP removes columnar grain structure

- HIP without aging leads to a ductile material

- Aging upon heat treatment for SLMed Inconel 718 leads to higher strength and lower ductility

- Heat treatment of EBMed Inconel 718 leads to higher strength, but not necessarily a more brittle material

- The monotonic properties of EBMed Inconel 718 depend on distance from build platform

- Lack of fusion defects leads to lower elongation at failure

- Effect of porosities have greater impact after heat treatment

- VED influences the amount of porosities present in the material

- δ phase has a detrimental effect on monotonic properties (decreasing the amount of γ'')

- For EBM, build temperature is important with respect to segregation of Laves phase

- AMed Inconel 718 can achieve similar tensile properties to those of wrought Inconel 718

5.2 Fatigue Properties

This section includes a selection of papers and experiments where the fatigue properties of AM Inconel 718 are investigated. Only what is considered to be relevant figures and information is included here, and it is suggested to review each article for further understanding and investigation. Each subsection is given the title of the relevant article or experiment.

5.2.1 The influence of Laves phases on the high-cycle fatigue behavior of laser additive manufactured Inconel 718

S. Sui et al., [53] investigated the effect of Laves phase on the high cycle fatigue properties of Inconel 718. The HCF tests were conducted on fatigue specimens produced by a Powder DED system, where the powder is fed through a nozzle and fused by means of a laser. For comparison reasons, a selection of wrought samples was also fatigue tested. The AMed specimens were printed to their final shape, with a notch geometry of $k_t = 1$, and the building direction with respect to the load direction is not indicated in the paper. After

production, the AMed specimens were subjected to a heat treatment only consisting of double aging; 720°C/8h → FC to 620°C/8h AC. The wrought specimens were subjected to the following heat treatment; 1050°C/1h AC, 980°C/1h AC, 720°C/8h → FC to 620°C/8h AC. HCF tests were conducted at elevated temperature (650°C) and with a load ratio of R=0.1.
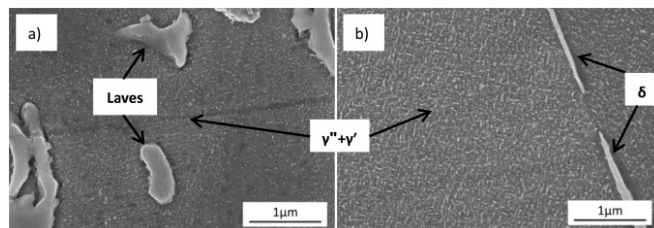
Figure 5.22: Precipitations in (a) AMed Inconel 718, and (b) Wrought Inconel 718 [53].

The results of the micrographs in figure 5.22 show that AMed and wrought specimens contain different combinations of precipitates. The AMed specimens mainly contain Laves phase in addition to γ' and γ'' precipitates, while wrought specimens contain δ phase together with γ' and γ'' precipitates. The difference between γ' and γ'' precipitates in AMed and wrought, is that γ' and γ'' tend to precipitate close to the Laves phase in AMed, while the precipitation is more uniform in the wrought specimens.
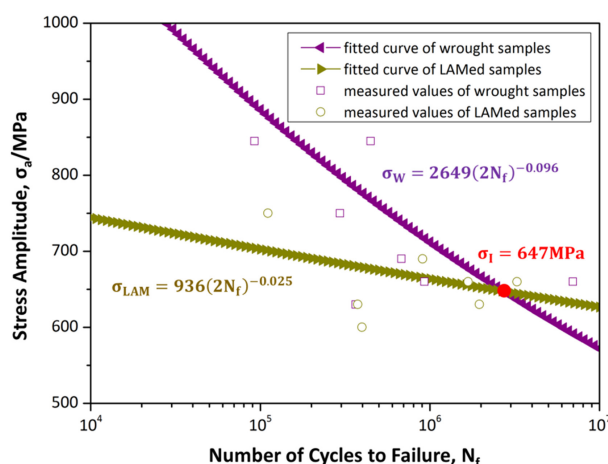
Figure 5.23: S-N curves for AMed and wrought Inconel 718 [53].

The resulting S-N curves in figure 5.23 of the fatigue testing, display an interesting relationship between the fatigue properties of AMed and wrought specimens. The curves indicate different fatigue resistance at high and low stress amplitudes for the two production methods. At low stress amplitudes, the fatigue resistance of the AMed specimens is inferior to that of the wrought specimens, but the AMed specimens have better fatigue properties at lower stress amplitudes. AMed and wrought specimens seems to have the same fatigue resistance at 647 MPa, which can be denoted the transformation stress amplitude.

5.2.2 Technical report from NASA

The high cycle fatigue tests carried out by NASA [60] were done on SLMed specimens with a stress concentration factor of $k_t=1$. The tests were performed at room temperature, employing a load ratio of R=0.1. A reference curve for wrought specimens is also included in the tests. The SLMed specimens were loaded both parallel and perpendicular to build direction, and different surface treatments were carried out on the specimens. Some specimens had a layer of their surface machined away, while others were tested with as-built surface. Surface treatments such as low stress grinding and tumbling + electropolishing were also executed on some of the specimens. Common for all specimens was the post-process heat treatment, which included: stress relief 1165°C/1.5h FC, HIP 1165°C/100MPa/1h AC, solution 1066°C/1h AC, and double aging 760°C/10h → FC to 650°C /20h.
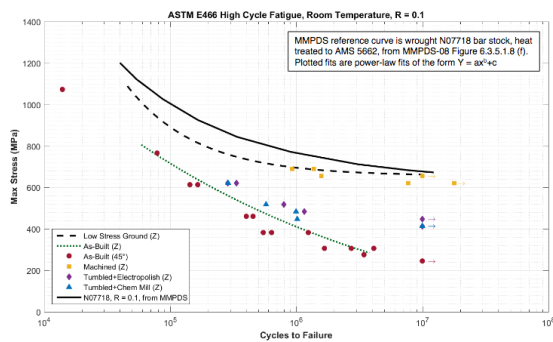
Figure 5.24: S-N curves for SLMed specimens with different post process treatments and wrought as reference, from [60].
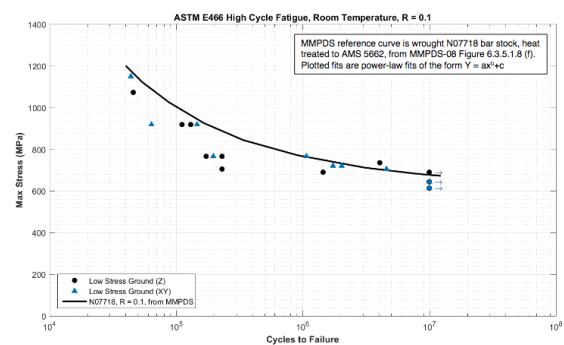
Figure 5.25: Low stress ground specimens loaded parallel (z) and perpendicular (xy) to build direction, with wrought as reference [60].

The S-N curves in figure 5.24 show a clear relationship between surface treatment and fatigue life, with a distinct improvement of fatigue life for surface-treated. The machined and low stress ground and machined specimens exhibited the greatest fatigue strength, while tumbling + electropolishing slightly improved the fatigue resistance compared to as-built. From the curves in figure 5.25, it can also be seen that the low stress ground specimens loaded bot parallel and perpendicular to build direction exhibit the same fatigue strength.

5.2.3 Microstructure and directional fatigue behavior of Inconel 718 produced by selective laser melting

Bending fatigue tests were conducted at room temperature on SLMed specimens with a load ratio of R=0 [67]. In order to study the effect of anisotropic microstructure on HCF properties, the fatigue specimens were built in different directions with respect to the intended loading direction, as seen in figure 5.26. The different build directions are indicated in figure, with the specimen-configurations denoted A, B, and C. After the SLM process, all specimens heat treated with the following steps: stress relief 970°C/1h

argon cooling, double aging 710°C/8h → FC to 610°C/8h argon cooling. The surface of the specimens is not treated after production, i.e. it is kept as-built.
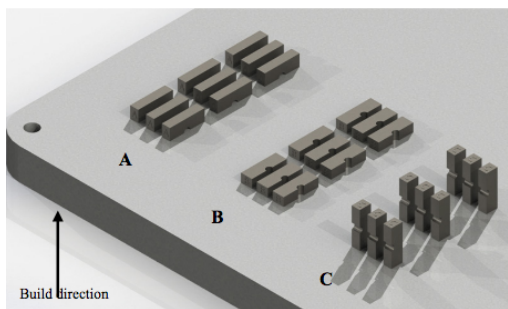
	A	B	C
$R_a[\mu\text{m}]$	6.49	10.67	15.56
$R_q[\mu\text{m}]$	7.58	12.97	19.63
$R_z[\mu\text{m}]$	29.67	56.96	84.43

Figure 5.26: Build orientation of the different specimens [67].

Table 5.4: Surface roughness of the specimens. Data from [67].

The micrographs show a build direction-dependent microstructure in figure 5.27, with grains elongated along the build direction, and equiaxed grain structure seen perpendicular to the build direction. For all specimens, Laves phases, γ'' precipitates and gas pores were found to be present in the material, as seen in figure 5.28. The evaluation of the surface roughness shows a substantial difference between specimens A, B, and C. C-specimens have the highest surface roughness, while A-specimens have the lowest, as seen in table 5.4.
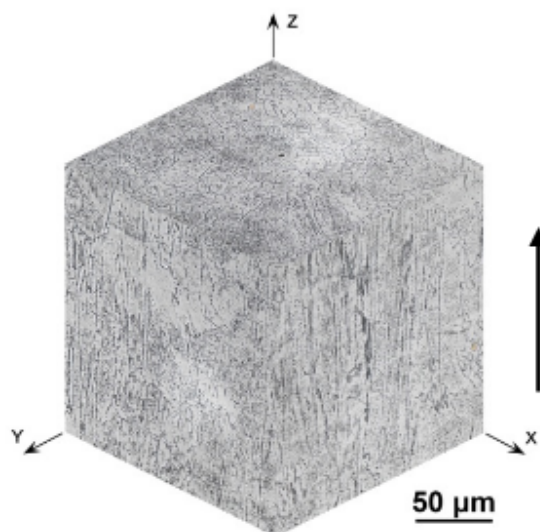
Figure 5.27: Microstructure with arrow indicating build direction [67].
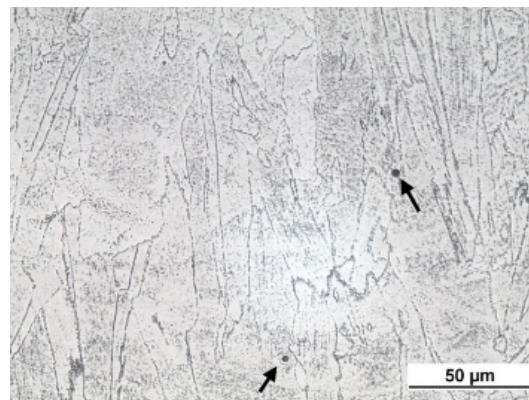
Figure 5.28: Gas pores (indicated with arrows) and precipitations (grey) along and inside grains [67].

In the paper, micrographs showing that the fatigue cracks initiated from defects nearby or on the surface are provided. For the sake of brevity, they are not included here. As can be seen from the S-N curves, A-specimens exhibit the highest fatigue strength, while C-specimens exhibits the lowest.
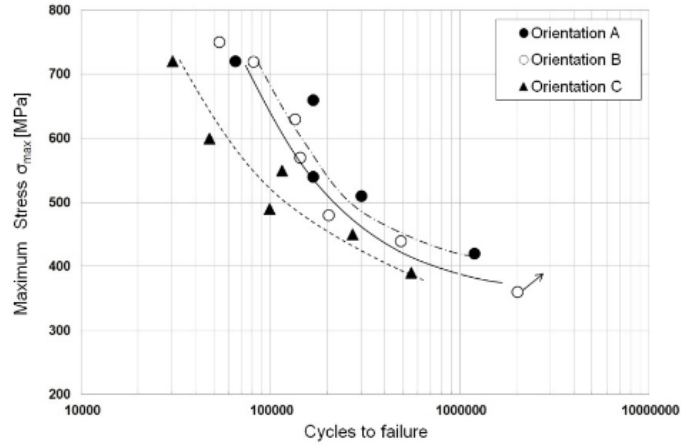
Figure 5.29: S-N curves for AMed and wrought Inconel 718 [53].

5.2.4 Defect analysis and fatigue design basis for Ni-based superalloy 718 manufactured by selective laser melting

The SLMed fatigue specimens in this study [68] were produced by two different SLM-systems, denoted A and B. The micrographs reveal that a larger powder size is used for production of material A compared to B. All specimens were machined from SLMed plates, either parallel (L direction) or perpendicular (T direction) with respect to the build direction. After production, the specimens underwent a heat treatment consisting of stress relief, solution heat treatment, and aging, according with the AMS5663 standard. The fatigue tests were conducted at room temperature with a load ratio of R=-1, using a high frequency tension-compression testing machine.

From the micrographs of both materials, it was observed that fatigue cracks originated from defects in contact with the surface. These defects were mainly gas porosities developed due to lack of fusion in the SLM process. Micrographs also showed that material B contained a higher number of defects than material A. The S-N curves display no dependency on build direction with respect to HCF life. Direction L and T exhibit the same fatigue strength, and this applies for both material A and B. In addition, material B had a slightly lower fatigue strength than material A.

48
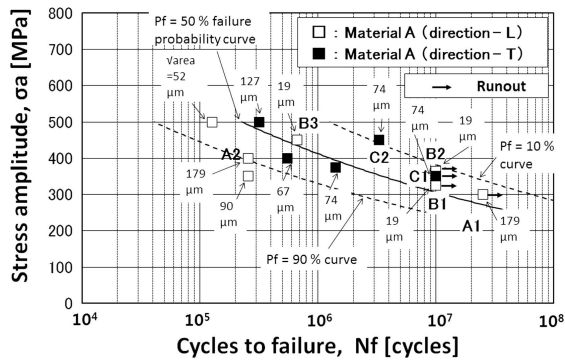
Figure 5.30: S-N curves for L and T direction for material A [68]. (The size measures indicate size of the defect related to fracture).
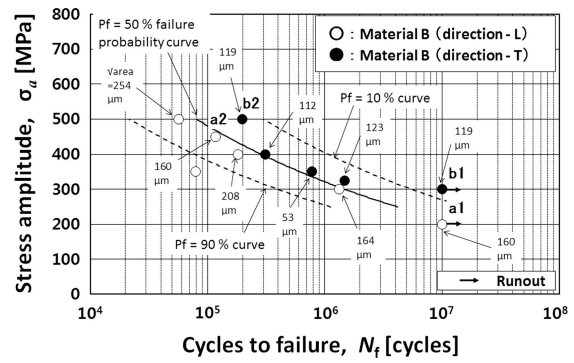
Figure 5.31: S-N curves for L and T direction for material B [68]. (The size measures indicate size of the defect related to fracture).

5.2.5 Notched fatigue testing of Inconel 718 prepared by selective laser melting

Notched specimens were produced by SLM and fatigue tested at room temperature with high frequency, using a load ratio of R=0.1 [69]. Three different notch geometries, and thus three different kt values, were used for the tests; V1, V2, and U, where all specimens were built both vertically and horizontally with respect to the build platform, as seen in figure 5.32. When printed vertically, supports were used inside of the notches. This is done because SLM has limitations when it comes to building surfaces with an incline less than 45° to horizontal. A number of V2 geometries were also produced by printing rectangular specimens and machining them into final shape. Similar to the other specimens, these rectangular specimens were also printed in both vertical and horizontal direction. Wrought specimens are also included in the tests. After production, all specimens underwent the following heat treatment: HIP 1163°C/3h 100MPa, solution annealing 954°C with quenching, double aging 718°C/8h → FC to 621°C/10h. Wrought specimens did not undergo HIP.
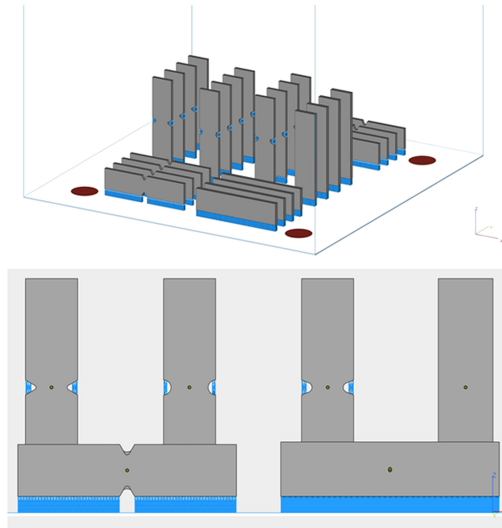
Figure 5.32: Orientation of specimens with respect to build platform [69]. Build direction is along z-axis.

After printing the specimens, the actual kt values were measured for all specimens by studying the notch root. The results gave values close to the intended k_t values, with some exceptions; horizontal specimens with the highest intended k_t had a lower actual k_t, and all vertical specimens generally had a higher actual k_t than the intended one. With respect to the surface roughness of the specimens, it was observed that the downward facing notch in the horizontal specimens had a significantly rougher surface. The S-N curves generally illustrate little difference in fatigue life for horizontal and vertical specimens with same notch geometry, even though vertical specimens have kt values higher than intended k_t, as can be seen for V1 and V2 specimens in figure 5.33. The machined specimens exhibit a higher fatigue strength than all the other specimens, regardless of geometry. This is illustrated in figure 5.34.
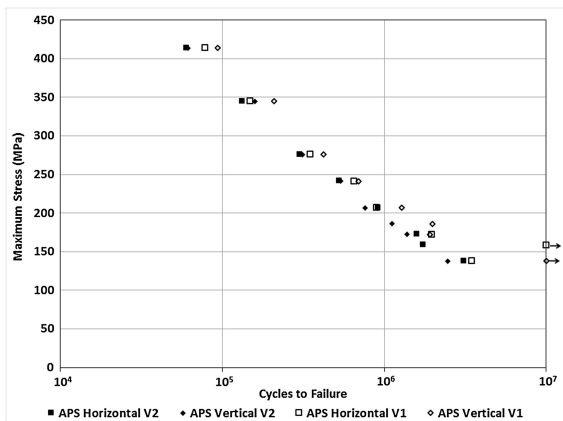
Figure 5.33: S-N curves for as produced surface (APS) for horizontal and vertical V1 and V2 notches [69].
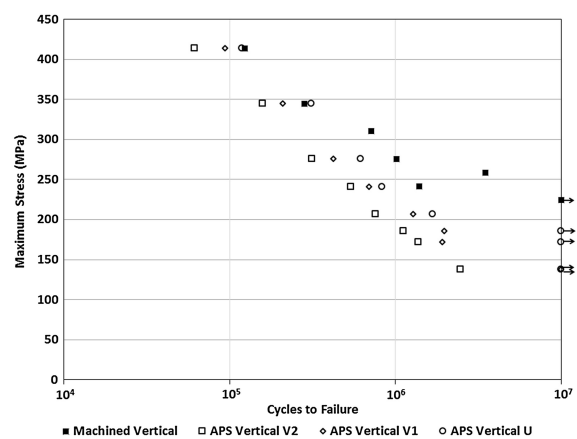
Figure 5.34: S-N curves for all vertical specimens, including machined [69].

5.2.6   Discussion

Effect of surface roughness

In reference [67], the effect of load direction with respect to build direction on HCF was determined for SLMed Inconel 718. A clear relationship between building direction and fatigue strength was established, with specimens built perpendicular to build direction exhibiting the highest fatigue strength. However, this result should be discussed with respect to both surface quality and grain structure, since these aspects are the main differences between the samples built in different directions. Considering that the correlation between surface finish and fatigue strength is so pronounced, its influence on HCF must be addressed. Recalling the results in reference [60], where surface treated specimens exhibited higher fatigue strength compared to as-built surface, it is reason to believe that the influence of surface roughness is decisive. The negative effect of rough surface finish on HCF has also been reported elsewhere [70]. Lewandowski et al. [71] reported a comparison between HCF properties for as-built and machined surfaces of AMed components, as seen in figure 5.35. From the figure it can be seen that the machining procedure has positive effects with respect to HCF properties.
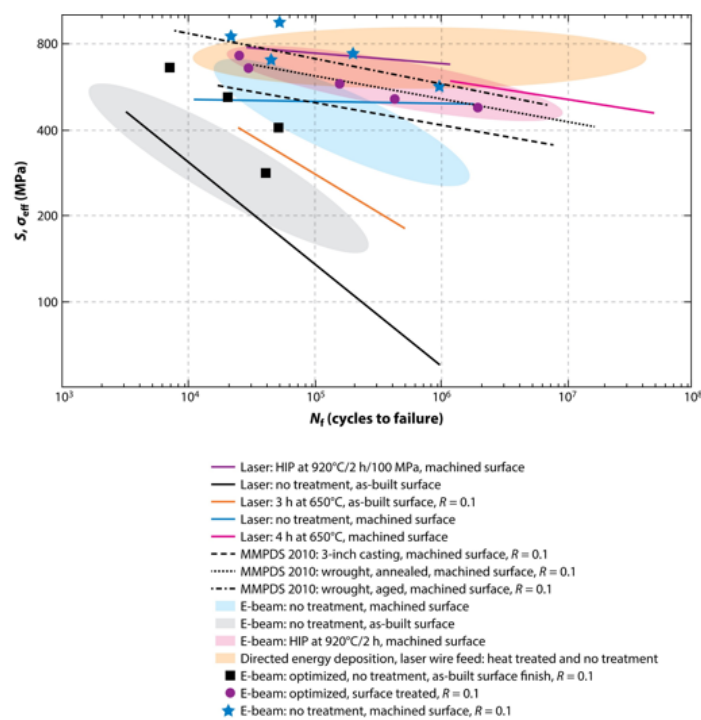
Figure 5.35: S-N curves for AMed and wrought specimens with different surface treatments and heat treatments [71].

The results from reference [69], seen in section 5.2.5, also indicate a relationship between fatigue strength and surface roughness. It can be observed that specimens with the same notch geometry exhibit the same fatigue strength, regardless of whether they are built vertical or horizontal. This may sound contradictory, having in mind that vertical specimens had higher measured k_t values than the intended k_t. However, it was also observed that the downward facing notches in the horizontal specimens had a rougher

surface. Consequently, it seems as if the higher k_t in the vertical specimens, and the rougher surface in the horizontal specimens have a similar detrimental effect on fatigue strength on a given specimen. In effect, the resulting fatigue strength is the same for the two orientations. This assumption can be further justified by studying the specific U-notched specimens. The U-notched specimens were the only specimens where a slightly different fatigue life could be observed for horizontal and vertical specimens, with vertical specimens having the highest fatigue strength. Horizontal U-notches contained the same rough-surfaced bottom notch as the other specimens. However, the U-notched specimens had the smallest difference in k_t values between horizontal and vertical specimens, leaving the effect of the surface roughness more decisive than the k_t, leading to a slightly higher fatigue strength for the vertical specimens. Of all the tested specimens, the machined specimens exhibited the highest fatigue strength, further demonstrating the effect of surface roughness on fatigue life.

Effect of Laves phase
S. Sui et al., [53] studied the relationship between the presence of Laves phases and the HCF properties was studied. From the results it was observed that Laves phases had a detrimental effect on fatigue properties during high stress amplitudes, while it led to better fatigue properties at lower stress amplitudes. High and low stress amplitudes are defined as stresses above and below the transformation stress amplitude (647 MPa), respectively. Due to the different mechanical properties of the Laves phases compared to the rest of the material, the Laves phases is expected to lead to local stress concentrations. The irregular distribution of γ'' will further promote this localization of stress. In the crack initiation stage, the stress concentration seemed to be of little importance, independent on the applied stress, but it had major impact on the crack propagation stage.

During the stage of crack propagation, the structure of the Laves phases changed with changing stress amplitude. The low stress amplitudes did not result in stress concentrations high enough for changing the original morphologies of the Laves phases. However, higher stress amplitudes caused the Laves phases to fragment, creating microscopic cracks and holes. These cracks and holes made it easier for cracks to propagate, leading to inferior HCF resistance for AMed Inconel 718 specimens at high stress amplitudes, compared to that of wrought. For the low stress amplitudes during crack propagation, the Laves phases acted as barriers for the fatigue cracks. The low stress concentrations associated with low stress amplitudes were not able to break up the Laves phases, thus leaving the fatigue cracks to stop at the Laves phases and detour around them. This phenomenon is what causes the AMed specimens to have superior fatigue resistance than that of wrought specimens for lower stress amplitudes. It should be mentioned that the δ phase present in the wrought specimens also has the ability to hinder crack propagation. However, based on the results in this present study, it seems as if the Laves phases holds this ability to a higher extent when the stress amplitude is small.

Effect of porosities
In reference [68] porosities, such as those crated by lack of fusion, were observed in the material, and the cracks seemed to initiate from the porosities that were located at the specimen surface. The S-N curves showed no difference in fatigue strength for the two specimen orientations, T and L. However, the specimens produced by machine B exhibited a lower fatigue strength than A-specimens, which can be related to the number of defects in the two materials. Material B did in fact contain more defects than

material A. Considering that this is the only substantial difference between A and B, it the most reasonable explanation for the difference in fatigue strength. These porosities could probably have been removed by a proper HIP treatment. This may sound paradoxical, considering that it was discussed in section 5.1.1 that HIP only removed internal pores, and not those close to the surface. However, in this study, specimens were machined from SLMed blocks and not printed directly into final shape. This implies that the surface pores found on the specimens, are corresponding to the internal porosities of the blocks. Therefore, HIP could have been done before machining the specimens in order to remove these defects, and thus increase the fatigue strength of the material.

Considering that most pores are located close to the surface of the AMed specimens [51], it is reason to believe that the improvement of fatigue properties after machining is somehow related to the removal of pores. Meaning that the improvement of surface roughness is not the only factor to be considered after a machining procedure. In references [60] and [69], as well as in figure 5.35, it is observed that machining has a positive impact on the fatigue properties.

Effect of build direction
In reference [68] the specimens underwent heat treatment including HIP, and it is reason to believe that the grain structure is equiaxed, recalling the results from section 5.1.1. This leaves the material to be without an anisotropic behavior. From the S-N curves in both figure 5.30 and 5.31, it is clear that the fatigue behavior does not depend on the build direction of the specimens. The same observation is done in reference [60], where the heat treated specimens exhibit similar fatigue strength regardless of build direction. In this case, the heat treatment also included HIP, leading to an isotropic material. For the specimens in reference [69], fatigue properties with respect to build direction was also investigated. These specimens were also subjected to HIP, leading to an isotropic material, and the fatigue properties were previously discussed to be governed by surface roughness and notch geometry.

In reference [67] the specimens were built in different directions with respect to the applied load. After heat treatment, which did not include HIP, the grain structure exhibited a clear anisotropic orientation with elongated grains in the build direction. This will in effect lead to different load situations for the specimens with respect to grain orientation. For specimens A and B, the load direction is parallel with the material layers, which means the load is perpendicular to the columnar grains. For specimen C, the direction of the load is parallel with the columnar grains. It was previously discussed that the difference in fatigue strength for the specimens is related to the surface roughness, since the surface roughness of the specimens is different. In addition, the specimens with the finest surface exhibit the best fatigue life, while the specimens with the roughest surface had inferior fatigue life. In order to determine the effect of the anisotropic microstructure, it is reasonable to compare the specimens with similar grain orientations, namely specimen A and B. Recalling the data from table 5.4, the B specimens exhibit a rougher surface than the A specimens. Since the A specimens exhibit superior fatigue properties to that of B, and the grain structure is fairly similar, it is reason to believe that the surface roughness has a larger impact on the fatigue properties than the anisotropic microstructure.

For a more in-depth study of the effect of anisotropic material on HCF properties, a study including specimens with clear material anisotropy and same surface roughness should be carried out. M.M Kirka et al., [49] has investigated the effect of anisotropy on the LCF

properties, and found that anisotropy impacts the LCF properties of the specimens.

Main findings:

- Laves phase can improve fatigue properties at low stress amplitudes

- Laves phase is detrimental to fatigue properties at high stress amplitudes

- Porositites have a detrimental effect on fatigue properties

- Surface roughness is a deciding factor in determining the fatigue strength of a specimen, with rough surface leading to inferior fatigue strength

- Surface treatment and machining can improve the fatigue strength of a component

- By performing heat treatment at sufficient temperatures, the grains become equiaxed, and the fatigue properties are not affected by build direction

- The effect of build direction needs further investigation in terms of the effect of grain orientation and anisotropic material

6 Experimental Details

In this chapter, the setup for the physical tests of the additively manufactured Inconel 718 specimens is presented. The test geometries as well as material properties will be presented, together with a description of the test-parameters.

6.1 Specimens

During the course of this work, two specimen geometries were fatigue tested. The specimens were produced at an external company by means of SLM, using the same process parameters. The two given parameters are $VED = 60 J/mm^3$ and a layer thickness equal to 50 μm. The geometry of the specimens is illustrated in figure 6.1. The specimen to the left is referred to as the unnotched, or plain specimen, while the specimen to the right is referred to as blunt V-notched. Table 6.1 shows the dimensions of the geometries.
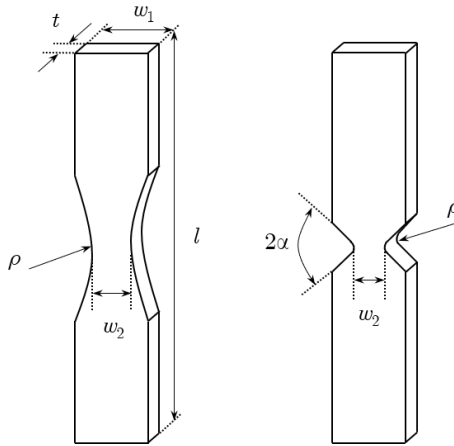
Figure 6.1: Unnotched (left) and blunt V-notched specimen (right).

Specimen	t [mm]	w_1 [mm]	w_2 [mm]	l [mm]	ρ [mm]	2α [°]
Unnotched	5	15	7.000	80	30.31	-
Blunt V-notched	5	15	5.828	80	1.000	90

Table 6.1: Dimensions of the unnotched and V-notched specimens.

All specimens were printed perpendicular to the building platform, along the specimens' length axis, and they were printed directly to their final shape without being machined. All surfaces were also kept as-built, without any form of surface treatment. Figure 6.2 shows the specimens with building direction indicated.
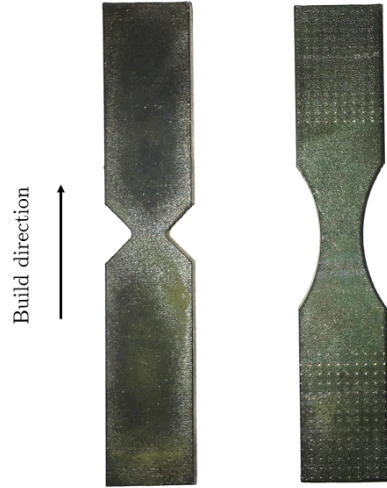
Figure 6.2: The blunt V-notched (left) and unnotched (right) AMed Inconel 718 specimens.

Heat Treatment

After production, the specimens underwent heat treatment consisting of an annealing step followed by a double aging process. Between the two aging steps, the temperature in the oven was reduced at a constant rate of $50°C/h$. The heat treatment process is summarized by the following steps: 1095°C/1h/AC + 720°C/8h/FC $\rightarrow$ (50°C/h) $\rightarrow$ 620°C/8h/AC. In this context, AC is air cooling and FC is furnace cooling. The schematic representation of the heat treatment steps is represented in figure 6.3.
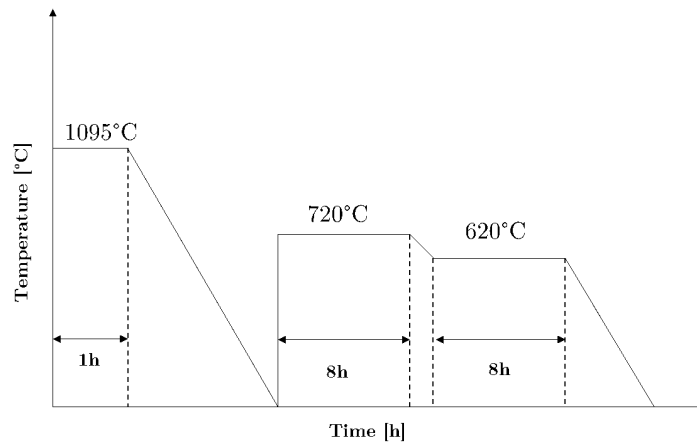
Figure 6.3: Schematic representation of the heat treatment process.

Surface Roughness

In order to investigate the surface roughness of the specimens at different regions, the Alicona Infinite Focus Microscope was used. The surface was measured on three different regions of one heat treated blunt V-notched specimen, along lines of approximately 2 mm. For each region, the roughness was measured in two different directions and along three lines for each direction. The three measured values were averaged and are reported in table 6.2. The regions and measuring lines are shown in figure 6.4, where the local directions are also indicated. From the results it can be seen that the overhang surface,

which has a 45° angle facing towards the building platform, has the highest surface roughness values.

	Front		Downward		Upward	
Direction	t	l	t	l	t	l
Average roughness, Ra [μm]	1.29	1.81	3.99	3.98	1.61	1.86

Table 6.2: Dimensions of the unnotched and V-notched specimens.
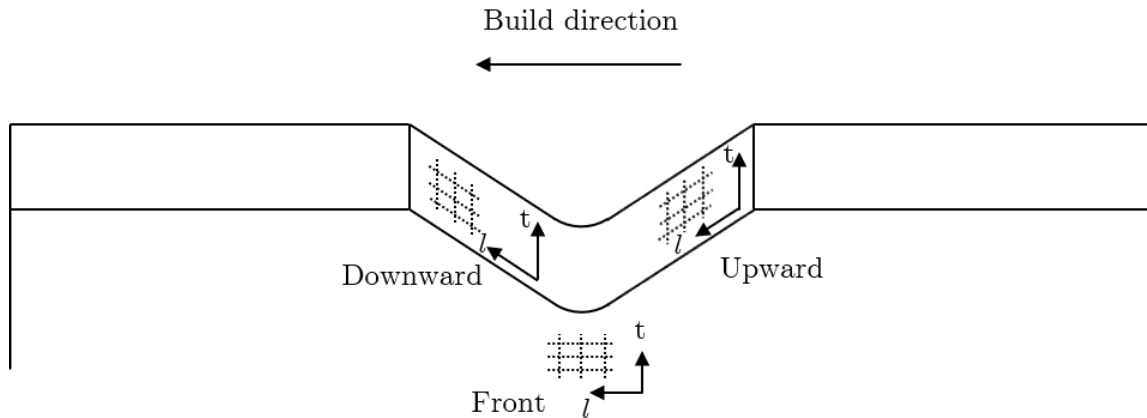
Figure 6.4: The three regions; Overhang, Front and Upward, where the surface roughness was measured in both the longitudinal (l) and transversal (t) direction. The dotted lines indicate the measuring lines. Building direction is also indicated.

Microstructure

The microstructure of one heat treated and one as-built specimen were analyzed using the Olympus BX53M optical microscope. This was done by first cutting the specimens with the Struers Accutom-50 cutting machine, and then polishing with SiC paper and diamond paste down to a final grit size of 1 μm. After polishing, etching of the surfaces was performed according to the ASTM standard [72] using a mixture of Cu2Cl, ethanol and HCl. The microstructure in three planes of the as-built specimen is shown in figure 6.5
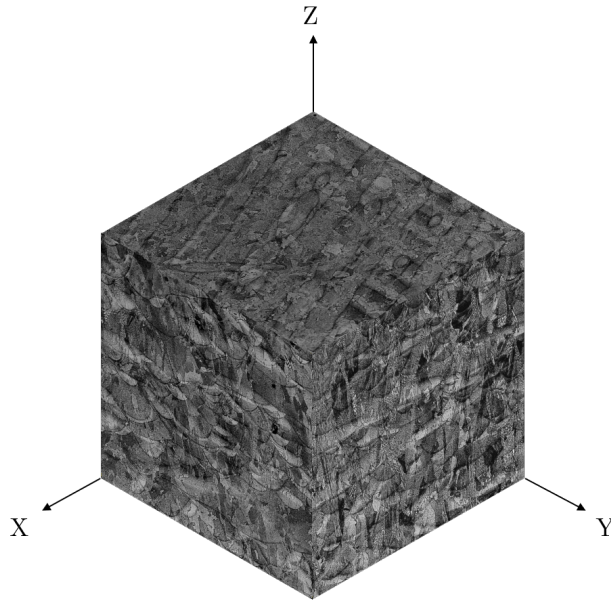
Figure 6.5: As-built microstructure shown in three planes. Z is build direction, and the xy-plane is the cross-section of the specimen.

(a) zx-plane
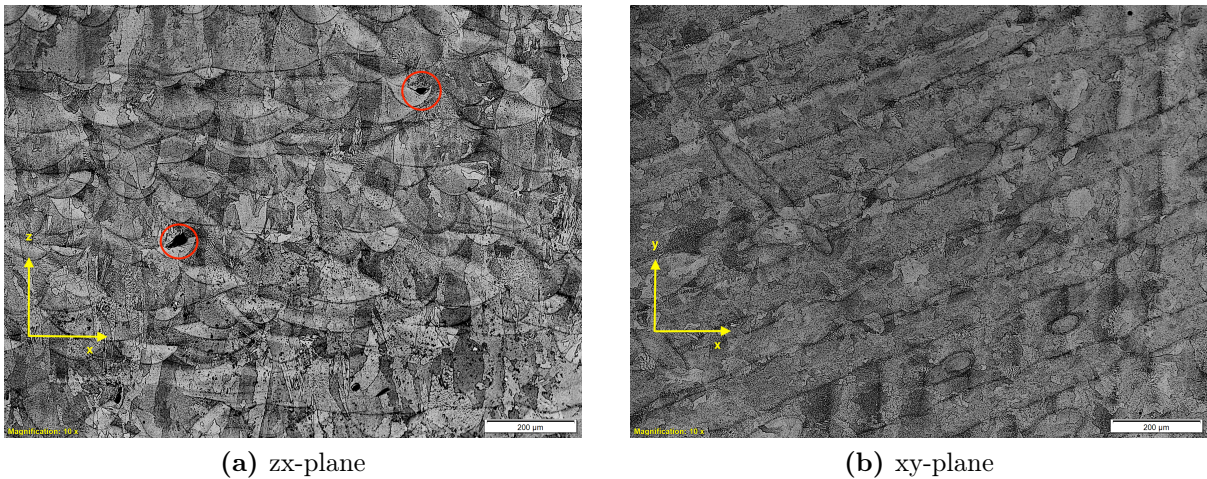
(b) xy-plane

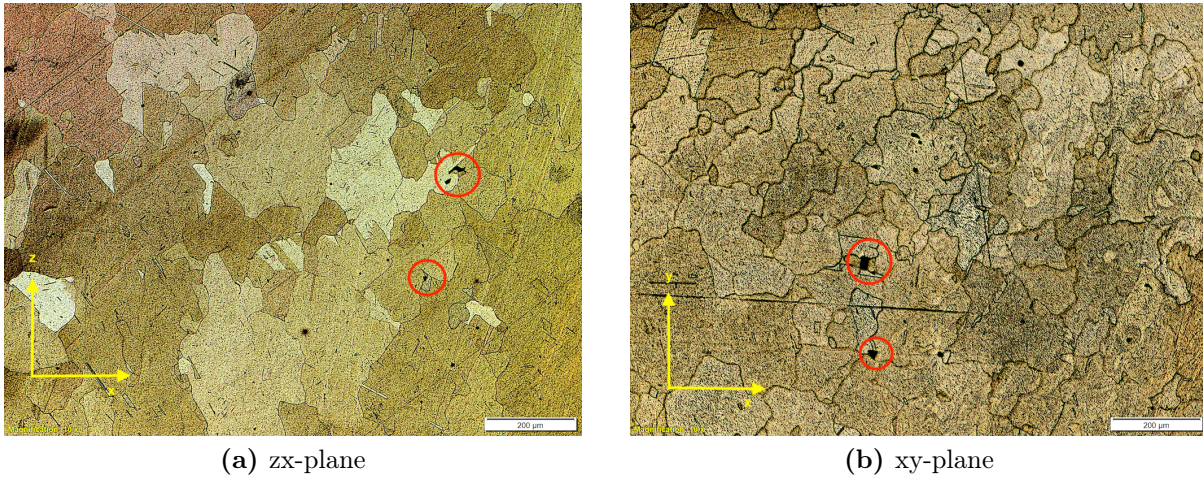**Figure 6.6:** Microstructure of the as-built specimen seen in two planes. Z is build direction, and the xy-plane is the cross-section of the specimen.

The micrographs in figures 6.6a and 6.6b show the microstructure of the as-built specimen in two planes, and visualize both grain orientation and characteristic features stemming from the printing process. Figure 6.6a shows the zx-plane of the specimens and visualizes how the layers are added layer-by-layer in the z-direction, or building direction of the specimen, with the melting pools also visible. In terms of the grain orientation, the micrograph reveals that the grains are columnar with an elongation in the build-direction, perpendicular to the material layers. Lack of fusion porosities stemming from the printing process, such as the ones found in reference [60], are highlighted with red circles.

The microstructure in the cross section of the as-built specimen is illustrated in figure 6.6b, and show the hatching lines from the AM process. The use of hatching lines was

58

described in section 2.3. The grains in the cross section of the specimen are not elongated in any particular direction, as was seen in figure 6.6a, but are equiaxed without any specific orientation.
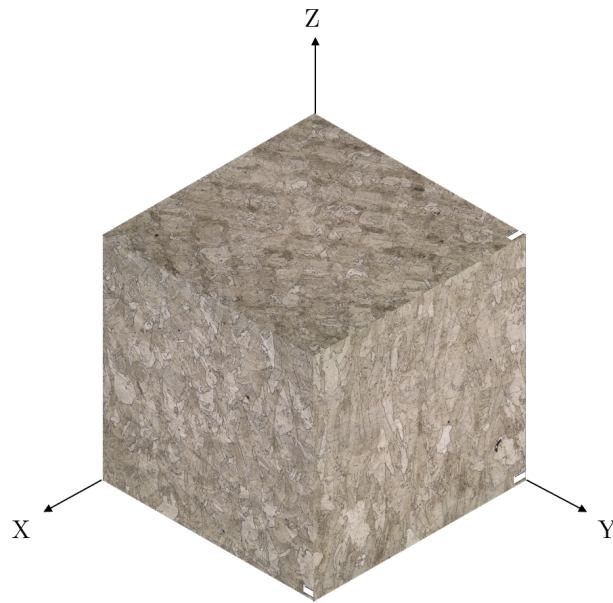
Figure 6.7: Heat treated microstructure shown in three planes. Z is build direction, and the xy-plane is the cross-section of the specimen.

(a) zx-plane
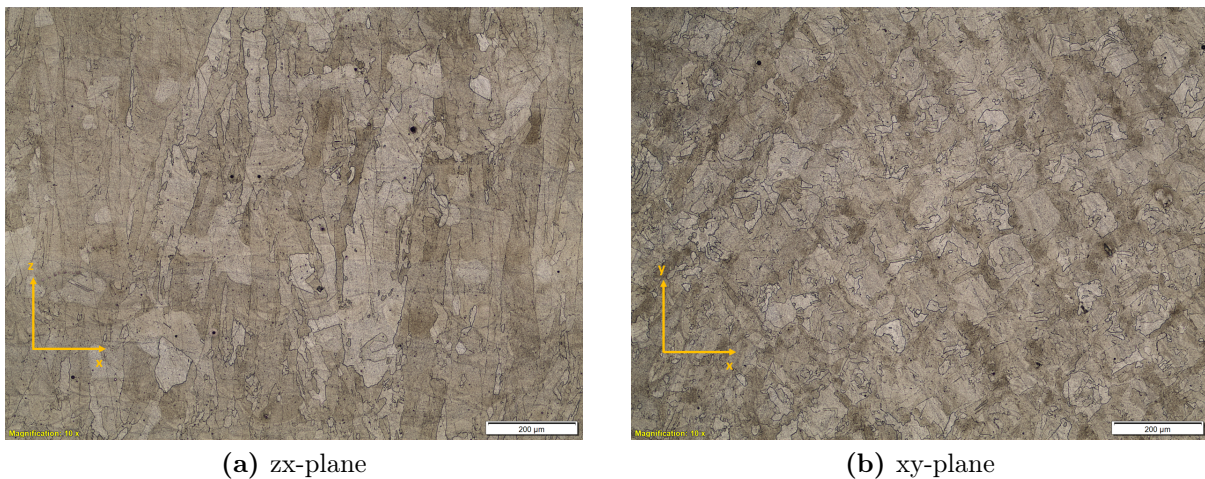
(b) xy-plane

Figure 6.8: Microstructure of the heat treated specimen seen in two planes. Z is build direction, and the xy-plane is the cross-section of the specimen.

The microstructure in the three planes of the heat treated specimen is shown in figure 6.7. Figure 6.8a and 6.8b show the microstructure of the heat treated specimen in the zx- and xy-plane, and reveal that the microstructural features differs compared to the as-built specimen. Both micrographs show that the microstructural features stemming from the AM process, such as building layers, melt pools and hatching lines are almost removed by the heat treatment. In figure 6.8a, the building layers are not visible, but some of the melting pools can still be seen. In the cross section of the specimen, shown

in figure 6.8b, the hatching lines are still visible, but they are less distinct compared to the as-built microstructure in figure 6.6b.

In terms of the grains, it seems as if the grain size has generally increased after heat treatment, but it should be pointed out that no accurate measure was carried out. The orientation of the grains seems to be fairly similar to what was seen for the as-built specimen. In figure 6.8a the grains are still elongated in the build-direction, as was seen for the as-built specimen in figure 6.6a. The micrograph of the cross section in figure 6.8b reveals that the grains are still equiaxed after heat treatment.

Figure 6.9 show that porosities are still present after the heat treatment process.
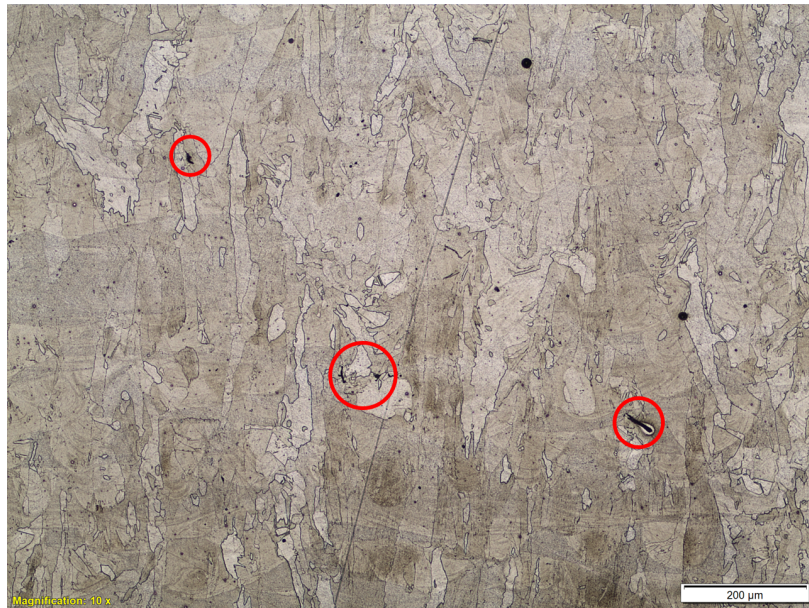
Figure 6.9: Defects in the heat treated specimens.

6.2   Static Testing

In order to investigate the static properties of Inconel 718, two tensile specimens were tested by means of static tensile tests. These specimens were delivered in the same batch a the ones used for fatigue testing, and has identical printing parameters. The geometry of the specimens are designed with reference to standard specimens defined by ASTM-E8 standard [73], and they underwent a similar heat treatment to the one described in section 6.1. The only difference is the temperature of the annealing step, which was set to 1200 °C for the tensile specimens. The specimen geometry is illustrated in figure 6.10, and the dimensions are shown in table 6.3. Figure 6.11 shows the microstructure of one of the heat treated tensile specimens. It can be seen that the grains are equiaxed in both planes, and it seems as if the grain size has increased even more with respect to the heat treated fatigue specimen, whose annealing temperature was 1095 °C. Pores are still present after the heat treatment, and are indicated with red circles.
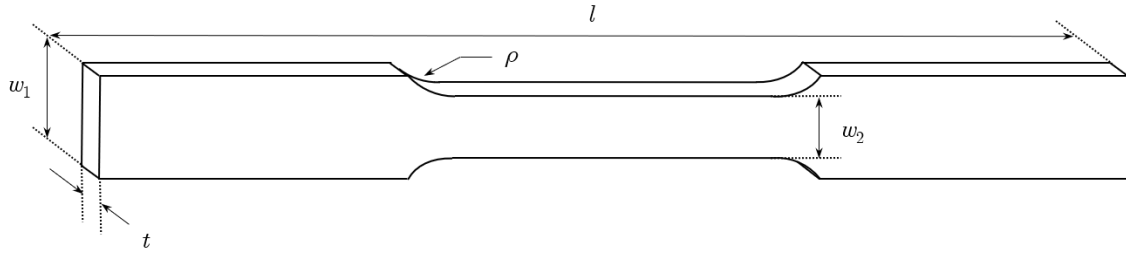
Figure 6.10: Geometry of tensile specimen.

Specimen	t [mm]	w_1 [mm]	w_2 [mm]	l [mm]	ρ [mm]
Tensile Specimen	3	10	6	100	6.000

Table 6.3: Dimensions of the unnotched and V-notched specimens.

(a) zx-plane

(b) xy-plane

Figure 6.11: Microstructure of the heat treated tensile specimen seen in two planes. Z is build direction, and the xy-plane is the cross-section of the specimen.

The two specimens were tensile tested at room temperature with identical test parameters in the MTS 370.10 50kN Load System, using a displacement rate of 10 mm/s. The tests were performed without an extensiometer, meaning that the yield strength and Young's Modulus are not measured accurately.

6.3 Fatigue Testing

The high cycle fatigue properties of the unnotched and blunt V-notched specimen were determined by means of uniaxial fatigue testing. This was done at room temperature and with a force controlled load, using an MTS Landmark Servohydraulic Test System. The loading amplitude was kept constant for all tests and was applied in a sinusoidal manner with a frequency of 10 Hz. At the beginning of the tests, the load was increased to mean load before the cyclic loading started.

For each test, the maximum and minimum load were applied in such a way that the load ratio $R = F_{max}/F_{min}$, or $R = \sigma_{max}/\sigma_{min}$, was equal to zero. This means that the minimum force had a value of 0 for all tests, avoiding compression stresses in the specimens.

7 Results

In this chapter, the results from the physical tests of the AMed Inconel 718 specimens are presented. Both the static and fatigue results are included.

7.1 Static

The resulting stress-strain curves from the tensile tests of the two heat treated specimens are shown in figure 7.1. The results reveal that the ductility of the two specimens are slightly different, as one specimen has shorter elongation at failure, whereas the strength is very similar. The fracture locations of the two specimens are visualized in figure 7.2 and reveal that the fracture location is not the same for the two specimens.
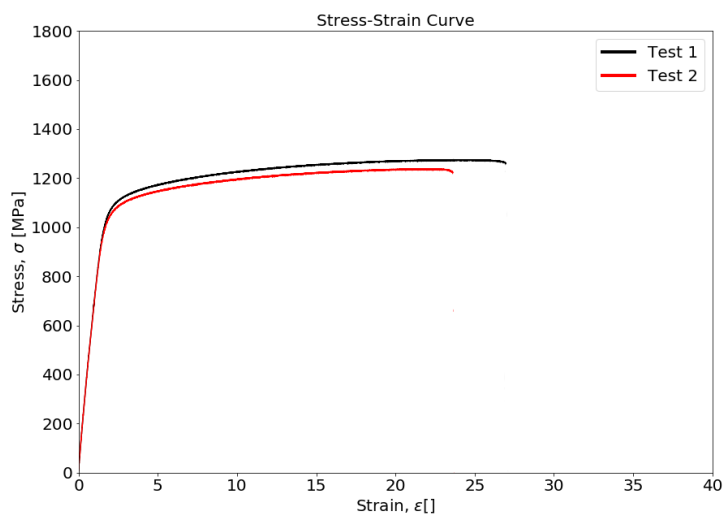
Figure 7.1: Stress-strain curves for the two tensile specimens.
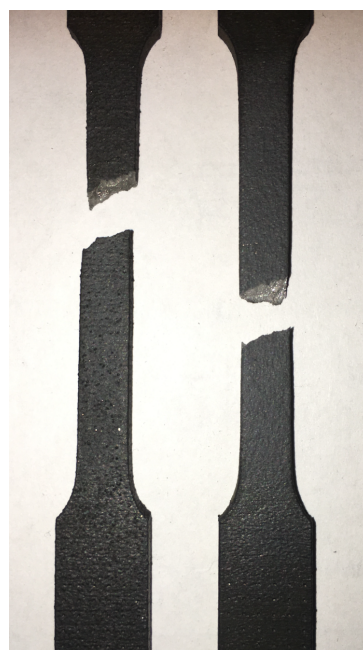
Figure 7.2: Fracture location of the two tensile specimens.

7.2 Fatigue

The results from the fatigue testing of the heat treated unnotched and blunt V-notched specimens, described in section 6.3, are shown in figure 7.3. The scatter data is plotted in log-log scales in an SN-diagram, with nominal stress range on the y-axis and number of cycles to failure on the x-axis. 2×10^6 cycles to failure is set as the fatigue limit, and

63

specimens with higher number of cycles to failure than the fatigue limit are considered as run-out. These specimens are indicated with an arrow in the SN-diagram.
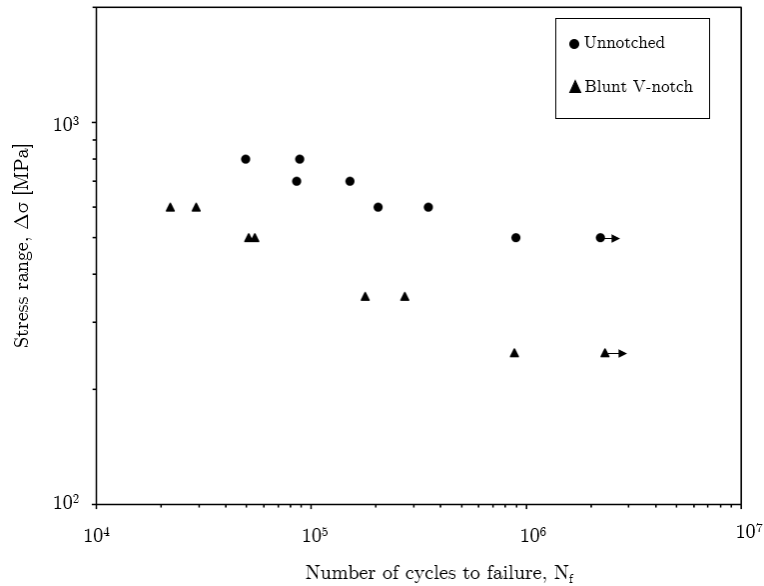
Figure 7.3: Fatigue data of the heat treated unnotched and blunt V-notched specimens.

In figure 7.4, the fatigue data of the unnotched and blunt V-notched specimens are plotted together with their 10%, 50% and 90% confidence bands. These confidence bands represent the probability of survival, and does not include the run-out specimens. From the 10% and 90% confidence bands, the scatter parameter, $T_{\Delta\sigma}$, can be defined. The scatter parameter describes the amount of scatter in the data, and is defined by equation 7.1. The inverse slope, k, is also included, and defines the slope of the confidence bands. The values for the confidence bands at 2×10^6 cycles to failure are shown in table 7.1. The results show that the unnotched specimens have higher fatigue strength, and that the scatter in the fatigue data is higher than that of the blunt V-notched. In addition, the slope of the confidence bands of the unnotched specimens is lower than that of the blunt V-notched.

$$T_{\Delta\sigma} = \frac{\Delta\sigma_{10\%}}{\Delta\sigma_{90\%}} \tag{7.1}$$
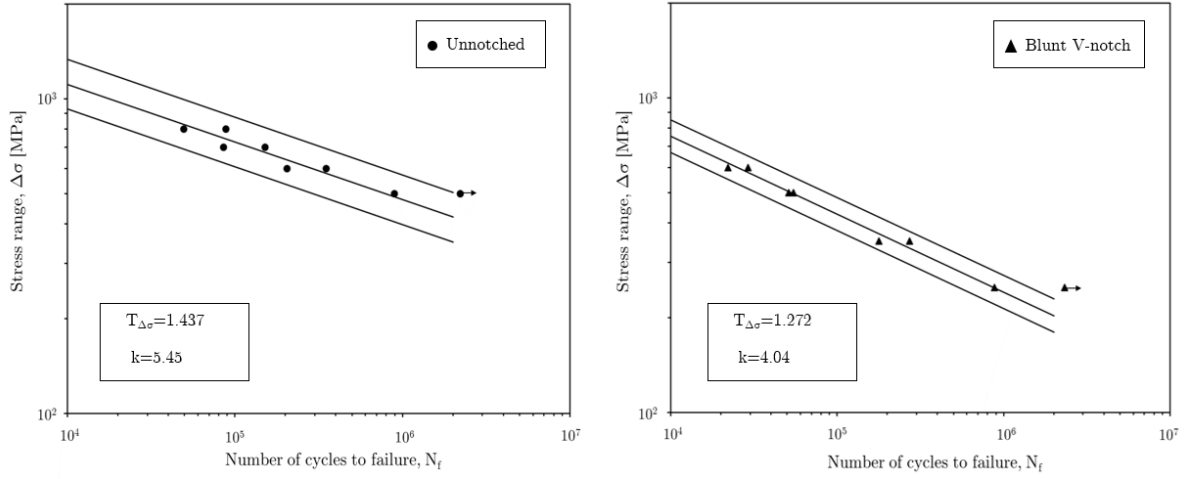
Figure 7.4: Fatigue data for the unnotched (left) and blunt V-notched (right) including the 10%, 50% and 90% confidence bands.

Specimen	$\Delta\sigma - 90\%$	$\Delta\sigma - 50\%$	$\Delta\sigma - 10\%$
Unnotched	350.83	420.54	504.10
Blunt V-notched	180.16	203.22	229.24

Table 7.1: Values for confidence bands at 2×10^6 cycles to failure.

8 The Theory of Critical Distances

In this chapter, the PM and LM stress based approaches of the TCD will be applied on the fatigue data of AMed Inconel 718. First, the approaches will be used on as-built AMed Inconel 718 specimens that where fatigue tested by Solberg and Berto [17]. These specimens were delivered in the same batch as the heat treated specimens presented in section 6.1, and include two additional geometries. The PM and LM will first be used to determine the critical distance values of the as-built specimens. Then, the accuracy of the PM and LM in terms of fatigue limit predictions will be evaluated. Thirdly, the PM is applied to create a modified set of fatigue data.

After applying the TCD approaches on the as-built specimens, the PM and LM will be applied on the heat treated specimens from section 6.1, in order to determine the effect of heat treatment on the critical distance values of the AMed Inconel 718 specimens. The next section will briefly summarize the geometric features and fatigue properties of the as-built specimens tested by Solberg and Berto, as well as the numerical calculations needed for the TCD calculations.

8.1 Background

In this section, the necessary information needed for applying the PM and LM is introduced. This includes fatigue data from physical tests, as well as numerical calculations for determining the stress fields of the specimens.

8.1.1 Data From Literature

As previously mentioned, the as-built specimens tested by Solberg and Berto [17] includes two geometries in addition to the heat treated geometries introduced in section 6.1. These specimens are referred to as sharp V-notched and semicircular and they are illustrated in figure 8.1, together with the blunt V-notched and unnotched specimens. The dimensions of the specimens are given in table 8.1.
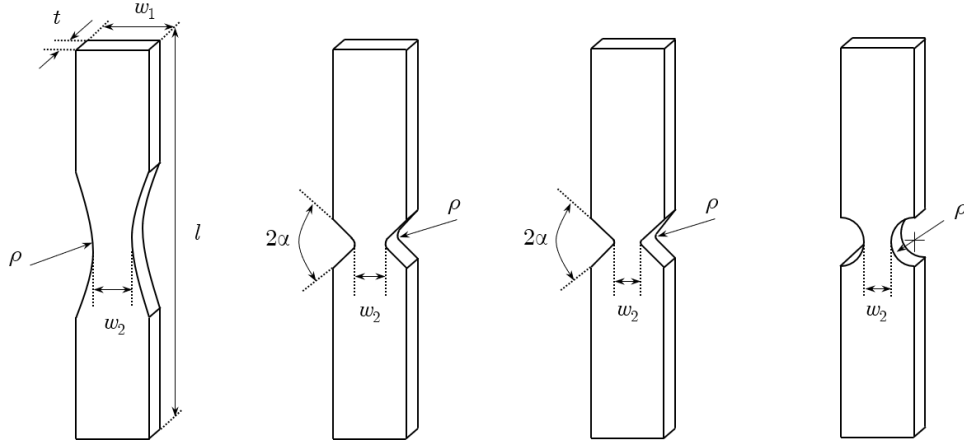
Figure 8.1: Unnotched, blunt V-notched, sharp V-notched and semicircular specimens, from left to right.

Specimen	t [mm]	w_1 [mm]	w_2 [mm]	l [mm]	ρ [mm]	2α [°]
Unnotched	5	15	7.000	80	30.31	-
Blunt V-notched	5	15	5.828	80	1.000	90
Sharp V-notched	5	15	5.083	80	0.100	90
Semicircular	5	15	5.000	80	5.000	-

Table 8.1: Dimensions of the four as-built specimens.

The fatigue tests performed by Solberg and Berto are identical to the uniaxial fatigue testing procedure for the heat treated specimens, described in section 6.3, with a load ratio of R=0 and load frequency of 10 Hz. In addition, the tests were also performed using the same fatigue testing machine, namely, the MTS 370.10 50kN Load System. The fatigue data for the as-built specimens, taken from [17], are shown in figure 8.2. The values for the 90%, 50% and 10% confidence bands at 2×10^6 cycles to failure are shown in table 8.2.
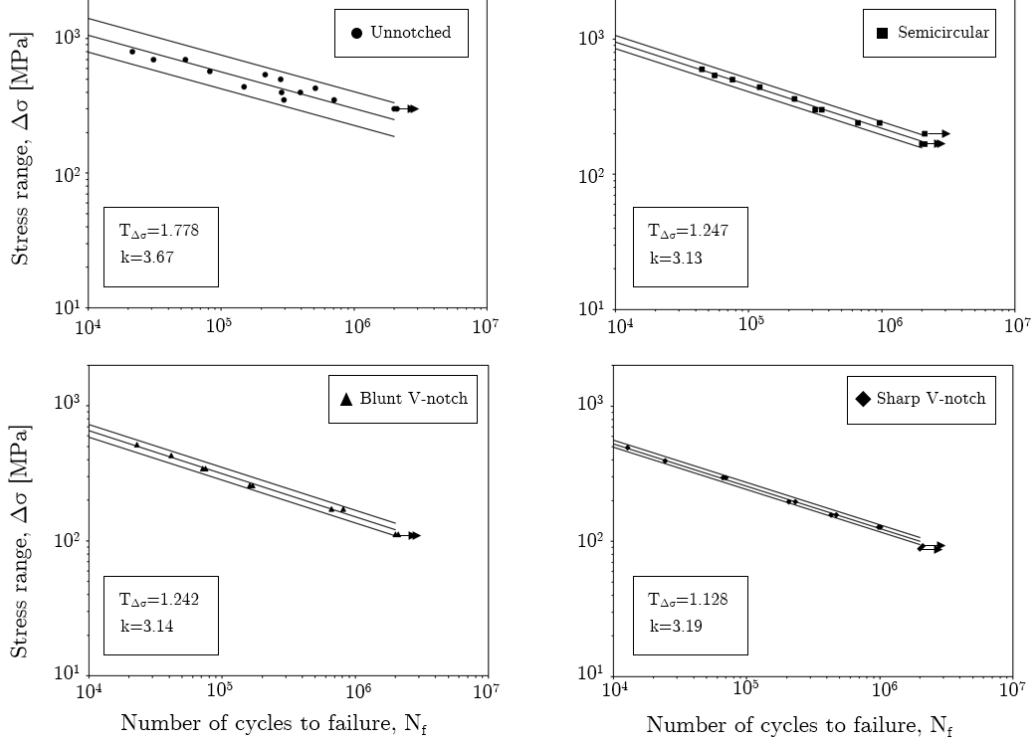
Figure 8.2: Fatigue data, including confidence bands, for unnotched (top left), semicircular (top right), blunt V-notched (bottom left) and sharp V-notched (bottom right) specimens. Data is taken from [17].

Specimen	$\Delta\sigma - 90\%$	$\Delta\sigma - 50\%$	$\Delta\sigma - 10\%$
Unnotched	187.45	250.00	333.32
Semicircular	157.10	175.4	195.84
Blunt V-notched	108.73	121.33	135.02
Sharp V-notched	94.53	100.44	106.60

Table 8.2: Data for confidence bands at 2×10^6 cycles to failure, based on the fatigue data data from [17].

8.1.2 Numerical Setup

In this work, the FE software Abaqus CAE is used to determine the stress fields of the different specimens.

All specimens are modelled according to their geometry and simplified by utilizing the specimen symmetry, allowing for the modelling of only one fourth of the specimen. This reduces the number of elements needed for the simulation and effectively reduces the required computational power. It is important that the boundary conditions and loads are applied in such a way that they satisfactorily represent the geometry of the entire models. A simplified representation of one quarter of a specimen with its boundary conditions and applied load is shown in figure 8.3.

68
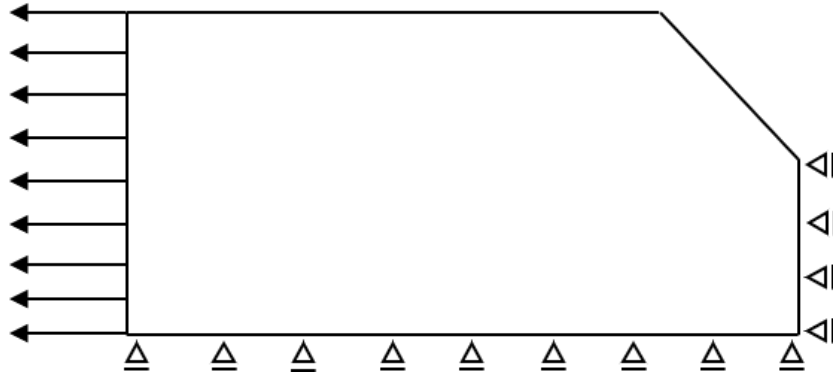
Figure 8.3: Load and boundary conditions for one fourth of the geometry.

A 2D mesh with plane stress thickness 5 mm is used, and the Young's Modulus and Poisson's ratio are set to 200 GPa and 0.3, respectively. The element type is CPS8, which is an 8-node biqadratic plane stress quadrilateral. For the notched specimens, and the sharp-notched in particular, the mesh in the notched region has to be dense in order to accurately calculate the stresses. The meshing strategy for the sharp V-notched specimen, illustrating the partitioning of the surface, is shown in figure 8.4, and the mesh is shown in figure 8.5.
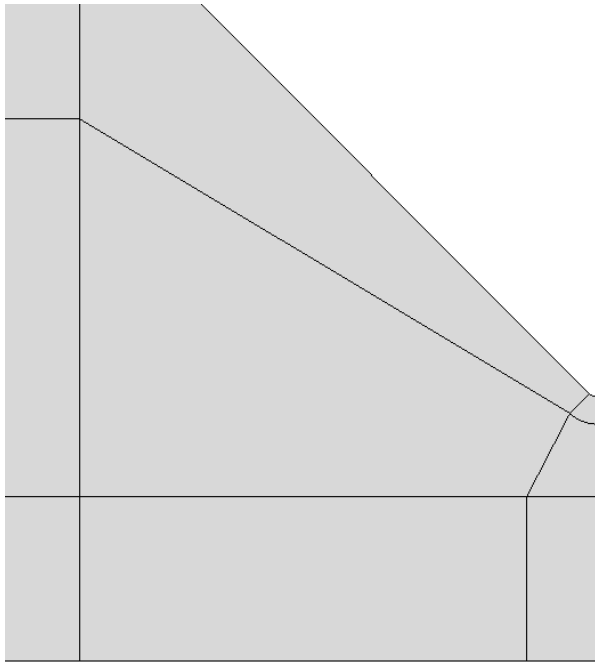
Figure 8.4: Partition of surface near the notch tip of the sharp V-notched specimen.
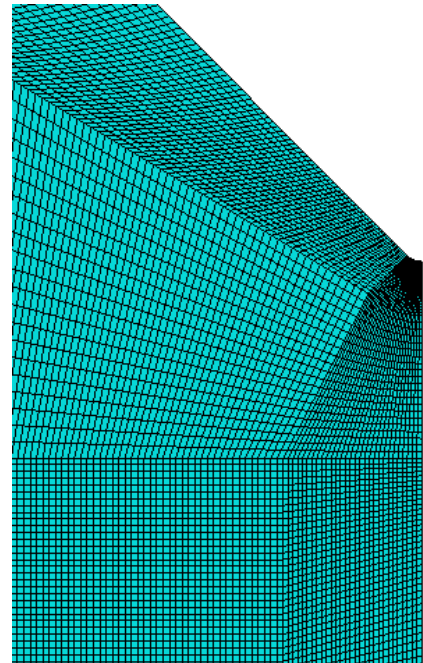
Figure 8.5: Mesh near the notch tip of the sharp V-notched specimen.

In order to determine the stress fields of the different specimens, a path is created along the cross section of the notched region. Recalling the definition of the PM and LM, it is important that the path starts at the notch tip and advances in the radial direction, along the notch bisector line. By subjecting all specimens to a unit load, the stress field along their respective path is obtained. The stress field plots of the different specimens

69

are presented in figure 8.6. The stress is given as the maximum principal stress, which is equal to the stress perpendicular to the notch bisector line, in y-direction (length direction of the specimens). The k_t-values, defined as maximum stress at the notch tip divided by the nominal stress, are also included.
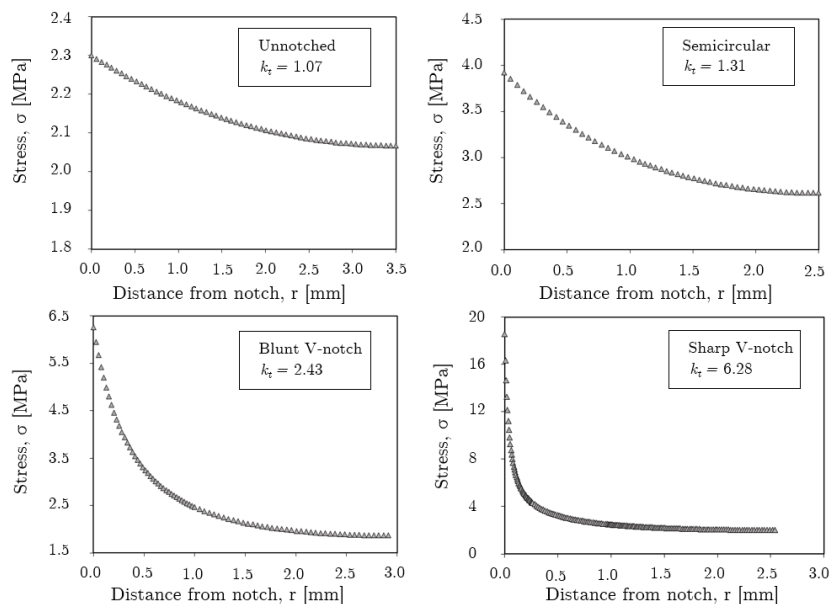
Figure 8.6: Stress fields of the unnotched (top left), semicircular (top right), blunt V-notched (bottom left) and sharp V-notched (bottom right) specimens.

8.2 Determining the Critical Distance

In this section, the critical distance of the as-built AMed specimens will be determined based on both the PM and LM.

8.2.1 The Point Method

In order to determine the critical distance of the as-built AMed Inconel 718 from Solberg and Berto [17], the PM is applied using data from the unnotched and sharp V-notched specimens. As previously mentioned, this procedure requires information about the stress fields and fatigue strength of the specimens. Applying a unit load, the stress fields were plotted in section 8.1.2, referring to figure 8.6. The fatigue data needed for the procedure is taken from the physical tests presented in figure 8.2 in section 8.1.1. The sharp V-notched specimens are used because they have the highest k_t value, similar to what was done by Louks and Susmel [29].

Using the 50% confidence bands of the physical tests, the nominal stress range values at different number of cycles are obtained. These values represent the nominal stress range which give a 50% chance of survival at a given number of cycles. Combining the stress fields at the unit load with the nominal stress range values, stress fields at different number of cycles to failure can be created. This is done by finding the corresponding applied stress on the gross cross-section for each nominal stress range value, and then

multiplying the applied stress value with the stress field at unit load. This is possible because these stress fields were obtained by applying a unit load on the gross cross-section, and the material behavior is assumed to be linear elastic.

Figure 8.7 shows parts of the stress fields of the unnotched and sharp V-notched specimens at 10^5, 5×10^5, 10^6 and 2×10^6 cycles to failure. The intersection between the stress fields of the unnotched and sharp V-notched specimens, at the same number of cycles to failure, gives the $L/2$ value and the effective stress range $\Delta\sigma_{eff}$ at that particular cycle count. The effective stress range, $\Delta\sigma_{eff}$, is obviously equal to the critical stress range $\Delta\sigma_0$ because the intersection point represents a failure condition.
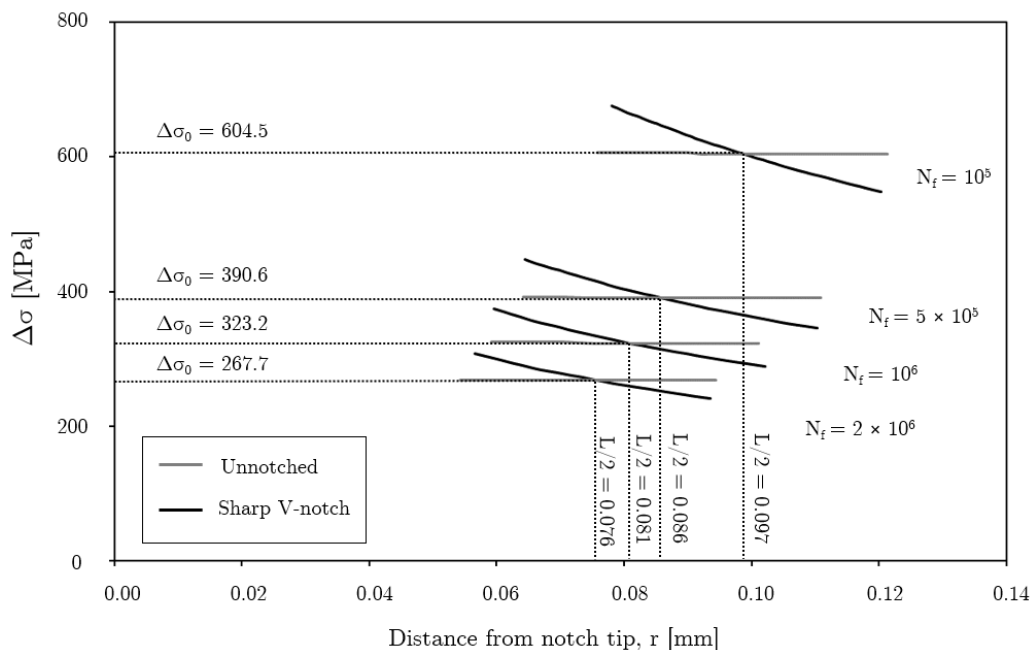
Figure 8.7: Sections of the stress fields of the unnotched and sharp V-notched specimens at 10^5, 5×10^5, 10^6 and 2×10^6 cycles to failure. Effective stress range and L/2 values indicated for each number of cycles to failure.

From the stress fields in figure 8.7, it can be observed that the half of the critical distance, $L/2$, decreases slightly with increasing number of cycles to failure. The critical distance values at different number of cycles to failure are reported in table 8.3. The average values are also reported, and show that the average $L/2$- and L-values between 10^5 and 2×10^6 cycles to failure are equal to $0.085\ mm$ and $0.17\ mm$, respectively. The critical distance at the fatigue limit, which is set to 2×10^6 cycles to failure, is equal to $0.152\ mm$. The relationship between the critical distance and number of cycles to failure is plotted in figure 8.8.

Number of cycles to failure, N_f	$L/2$ [mm]	L [mm]	$\Delta\sigma_0$ [MPa]
10^5	0.097	0.194	604.5
5×10^5	0.086	0.172	390.6
10^6	0.081	0.162	323.2
2×10^6	0.076	0.152	267.7
Average	0.085	0.170	

Table 8.3: Critical distance values versus number of cycles to failure calculated according to the PM. Critical stress ranges are also included.
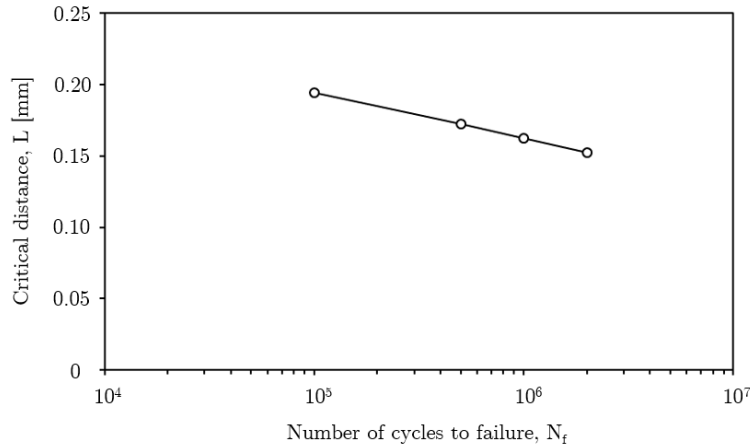
Figure 8.8: Critical distance determined by the PM, versus number of cycles to failure.

8.2.2 The Line Method

The determination of the critical distance based on the LM is performed based on the same stress fields as for the PM, i.e. the stress fields at 10^5, 5×10^5, 10^6 and 2×10^6 cycles to failure for the 50% confidence bands for the unnotched and sharp V-notched specimens, plotted in figure 8.7. As was presented in section 3.6.2, the LM is based on averaging the stress field over a distance of two times the critical distance, $2L$. This is done by integrating the stress field and dividing the integral by $2L$, which gives the effective stress range, $\Delta\sigma_{eff}$, referring to equation 3.13. The principle of the L-determination for the LM is similar to that of the PM in the previous section; the critical distance is determined by finding the distance that gives the same effective stress range for the two specimens. For the PM, this was determined by the intersection between the two stress fields, while the LM uses the average stress over a distance. The procedure for determining the critical distance based on the LM is illustrated in figure 8.9.
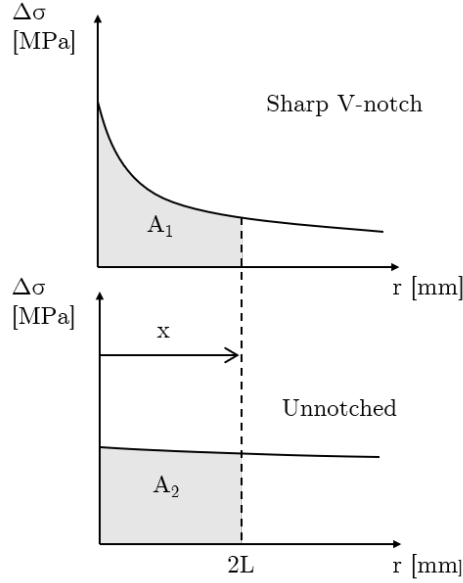
Figure 8.9: Procedure for determining the critical distance based on the sharp V-notched and unnotched specimens, using the LM approach.

In order to determine the critical distance, the stress fields of the two specimens are integrated separately with the same integration limits, using the trapezoidal rule. The lower limit of the integration starts at the notch root and is equal to zero, while the upper limit is located at a point along the notch bisector line. For each number of cycles to failure, the stress fields are integrated, and the upper limit of the integration is changed until the two integrals are equal. Referring to figure 8.9, this is the same as changing the x-value until A_1 equals A_2. This procedure effectively determines the distance along the notch bisector line which gives an equal effective stress range for the unnotched and sharp V-notched specimen. Recalling the definition of the LM from section 3.6.2 and equation 3.13, this distance is defined as $2L$, which is the material's critical distance multiplied by a factor 2. The effective stress range is found by dividing the integral by $2L$. Similar to the PM, the effective stress ranges found for each number of cycles to failure are considered as the critical stress ranges, $\Delta\sigma_0$.

The resulting critical distance values obtained through the LM are shown in table 8.4, and the trend is plotted in figure 8.10. It can be seen that the critical distance decreases with increasing number of cycles to failure, similar to what was observed for the PM. The critical stress range values reported in table 8.4 are almost identical to the values found for the PM.

Number of cycles to failure, N_f	L [mm]	$2L$ [mm]	$\Delta\sigma_0$ [MPa]
10^5	0.150	0.300	601.4
5×10^5	0.125	0.250	390.0
10^6	0.115	0.230	324.2
2×10^6	0.110	0.220	266.7
Average	0.125	0.250	

Table 8.4: Critical distance values versus number of cycles to failure calculated according to the LM. Critical stress ranges are also included.
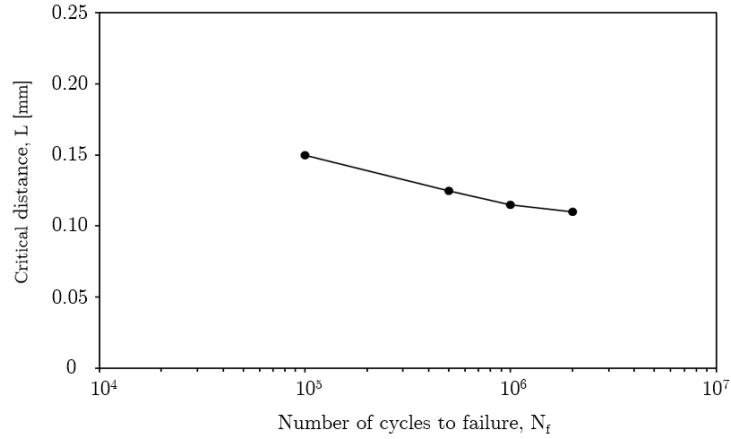
Figure 8.10: Critical distance determined by the LM, versus number of cycles to failure.

8.2.3 Comparison of L-values determined by the Point and Line Method

The critical distances determined by the PM and LM approaches are not the same. Table 8.5 summarizes the critical distance values obtained through the two methods, and it can be seen that the critical distance values found by the point method are generally higher than those of the line method. This applies for all number of cycles to failure, and the difference is visualized in figure 8.11, where critical distance is plotted versus number of cycles to failure.

| | Critical distance, L [mm] | |
Number of cycles to failure, N_f	PM	LM
10^5	0.194	0.150
5×10^5	0.172	0.125
10^6	0.162	0.115
2×10^6	0.152	0.110
Average	0.170	0.125

Table 8.5: Summary of the critical distance values obtained according to the PM and LM.

74
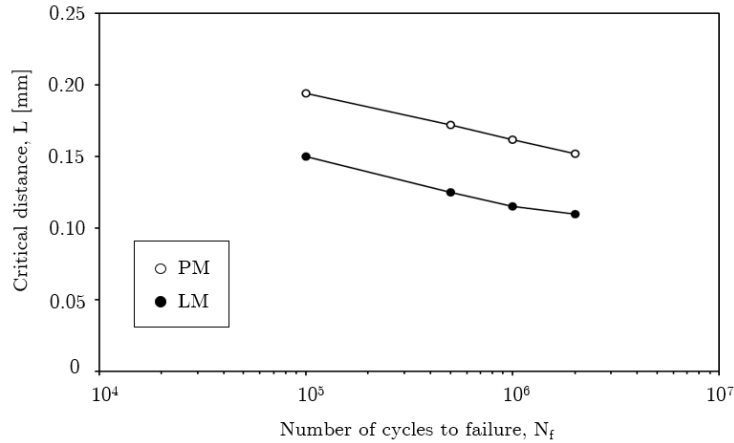
Figure 8.11: Critical distance values determined according to the PM and LM, versus number of cycles to failure.

8.3 Fatigue Limit Prediction

Having obtained the critical distance values for the as-built Inconel 718 specimens by means of both the PM and LM, these values can be used to predict the fatigue limit of the as-built blunt V-notched and semicircular specimens. This is done by considering the stress fields of the blunt V-notched and semicircular specimens at the fatigue limit given by the 50% confidence bands, and using the critical distance values at the fatigue limit to modify the stress fields. As previously mentioned, the fatigue limit is set to 2×10^6 cycles to failure. In section 8.1.1, the stress range at 2×10^6 cycles to failure for the 50% confidence bands were reported. Specifically, these values were reported in table 8.2.

Point Method
In section 8.2.1, the critical distance at the fatigue limit was found to be 0.152 mm, which corresponds to $L/2 = 0.076mm$. This value, combined with its corresponding critical stress range, $\Delta\sigma_0 = 267.7MPa$, can be used to modify the stress fields of the blunt V-notched and semicircular specimens. This procedure is illustrated in figure 8.12. The basis of the procedure is the postulation of the PM, which states that the stress fields of all specimens should intersect in the same point, namely the point at a distance $L/2$, which means that the effective stress range is equal for all specimens in that particular point. In reality, the effective stress ranges are however not the same at $L/2 = 0.076mm$, referring to figure 8.13 which shows the stress fields of all specimens at the fatigue limit. The figure includes the $L/2$ value found in section 8.2.1, based on the unnotched and sharp V-notched specimens at 2×10^6 cycles to failure.
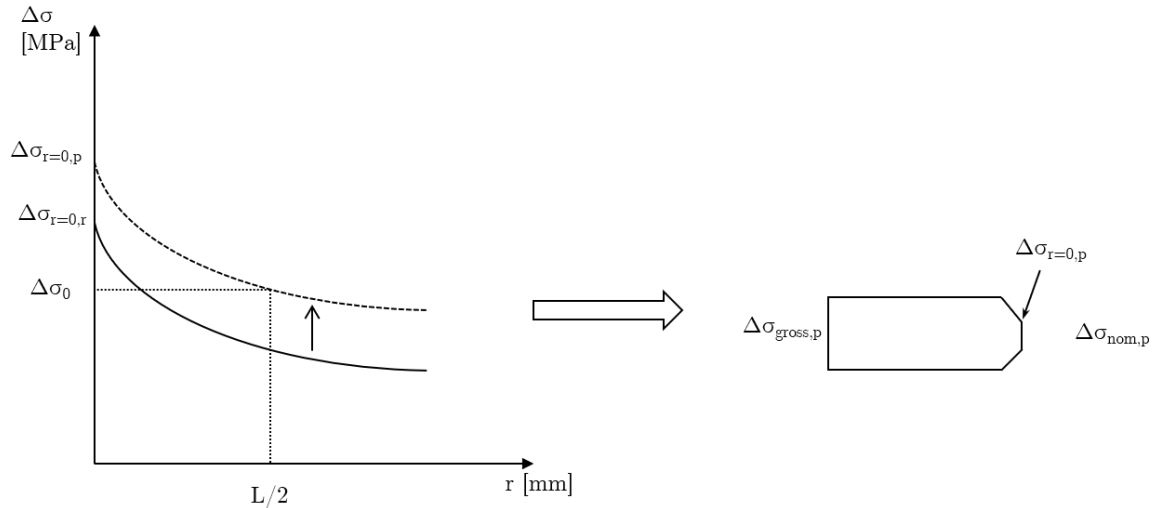
Figure 8.12: Procedure for predicting the fatigue limit of the blunt V-notched and semicircular specimens. $\Delta\sigma_{r=0,r}$ is the real maximum stress at the notch root at 2×10^6 cycles to failure, while $\Delta\sigma_{r=0,p}$ is the predicted maximum stress found by shifting the stress fields in y-direction.

First, the stress fields of the blunt V-notched and semicircular specimens are moved in y-direction, so that their stress fields intersect with the point given by $L/2 = 0.076$ and its corresponding critical stress range, equal to 267.7 MPa. This will effectively give a new intersection point between the individual stress fields and the y-axis. The new intersection with the y-axis represents the predicted maximum stress at the notch-tip, from here referred to as $\Delta\sigma_{r=0,p}$, and can be used to reverse calculate its corresponding predicted nominal stress range, $\Delta\sigma_{nom,p}$. This nominal stress range is then considered the predicted fatigue limit of the specimens, and can be compared with the experimentally obtained fatigue limit.
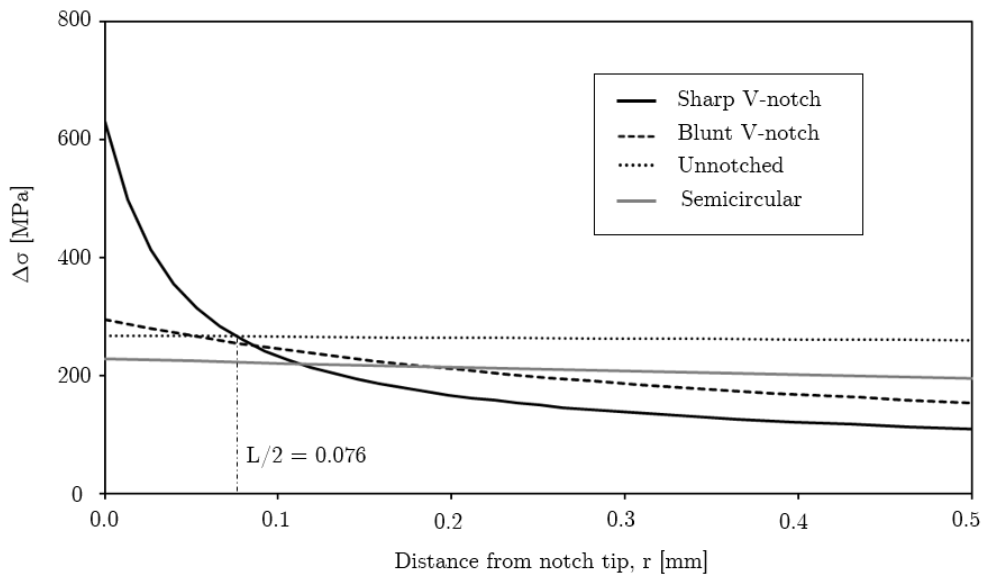
Figure 8.13: Stress fields of all specimens at 2×10^6 cycles to failure from the 50% confidence bands.

76

Table 8.6 shows the results of the prediction procedure for both specimens and indicates the error of the prediction, given by equation 8.1. From the results it can be seen that the estimated value for the semicircular specimen is less accurate than the estimated value for the blunt V-notched specimen, and that the PM slightly overestimates the fatigue limits.

$$Error = \frac{Predicted - Experimental}{Experimental}[\%] \tag{8.1}$$

| | Fatigue limit, $\Delta\sigma$ [MPa] | | |
Specimen	Experimental	Predicted	Error [%]
Blunt V-notched	121.3	126.3	4.1
Semicircular	175.4	208.6	18.9

Table 8.6: Predicted fatigue limit of blunt V-notched and semicircular specimens at 2×10^6 cycles to failure, according to the PM.

Line Method

The same principles of the prediction procedure based on the PM, also applies for the LM. Instead of considering the intersection point, the LM postulates that the effective stress range for the specimens are equal when the stress fields are averaged over a distance $2L$. In section 8.2.2, the critical distance and the corresponding critical stress range was calculated according with the LM. At the fatigue limit, 2×10^6 cycles to failure, the critical distance was found to be 0.11 mm, giving a $2L$ value of 0.22 mm. Its corresponding critical stress range was equal to 266.7 MPa. In order to predict the fatigue limit of the blunt V-notched and semicircular specimens, their stress fields are integrated between constant integration limits of zero and $2L = 0.22mm$. Following the same procedure as that of the PM fatigue limit prediction, the stress fields are moved in the y-direction until the effective stress range equals the critical stress range corresponding to the critical distance of $L = 0.11mm$. The procedure for moving the stress fields in y-direction with fixed limits, zero and $2L = 0.22mm$, is illustrated in figure 8.14.
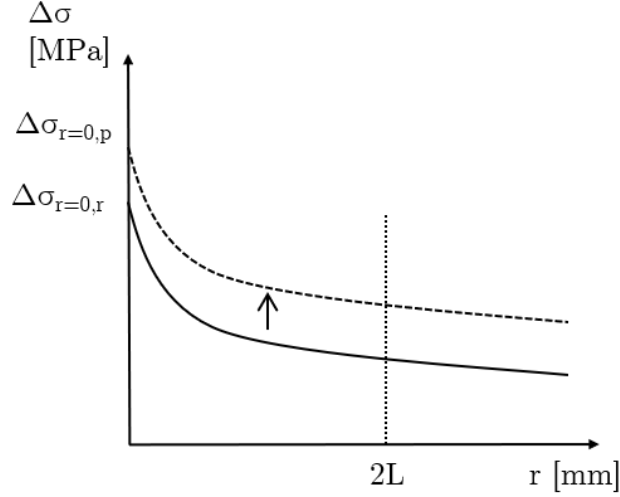
Figure 8.14: Procedure for shifting the stress fields in y-direction with fixed limits. $\Delta\sigma_{r=0,r}$ is the real maximum stress at the notch root at 2×10^6 cycles to failure, while $\Delta\sigma_{r=0,p}$ is the predicted maximum stress.

Having moved the stress fields the correct amount in y-direction, the new intersections with the y-axis are used to reverse calculate the corresponding nominal stress range, identical to what was done for the PM. This stress range is the predicted fatigue limit and can be compared with the actual fatigue limit. The results are given in table 8.7, and shows that the semicircular specimens are more difficult to predict, similar to what was seen for the PM.

Specimen	Fatigue limit, $\Delta\sigma$ [MPa]		Error [%]
	Experimental	Predicted	
Blunt V-notched	121.3	131.3	8.2
Semicircular	175.4	210.2	19.8

Table 8.7: Predicted fatigue limit of blunt V-notched and semicircular specimens at 2×10^6 cycles to failure, according to the LM.

Table 8.8 summarizes the predicted values for both the PM and LM, and reveals that the predictions based on the LM is slightly less accurate than those of the PM. Both the PM and LM overestimates the fatigue limit of the specimens, however, the overall accuracy is promising, with an absolute error below 20 %. The accuracy of the two approaches is also illustrated in figure 8.15.

Specimen	Experimental	PM		LM	
		Predicted [MPa]	Error [%]	Predicted [MPa]	Error [%]
Blunt V-notched	121.3	126.3	4.1	131.3	8.2
Semicircular	175.4	208.6	18.9	210.2	19.8

Table 8.8: Predicted fatigue limits of blunt V-notched and semicircular specimens at 2×10^6 cycles to failure, according to the PM and LM.
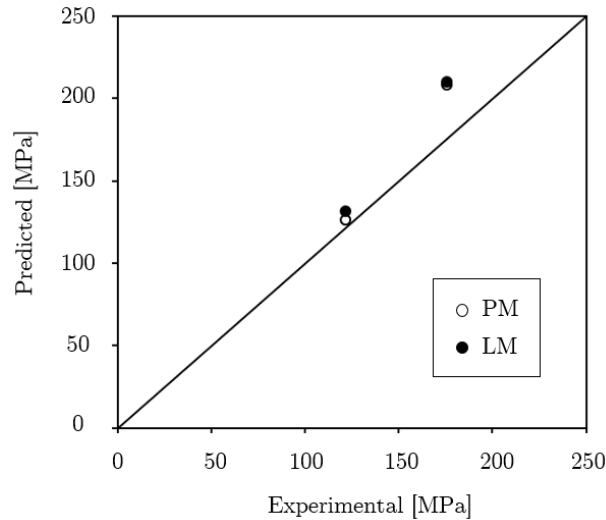
Figure 8.15: Experimentally obtained versus predicted fatigue limits, for PM and LM.

8.4 Modification of the Fatigue Data Based on the Point Method

The SN-curves that was presented in section 8.1.1 represents the number of cycles to failure versus the stress range in the net section of the specimens. Using the stress range or stress amplitude in the net section is the common way of representing the fatigue properties of a material or component. However, with the basis of the critical distance obtained according to the PM, the fatigue data can be modified to represent another stress situation.

Recalling that the PM postulates that the critical stress range for all specimens of the same material is equal at $L/2$, the fatigue data for the different specimens can be re-designed to represent the stress range at $L/2$ instead of the nominal stress range. Figure 8.16 shows the modified fatigue data for the blunt and sharp V-notched, and the semi-circular specimens, including their 10%, 50% and 90% confidence bands. These plots are created by considering the average $L/2$-value found in section 8.2.1, which is equal to 0.085 mm, because this value better represents the critical distance values for the entire span in number of cycles to failure. With the basis of $L/2 = 0.085$, the fatigue data for all specimens are modified in such a way that they represent the stress range at a distance 0.085 from the notch tip, instead of the nominal stress range. This modification is done for each specimen separately, considering the stress fields of the individual specimens. The scatter parameters and inverse slopes of the curves in figure 8.16 are obviously equal to the ones reported in figure 8.2 in section 8.1.1, because the data points for each specimen have been "shifted" by the same amount.
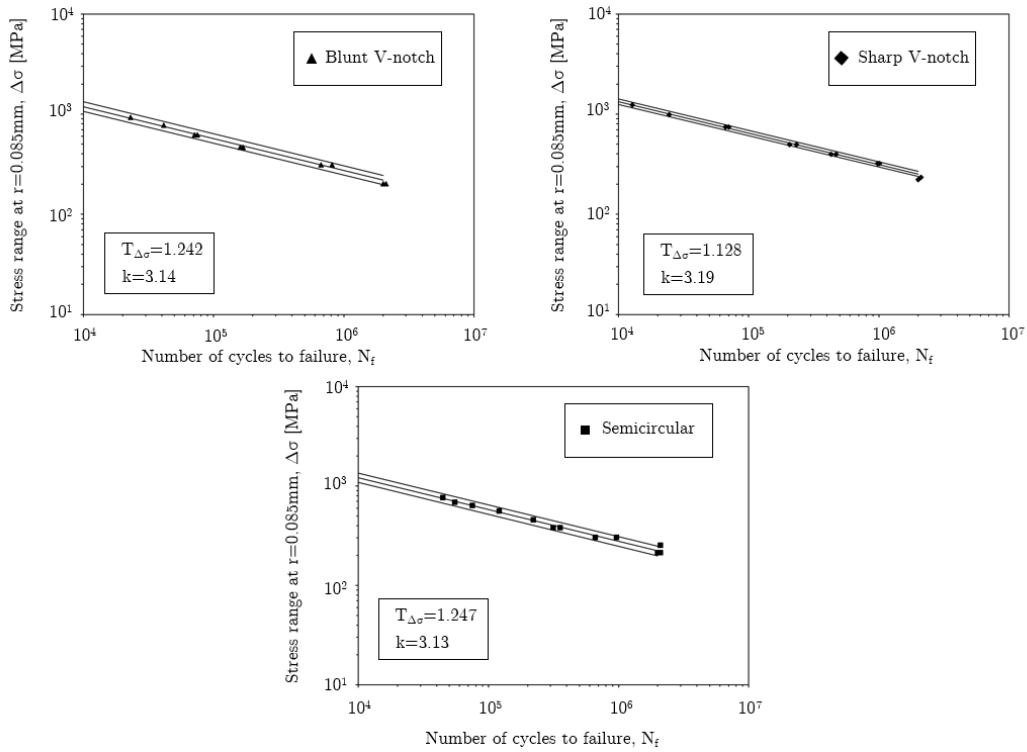
Figure 8.16: Fatigue data of the blunt V-notched (top left), sharp V-notched (top right) and semicircular (bottom) specimens, presented as stress range at r=0.085 mm versus number of cycles to failure.

In figure 8.17, the modified fatigue data for all three specimens are included in the same diagram. The 10%, 50% and 90% confidence bands are also included, and they are created based on the combined data of all specimens. The resulting plot shows that the modified fatigue data for the three specimens give relatively low scatter, with a scatter parameter of $T_{\Delta\sigma} = 1.289$. This means that the modification of the fatigue data, based on $L/2 = 0.085$, is able to "gather" the fatigue data in such a way that they come together approximately along one line and with little scatter.
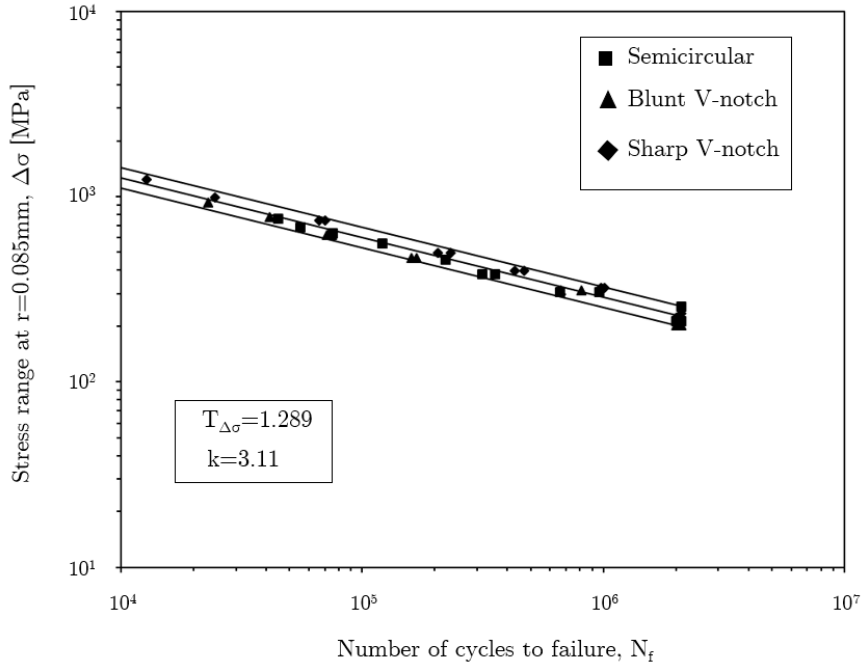
Figure 8.17: Combined fatigue data of the semicircular, sharp and blunt V-notched specimens, presented as stress range at r=0.085 mm versus number of cycles to failure.

8.5 Effect of Heat Treatment

In this section, the heat treated specimens from section 6.1 are introduced and investigated by means of the PM and the LM. For a valid comparison between heat treated and as-built specimens, the critical distance must be determined based on the same specimen geometries. This means that the blunt V-notched specimens will be used, since these specimens are the only heat treated notched specimens included in this work.

Point Method
Following the same procedure as the one in section 8.2.1, the critical distance of the heat treated and as-built specimens are determined based on the blunt V-notched and unnotched specimens. For this purpose, the stress fields of the specimens are plotted for 10^5, 5×10^5, 10^6 and 2×10^6 cycles to failure, both for the heat treated and as-built specimens, using the 50% confidence bands. The confidence bands for the heat treated specimens are taken from section 7.2, while the confidence bands for the as-built specimens are taken from section 8.1.1. The stress field plots of the heat treated and as-built specimens are shown figure 8.18.

81
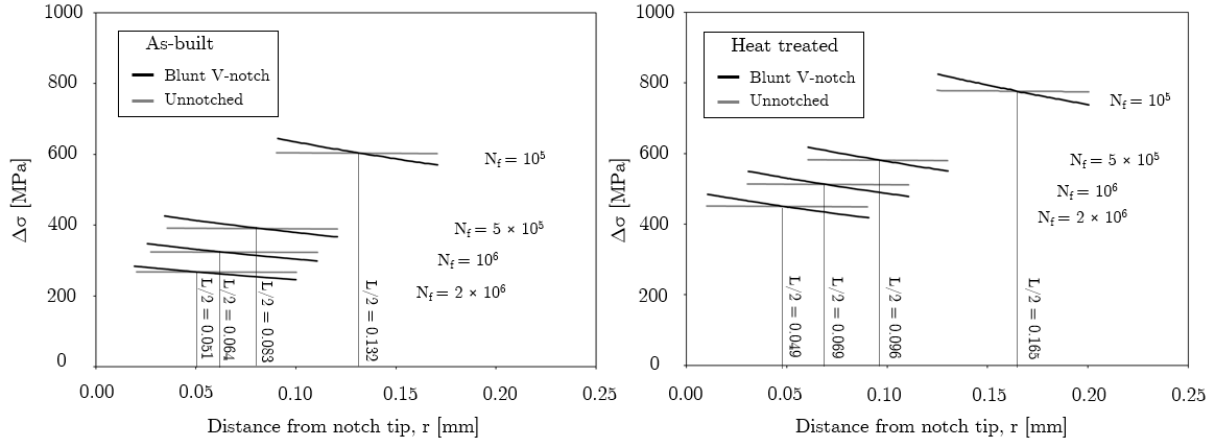
Figure 8.18: Sections of the stress fields of as-built (left) and heat treated (right) blunt V-notched and unnotched specimens at 10^5, 5×10^5, 10^6 and 2×10^6 cycles to failure. The $L/2$ values are indicated for each intersection point.

The intersections of the stress fields give the $L/2$ value at that particular number of cycles to failure. These values are reported in table 8.9, together with the L values, and the critical distance versus number of cycles to failure is plotted in figure 8.19. These curves reveal that the difference in critical distance between heat treated and as-built specimens is larger for lower number of cycles to failure, with the heat treated specimens having higher critical distance than the as-built specimens. As the number of cycles to failure increases, the critical distance values for heat treated and as-built specimens seems to converge against a common value.

	As-built		Heat Treated	
Number of cycles to failure , N_f	$L/2$ [mm]	L [mm]	$L/2$ [mm]	L [mm]
10^5	0.132	0.264	0.165	0.330
5×10^5	0.083	0.166	0.096	0.192
10^6	0.064	0.128	0.069	0.138
2×10^6	0.051	0.102	0.049	0.098

Table 8.9: Critical distances for the as-built and heat treated specimens at different number of cycles to failure, determined by the PM.
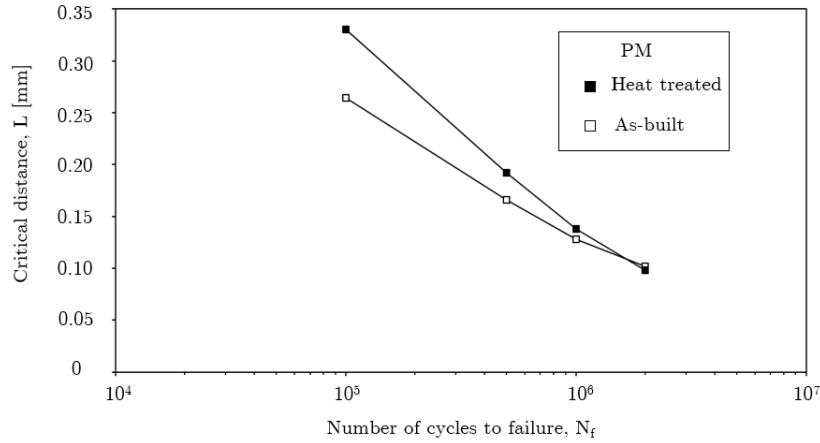
Figure 8.19: Critical distance of heat treated and as-built specimens versus number of cycles to failure, determined by the PM.

Line Method

Using the stress fields introduced in figure 8.18, and following the same procedure as in section 8.2.2, the critical distance of the heat treated and as-built specimens are determined based on the LM. The resulting critical distance values are reported in table 8.10, and the critical distance versus number of cycles to failure is plotted in figure 8.20. The same trend is seen here as it was for the PM; the critical distance values for the heat treated specimens are higher than those of the as-built specimens for lower number of cycles to failure, and the values seems to converge against a common value for higher number of cycles to failure. It can also be observed that the LM yields lower critical distance values than the PM, similar to what was seen in section 8.2.3.

	As-built		Heat Treated	
Number of cycles to failure , N_f	L [mm]	$2L$ [mm]	L [mm]	$2L$ [mm]
10^5	0.145	0.29	0.185	0.370
5×10^5	0.088	0.175	0.100	0.200
10^6	0.063	0.125	0.068	0.135
2×10^6	0.050	0.100	0.050	0.100

Table 8.10: Critical distances for the as-built and heat treated specimens at different number of cycles to failure, determined by the LM.
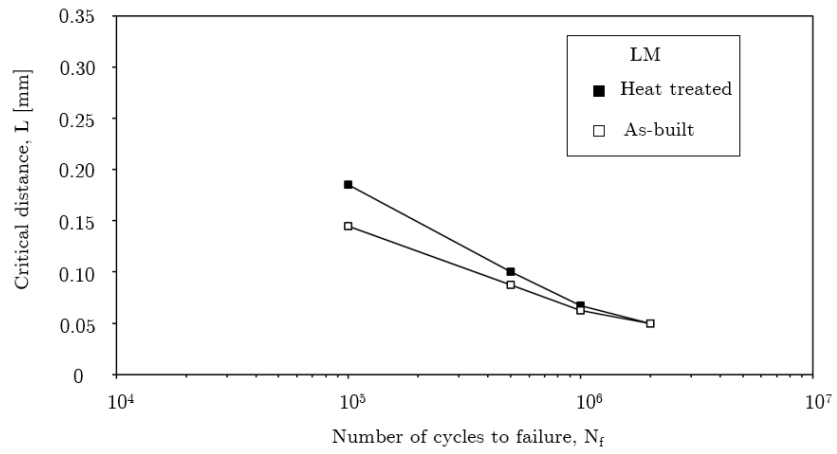
Figure 8.20: Critical distance of heat treated and as-built specimens versus number of cycles to failure, determined by the LM.

9 Engineering Approach to the TCD

Having seen that the TCD yields good prediction results in section 3.6.3 and 8.3, and the possibility of modifying the fatigue data for assessing fatigue performance based on the PM, this section introduces a proposed method for applying the TCD in engineering tasks.

9.1 Using FEA and CAD Software

Since the TCD relies on the stress situation at a distance from the surface of a component, it is desirable to have information about this stress in order to apply the TCD criterion in engineering tasks. When performing stress-analyses in Abaqus, the output results are given as stresses on the surface of the model. It is also possible to create node-paths to obtain the stress fields at different locations of interest, as was done in section 8.1.2. These stress fields can easily be used to make failure predictions based on the TCD, but they have to be created individually and at specific locations of the engineering component. If the component in question contains several stress raisers and it is difficult to predict where the highest critical distance stress is located, the node path approach requires that node paths are created at each stress raiser. In addition, it can be a time consuming and challenging task to create node paths that follows the most critical direction of the stress distribution for each stress raising feature. In this section, an alternative approach to obtain information about the stress at a distance from the surface is proposed. The approach includes modelling a component in a CAD software, before analysis is performed in an FE software. The steps of the entire procedure are summarized in Appendix A, where a simple notched cylinder with an arbitrary geometry is used as an example. Appendix A also includes a short verification of the procedure, where an arbitrary load is applied and the node path approach is carried out for comparison purposes.

The Offset Procedure
The procedure for setting up a simulation that allows for a convenient investigation of the stresses at a distance from the model surface, starts with creating the model in a CAD software. In this work, Inventor is used for modelling, while Abaqus is used for the FE simulations. In the explanation that follows, the notched cylinder from appendix A will be used for visualization purposes.

First, the original part is created and saved. Then, a modified solid part is created by offsetting the surfaces of the original model. In inventor, this is done by using the Thicken/Offset command and specifying the offset direction in such a way that the new surface is located on the inside of the original part. Performing a cut will effectively remove the volume located between the outer surface of the original part and the offset surface, and a new part is created. The surface of this offset part now represents the material located at a specified distance from the surface of the original part, specified by the offset distance, and can be saved as an individual part.

Having created two individual parts – the original part and the offset part – the parts can be imported and assembled in Abaqus. In Abaqus, the parts are first assigned sections individually and then assembled in order to create a combined part. It is important that a new set is created for each part when assigning sections. Since the parts were created based on the same coordinate system in Inventor, they will automatically be placed on top of each other when assembled in Abaqus. This means that the offset part will be located inside the original part with its surface positioned at a constant distance from the surface of the original part. In the assembly-module, the parts must be merged, and the intersecting boundaries must be retained. This step effectively creates a new part, identical to the original part, but with a partitioning surface located at an offset distance from its outer surface, as shown in figure 9.1. The offset-distance is determined by the distance specified when creating the offset part in Inventor.
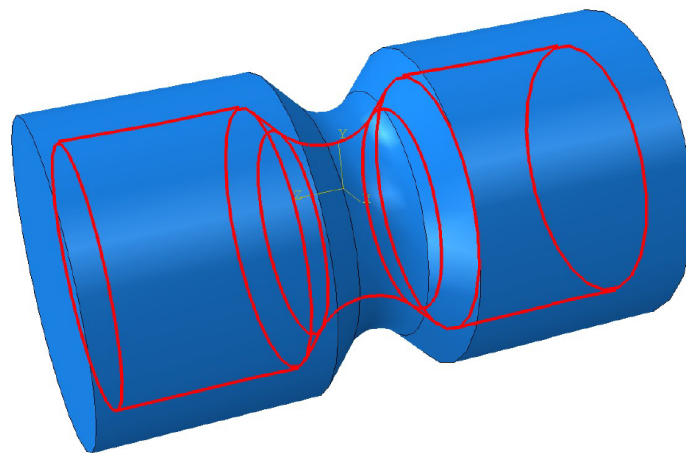
Figure 9.1: Partition surface inside the original part.

After creating the assembled part with an offset partition-surface, the part can be meshed and analyzed. When the part is meshed, two element sets are created; one element set will be located outside the partition surface, while the other element set is located inside the partition surface. Figure 9.2 shows how the original part consists of one external and one internal element set. The two element sets are divided by the partition surface, and share this surface as a common face. The elements will always align with the partition, or offset, surface.
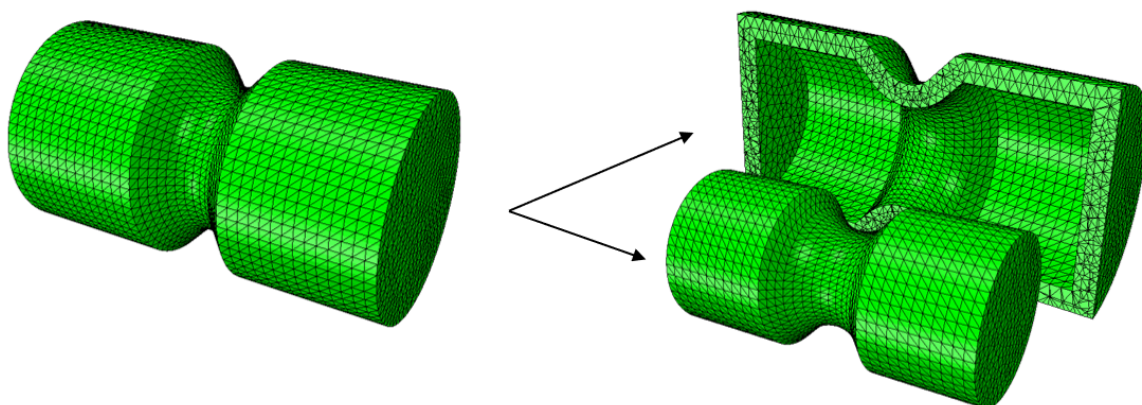
Figure 9.2: Internal and external element set of the part.

After running the analysis, the resulting stresses can be studied in the viewport of the visualization module in Abaqus. These stresses are by default displayed on the surface of the model. However, having performed the offset procedure described above, the stresses at an offset distance from the surface can be obtained. These stresses are visualized by removing the element set located outside the partition surface, leaving only the internal element set visual. The surface stresses on the internal element set represents the stresses at an offset distance from the surface of the original part. Figure 9.3 shows the stresses on both the original part surface and at an offset distance. As expected, the stresses are lower at a distance from the surface.
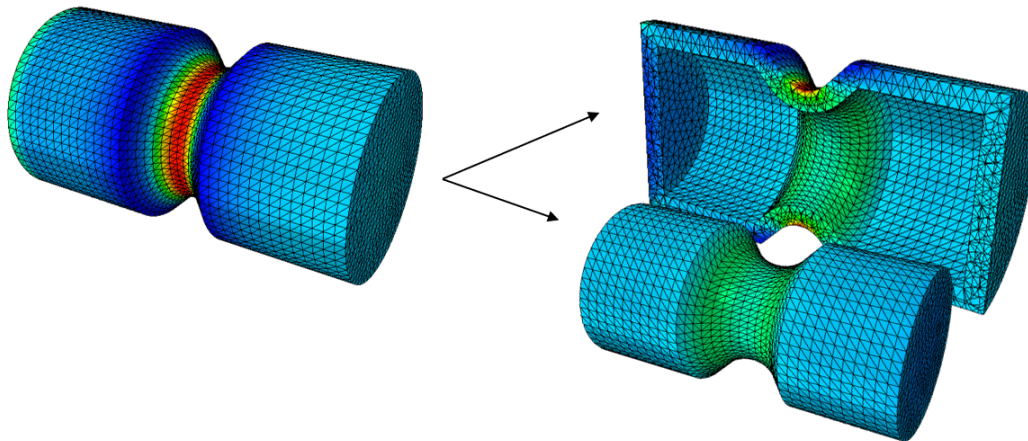
Figure 9.3: Stresses on the internal and external element set of the part.

In section 10.5.1, some possible applications of the offset procedure will be presented and discussed. These applications include fatigue assessment based on the PM, identification of the critical region of a component based on the PM and shape optimization.

10   Discussion

10.1   Critical Distance of As-Built Inconel 718

In section 8.2, the critical distance of as-built Inconel 718 was determined based on both the PM and LM for different number of cycles to failure. This was done using the sharp V-notched specimens and the unnotched specimens, similar to what was done by Louks and Susmel [29] who used the specimen with highest k_t together with the unnotched specimen. However, Louks and Susmel did not use the stress fields of the unnotched specimen, but rather the nominal stress range when determining the critical distance, similar to what was done by Taylor et al. [31]. In this work, the stress fields of the unnotched specimens are used instead of the nominal stress range, meaning that the critical stress range, $\Delta\sigma_0$, is never exactly equal to the nominal stress range of the unnotched specimens at a given number of cycles to failure. This is done to perform the PM and LM calculations based on more realistic stress conditions, and effectively obtain more accurate results.

Difference Between PM and LM
In section 8.2.1 and 8.2.2, the critical stress range values obtained according to the PM and LM were reported. These values are almost identical for all number of cycles to failure, indicating that the PM and LM procedures were carried out correctly. The small difference is most likely related to the integration based on the trapezoidal rule for the LM.

Even though the critical stress ranges are the same, the critical distance values calculated by the two methods are different. From the results in figure 8.11, it can be seen that the critical distance values obtained through the PM are higher than the values obtained through the LM, for all number of cycles to failure. This is in line with what was observed by Benedetti and Santus [32] when using the inverse search procedure for determining the critical distance of AMed Ti-6Al-4V ELI.

The Critical Distance Values
Louks and Susmel [29] calculated the critical distance of Inconel 718 based on fatigue data from Chen et al. [35], as was mentioned in section 3.6.3. The specimens were fatigue tested at 500 °C, with a load ratio of R = -1. At the fatigue limit condition of the material, the critical distance was determined according to the PM based on specimens with $k_t = 8$. A critical distance of $L = 0.154mm$ was obtained, which is very similar to the critical distance obtained in this work when using the PM at the fatigue limit ($L = 0.152mm$). This is an interesting observation, considering that the fatigue tests performed in this work were carried out at room temperature and with a load ratio of R = 0. In addition, the specimens tested by Chen et al. were not produced by means of additive manufacturing and had a significantly higher fatigue limit.

It is difficult to say why these values are almost identical, considering the difference in test parameters and production method, as well as physical properties of the specimens. In order to make comparisons of the critical distance of Inconel 718, and investigate the

effect of test parameters and production method, more fatigue test data of Inconel 718 should be studied by means of the TCD. There are not many critical distance values of Inconel 718 reported in literature.

Critical Distance Dependency on Number of Cycles to Failure
From the results in figure 8.11, it is evident that the number of cycles to failure has an impact on the critical distance. With increasing number of cycles to failure, the critical distance value decreases. This applies for both the PM and LM. The same phenomenon was observed by Benedetti and Santus [32], where they used the inverse search procedure and found that the L is a decreasing function of N_f.

The change in L with respect to N_f is related to the inverse slope of the confidence bands of the as-built unnotched and sharp V-notched specimens. The inverse slopes, k, were reported in figure 8.2, and revealed that the slope of the sharp V-notched specimens' confidence bands were steeper than those of the unnotched. This difference in slopes has an effect on the critical distance determination that can be conveniently explained by means of the PM, but the same effect of course also applies for the LM.

When the nominal stress ranges are extracted from the 50% confidence bands and used to plot the stress fields at 10^5, 5×10^5, 10^6 and 2×10^6 cycles to failure, as was done in figure 8.7, the intersection of the stress fields depend on the slope of the confidence bands. If the confidence bands were parallel, meaning that the slopes are equal, the stress fields would intersect at the same distance from the notch root for all N_f. Since the confidence bands of the sharp V-notched specimens have a steeper slope than the unnotched, the stress fields will intersect at a shorter distance from the notch root with increasing number of cycles to failure. This will effectively give shorter critical distances with increasing N_f.

10.2   Fatigue Limit Prediction

The Approach
The approach for determining the fatigue limit proposed in this work is slightly different to the approach of Louks and Susmel [29]. When predicting the fatigue limit according to the PM, Louks and Susmel use the $L/2$ value to determine the effective stress range at the fatigue limit, $\Delta\sigma_{eff}$, of the specimen to be assessed. For this purpose, the stress field at the fatigue limit of the specimen to be assessed and the $L/2$ value must be obtained through experiments. The effective stress range value is then compared to the critical stress range, $\Delta\sigma_0$, and the error is calculated using equation 3.17. This prediction is based on the assumption that the stress range at $L/2$ of the specimen to be assessed, should be equal to the critical stress range. Figure 10.1 shows how the approach of Louks and Susmel can be used to predict the fatigue limit of the semicircular specimen, based on the stress fields from section 8.3.
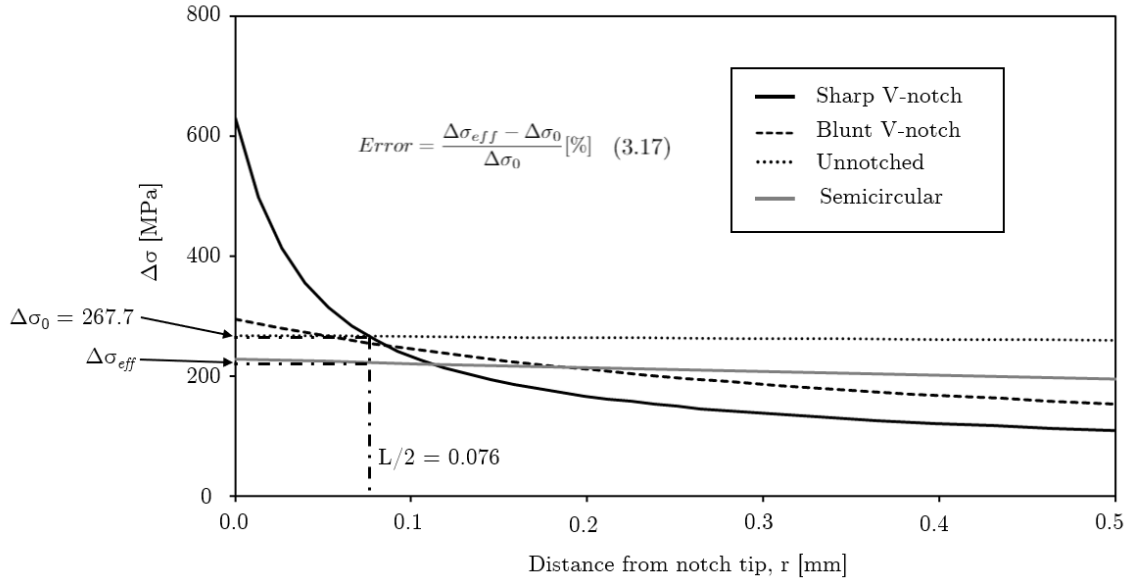
Figure 10.1: Determining the fatigue limit of the semicircular specimens based on the approach of Louks and Susmel [29].

The approach proposed in this work, which was described in section 8.3, is based on shifting the stress field of the specimen to be assessed. The stress field is shifted to the intersection of the critical stress range and $L/2$, as was seen in figure 8.12, and the new intersection with the y-axis is the predicted stress at the notch root. Referring to figure 10.1, this is done by shifting the stress field of the semicircular specimen to the point where $\Delta\sigma_0 = 267.7MPa$ and $L/2 = 0.076mm$ intersects. The predicted stress at the notch root is then used to find the predicted nominal stress range, which is compared to the experimentally obtained nominal stress range by finding the error according to equation 8.1. This approach is also based on the assumption that the effective stress range of the specimen to be assessed, is equal to the critical stress range. However, the procedure does not require information about the stress field at the fatigue limit of the specimen to be assessed. This is because the stress field is shifted to the intersection between $L/2$ and the critical stress range $\Delta\sigma_0$, meaning that the stress field at unit load is the only required information, in addition to the $L/2$ value. In effect, the fatigue limit of all specimens can be predicted as long as their stress fields at unit load are known, and that the $L/2$ and $\Delta\sigma_0$ values are determined from previous experiments. This allows for a more flexible approach than the one used by Louks and Susmel.

It should also be stressed that the absolute errors obtained through the approach from section 8.3 and the approach of Louks and Susmel are identical. This is because the stress fields are shifted by an amount corresponding to the difference between the $\Delta\sigma_0$- and $\Delta\sigma_{eff}$-values that Louks and Susmel use when calculating the error. The two approaches will however give errors of opposite signs.

Accuracy

The results from section 8.3, reveal promising fatigue limit prediction abilities of both the PM and LM. Table 8.8 shows that the absolute error is below 20% for both the PM and LM, and that the PM yields slightly more accurate results than the LM. The superior prediction accuracy of the PM, with respect to the LM, has been reported by several

authors [32, 29, 74].

The accuracy of the results, indicated by the calculated error, is comparable to several results reported in literature. Benedetti and Santus [32] used the inverse search procedure, presented in section 3.6.3, for prediction of the fatigue limit. The error of this prediction had a maximum absolute value of 8%, when L was obtained from tensile fatigue tests, and a maximum absolute error of 15.9% when L was obtained from FCG rate tests. The maximum error of 15.9% is comparable to the least accurate results in this work, presented in section 8.3, while the maximum error of 8% is more accurate. This indicates that the inverse search procedure based on L-values obtained from tensile fatigue tests, can be considered as slightly more accurate than the procedure proposed in this work, even though the difference is rather small.

As previously mentioned, Louks and Susmel [29] used a similar approach to the one proposed in this work when predicting fatigue limits according to the PM and LM. The accuracy of these predictions were summarized in table 3.4 in section 3.6.3, and show that the absolute errors are slightly less than the ones obtained in this work. This can probably be related to the fact that Louks and Susmel used notched specimens that were not produced by AM and had higher k_t-values than the ones used in this work, both when determining the critical distance and for the specimens that were assessed. Higher k_t-values give more accurate prediction results, at least when following the inverse search procedure, according to Santus et al. [75]. It is likely that this applies as a general rule when predicting fatigue limits according to the PM and LM, and not only for the inverse search procedure, because the specimens are more likely to fail at the notch tip when k_t is large. This is because high k_t-values will cause the notch to be more critical than local defects. When the specimens fail at the notch tip, the stress fields along the notch bisector line that are used in both the PM and LM, will better represent the stresses that causes failure in the physical tests. This is especially important for AMed components where other factors, such as high surface roughness and defects, can cause failure to initiate at other locations than the notch tip.

From the results in table 8.8, it is also evident that the accuracy of the fatigue limit predictions of the semicircular specimen is significantly lower than that of the blunt V-notched. This applies for both the PM and LM. A possible explanation to this is the fact that the semicircular specimens fail at positions higher up in the overhang region, as was reported by Solberg and Berto [17], whereas the blunt and sharp V-notched specimens tend to fail closer to the notch root. This means that the stress fields along the notch bisector line of the semicircular specimens, that were used for both the PM and LM, does not represent the stress distribution at the failure location as accurately as the stress fields of the blunt and sharp V-notched specimens does. However, it must be stressed that both the PM and LM are able to predict the fatigue limit of the semicircular specimens with an absolute error below 20%. This indicates that these two stress based approaches are suitable for assessing components produced by AM with a promising accuracy. This is despite the fact that the AMed semicircular specimens does not fail at the notch root.

10.3   Effect of Heat Treatment

Figure 6.6 and 6.8 illustrated the microstructure of the AMed Inconel 718 specimens before and after heat treatment. From these micrographs, it can be seen that the heat treatment has an effect on the microstructural features of the material. The grain size seems to increase, and the building layers are no longer visible. However, some features that were also seen in the as-built microstructure are still visible after heat treatment. Hatching lines and some melt pools can be seen after heat treatment, and the grains are still elongated in the build-direction.

When studying the effect of heat treatment on SLMed Inconel 718, M. E. Aydinöz et al., [51] found that HIP performed at 1150°C recrystallizes the material and eliminates the preferential grain orientation, and that solution annealing at 1000°C is not sufficient to remove the preferential grain orientation. These results were reported in figure 5.1. In the NASA tests [60], the material was recrystallized when performing heat treatment with a maximum temperature of 1165°C, as was seen in figure 5.4. Gribbin et al. [41] and S. Emuakpor et al. [61] also found that heat treatment temperatures close to 1200°C leads to recrystallization.

Based on the findings from literature, it is likely that only a slight increase of the annealing temperature of 1095°C used in this work, would have led to complete recrystallization. For instance, the heat treatment of the tensile specimens presented in section 6.2, with an annealing temperature of 1200°C, removed all characteristics stemming from the AM process as well as the preferential grain orientation.

In terms of porosities, the heat treatment conducted in this work does not seem to treat this problem. Figure 6.9 show that porosities are still present after the heat treatment. Considering that the specimens did not undergo HIP, this is not a surprising observation. HIP has been reported to have a positive effect on the presence of porosities [51, 76, 77].

Critical Distance Dependency on Heat Treatment
In section 3.6.3, the relationship between microstructural features and the critical distance was introduced. Taylor [36] investigated the effect of grain size on critical distance, based on brittle fracture of specimens subjected to different types of heat treatment. The results revealed that the critical distance increased with increasing grain size. Negru et al. [38] employed the PM to determine the critical distance of PUR material with different densities, and found that the critical distance increased with decreasing density. Both these findings suggest that the critical distance increases with increasing size of the microstructural features of the material.

In section 8.5, the effect of heat treatment on the critical distance was investigated. This was done by employing both the PM and LM, based on fatigue data of as-built and heat treated blunt V-notched and unnotched specimens. The resulting critical distances versus N_f were plotted in figure 8.19 and 8.20, for PM and LM, respectively. From these curves, it can be seen that the difference in critical distance for as-built and heat treated specimens is large for lower number of cycles to failure, with the heat treated specimens having higher critical distance. For higher N_f, the difference decreases, and at 2×10^6 cycles to failure, the critical distance for as-built and heat treated specimens are almost identical.

The fact that the critical distance is higher for the heat treated specimens can possibly be related to the fact that the heat treated specimens seemed to have larger grain size than the as-built specimens. This is line with what was observed in literature, where the critical distance was observed to increase with increasing size of the microstructural features. However, the dependency on N_f on the difference in critical distance between the as-built and heat treated specimens is an interesting observation. This finding is related to the 50 % confidence bands that were used to create the stress fields at 10^5, 5×10^5, 10^6 and 2×10^6 cycles to failure, for the as-built and heat treated specimens. As seen in figure 8.18, the stress fields of the unnotched and blunt V-notched specimens, at $N_f = 2 \times 10^6$, intersect at the same distance from the notch root for both the as-built and heat treated specimens, effectively giving almost identical $L/2$ values according to the PM. This is because the increase in fatigue strength after heat treatment is almost identical for both the unnotched and blunt V-notched specimens at $N_f = 2 \times 10^6$, as can be seen from the data in table 8.2 and 7.1. For the blunt V-notched specimens, the fatigue strength at $N_f = 2 \times 10^6$ increases by a factor of 1.675 when going from as-built to heat treated. The factor for the unnotched specimens is 1.682, which is very similar, meaning that the stress fields of the blunt V-notched and unnotched specimens are shifted by essentially the same amount when going from as-built to heat treated. This causes the stress fields at $N_f = 2 \times 10^6$ to intersect at almost the same distance from the notch root, before and after heat treatment.

At lower number of cycles to failure, the increase in fatigue strength due to the heat treatment is not the same for the unnotched and blunt V-notched specimens. At lower N_f, the heat treatment has a relatively larger positive effect on the blunt V-notched specimens with respect to the unnotched specimens, causing the stress fields of the heat treated specimens to intersect further away from the notch root, effectively giving larger critical distance values for the heat treated specimens. The physical explanation of the similarities in the critical distance at higher number of cycles to failure is difficult to explain without performing additional fatigue tests. Due to the scatter in the fatigue data, it is possible that additional tests would yield different results. In addition, heat treated sharp V-notched specimens should be fatigue tested in order to more accurately evaluate the critical distance of heat treated AMed Inconel 718.

10.4 Modification of Fatigue Data

In section 8.4, the fatigue data of AMed as-built Inconel 718 was modified with respect to the average $L/2$-value found according to the PM. By using $L/2 = 0.085mm$, the fatigue data of the semicircular, blunt V-notched and sharp V-notched specimens was plotted as the stress range at $L/2$ versus number of cycles to failure, instead of using the nominal stress range. The average $L/2$-value of $0.085mm$ was used in order to better represent the $L/2$-values of the material over the entire span of number of cycles to failure. The resulting plots showed little scatter, with a scatter parameter of $T_{\Delta\sigma} = 1.289$. This finding suggests that the modification of the fatigue data based on the average $L/2$ value is a promising approach to represent the fatigue data of a given material. The approach allows for a representation of the fatigue data that does not depend on the specimen geometry.

It can however be argued that more accurate results could have been obtained by using other $L/2$ values than the average one. For example, the critical distance could have been determined for each data point of the fatigue tests, based on the 50% confidence bands. This would require that the stress fields of the sharp V-notched and unnotched specimens are created for the N_f value corresponding to each data point. In that way, the stress ranges at $L/2$ could be plotted versus N_f, using the exact $L/2$ value corresponding to each particular N_f. A procedure like this would however be time consuming.

10.5 Offset Procedure

10.5.1 Applications of the Offset Procedure

In this section, some possible applications of the offset procedure are presented and discussed. When working with specific problems, these applications require that the critical distance of the material is known beforehand.

Fatigue Assessment Approach
Having shown that it is possible to investigate the stresses at a desired distance from the surface of a component, following the offset procedure described in section 9.1, the procedure can be combined with principles of the TCD. The results from section 8.4 showed promising results in terms of modifying the fatigue data with respect to the average $L/2$ value obtained according to the PM. This modified fatigue data can be used to assess the fatigue strength of any AMed as-built Inconel 718 component, by evaluating its stresses at a distance of 0.085 mm from the surface.
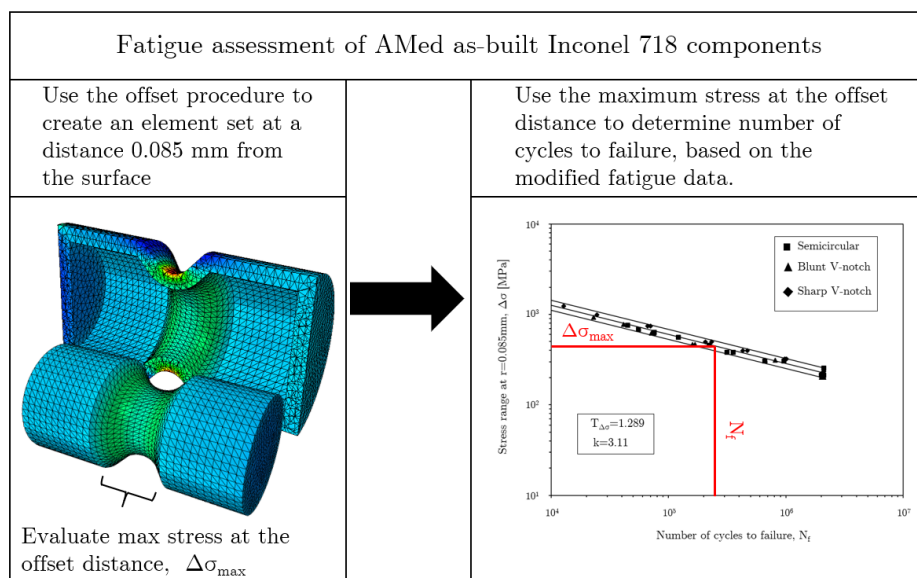
Figure 10.2: Fatigue assessment approach of AMed as-built Inconel 718, based on the offset procedure and modified fatigue data.

With the basis of the notched cylinder presented in section 9.1, figure 10.2 shows how a fatigue assessment based on the offset procedure and the modified fatigue data is carried

out. If the offset distance is set to $L/2 = 0.085mm$, the stress range at the offset surface can be used to evaluate the fatigue life of the component directly from the modified SN-curve. A procedure like this allows for performing fatigue assessments without having to determine the stress concentration factor and notch sensitivity. Using an $L/2$ value of 0.085 mm obviously only applies for the AMed as-built Inconel 718 presented here. If this procedure is to be used on another material, the offset distance and modified fatigue data must correspond to the properties of that particular material.

Critical Region Identification

Identification of the regions governing the performance of a component is an important task when designing or improving its design. It is also crucial to have information about the critical region when assessing the component's properties in terms of static and fatigue strength.

Taylor et al. [31] predicted the fatigue failure location of a cast iron automotive suspension component containing two distinct stress raising features by using the PM. The basis of this study was the inadequate results obtained when using a FE software to determine the fatigue life of the component. The FE software predicted failure at the stress raising feature with the highest stress at the notch tip, and not at the location that was observed from the physical tests of the suspension component. By creating node paths at the two stress raising features and investigating the stresses at a distance from the notch tips, the PM was successfully employed to predict the correct failure location, namely, the stress raising feature with the highest stress at a distance $L/2$ from the notch tip. This finding suggests that the fatigue life is governed by the stresses at a distance from the notch tip, rather than the peak stress at the notch tip.

Introducing the component in figure 10.3, it can be shown how the offset procedure described in section 9.1 can be used to identify the critical region of a component containing more than one stress raiser, by using the PM. The component in question is a cylinder with two notches, one sharp and shallow and one deep and blunt, and the offset procedure is used to analyze the stresses at an arbitrary distance of 0.6 mm from the surface.
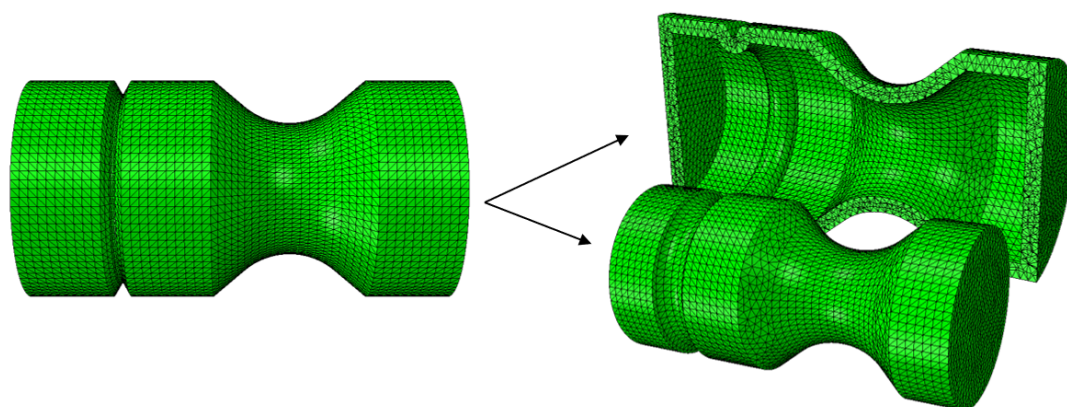
Figure 10.3: External and internal element sets of the two-notched cylinder.

Running a stress analysis with a tensile unit load, the stresses at the offset distance from the surface can be studied. As the results in figure 10.4 show, the shallow and sharp notch has the highest peak stress at the notch tip, whereas the blunt notch has the highest stress at a distance 0.6 mm from the surface. In order to apply this procedure to a

component of any given material, the offset distance of 0.6 mm can simply be changed to the $L/2$ value of that particular material. This will effectively allow for a convenient determination of the critical region based on the PM. For instance, the automotive suspension component analyzed by Taylor et al. [31] could have been investigated by means of the offset procedure with an offset distance corresponding to the $L/2$ value of cast iron, instead of using node paths.
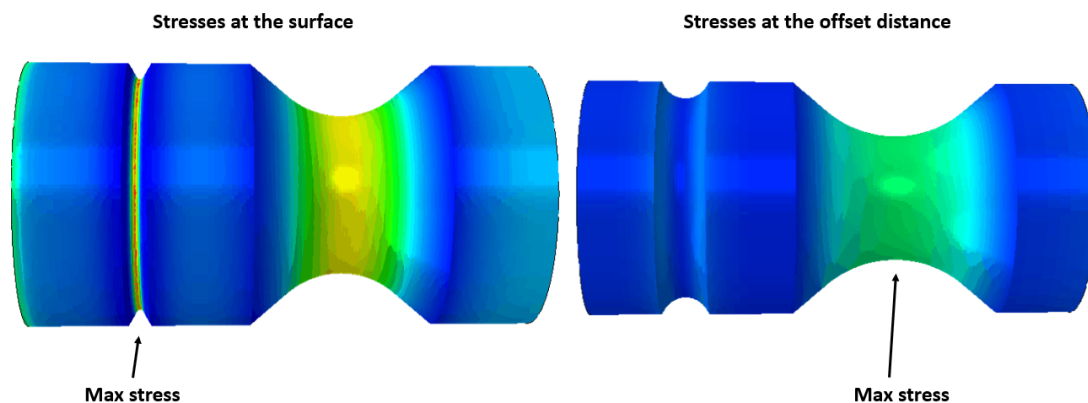
Figure 10.4: Maximum stresses at the surface (left) and at a distance 0.6 mm from the surface (right) of the two-notched cylinder.

Shape Optimization

Shape optimization can be a useful tool when making final design modifications to a component. By slightly changing the surface geometry, the component can be optimized to minimize stress and strain, and to maximize durability. As was mentioned in section 3.5, Tosca is a commercial software that can be implemented in Abaqus to perform optimization tasks. The Tosca shape optimization is here used to illustrate how the critical region identification presented above can be used to make better design decisions.

With the basis of the cylinder with two notches from figure 10.3, Tosca shape optimization is used to reduce the peak stresses. This is done by selecting the regions to be optimized, and allowing the software to modify the surface nodes and keeping the volume constant. Under the postulation that the critical region of the two-notched cylinder is located at the blunt notch where the stress at the offset distance is highest, the shape optimization can be performed locally at this notch only. This result is reported in Appendix B.1, with stress reduction and elapsed time indicated.

If the entire cylinder is shape optimized with respect to reduction of peak stresses, the results in Appendix B.2 are obtained. These results reveal the importance of having information about the critical regions of the component before performing the shape optimization. Even though the same results are obtained in terms of stress reduction at the critical notch, the time consumption is drastically reduced when the optimization is only performed at the critical region.

10.5.2   Shortcomings of the Offset Procedure

Mesh

A deciding factor for the applicability and scalability of the offset procedure is the mesh

size. When the partition surface is created in Abaqus by merging the original part and the offset part, the distance between the outer surface and the partition surface is given by the offset distance. It is obvious that when the partitioned part is meshed, the elements need to be sufficiently small in order to fit between the outer surface and the partitioned surface. Appendix C includes a mesh sensitivity analysis of a notched cylindrical specimen with constant outer dimensions. By applying the offset procedure with different offset distances, the max. principal stresses at the outer surface and the offset surface, at unit load, are measured in the notched cross section of the cylinder. For a given offset distance, the mesh size is gradually reduced. The results show that the maximum stress at the offset surface seems to converge at approximately the same mesh size as the outer surface. This suggests that the offset stresses are as mesh sensitive as the surface stresses, meaning that it can be expected that the stress at the offset distance converges if the stress at the surface converges.

The results in Appendix C also show that a shorter offset distance dictates the maximum feasible mesh size. For instance, when the offset distance is decreased to 0.4, the mesh size cannot be greater than 3.5. This is because the distance between the outer surface and the offset surface is too short for larger mesh sizes than 3.5. It can also be seen that a shorter offset distance causes a greater amount of distorted elements. This is because the elements will always try to align with the offset, or partition surface, and will have poor shape if the element size is too large with respect to the offset distance. It can thus be assumed that the offset procedure will require a dense mesh, and hence high computational time, if the offset distance is decreased even further. For example, the average $L/2$ value of as-built Inconel 718 that was used to modify the fatigue data in section 8.4 would require an offset distance of $0.085mm$. If a fatigue assessment of a large as-built Inconel 718 component is to be carried out according to the fatigue assessment approach proposed in section 10.5.1, a dense mesh, and consequently a large amount of elements would be required. This illustrates the problem with scalability of the offset procedure, where a large component with a short critical distance requires large computational effort.

In summary, the offset procedure will in many cases require what can be seen as an unnecessary dense mesh. This happens if the mesh density required for the surface stresses to converge, causes elements that are too large to fit between the outer surface and the offset surface. The mesh density would then need to be increased until the elements are sufficiently small to fit between the two surfaces, consequently causing a mesh density larger than what was needed for the surface stresses to converge.

Geometries

One obvious limitation of the offset procedure is the inability to obtain a constant offset distance of parts containing sharp edges. To the left in figure 10.5, it can be seen how an offset surface stemming from a part with a sharp corner does not represent an offset surface with a constant distance from the original surface. The offset distance at the corner is clearly larger than the offset distance elsewhere in the component. This issue can be overcome by simply introducing small radii at each sharp corner, effectively creating rounded corners instead of sharp corners. This is seen to the right in figure 10.5. Introducing such radii obviously requires a modification of the geometry and can in some cases affect the performance of the component. It can however be argued that the introduction of rounded corners will not be necessary in many cases, because the critical

regions of components often do not contain sharp corners.

a) Sharp corner   b) Rounded corner
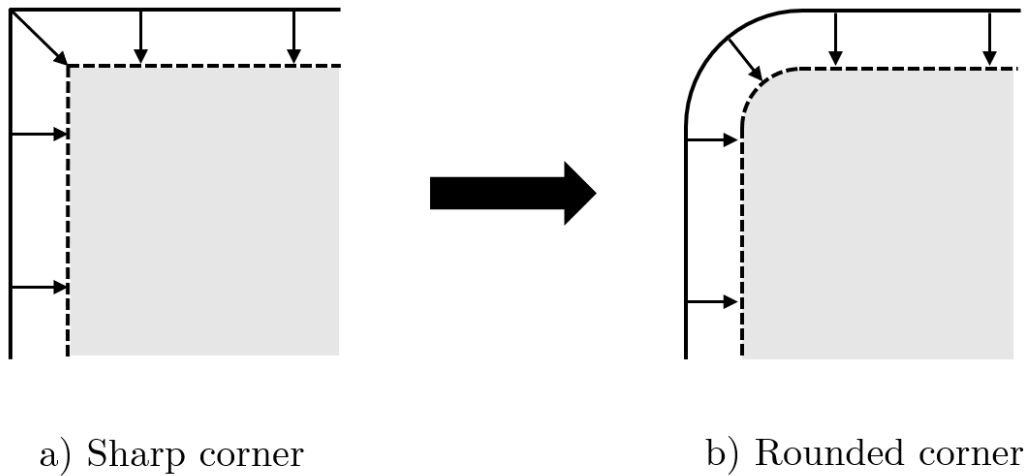
Figure 10.5: Introducing rounded corners to obtain a constant offset distance.

10.5.3   Extending on the Offset Procedure

Implementation in Abaqus
Having discussed that the offset procedure has certain limitations when it comes to meshing of components with small critical distances, it can be argued that the procedure could be improved to overcome these challenges. For instance, the investigation of stresses at a distance from the component surface could be implemented in the visualization module in Abaqus. By selecting all component-surfaces, the stresses at a desired distance from the surface could be studied by "cutting" through the elements close to the surface. This is similar to what can be done with section view in the visualization module, but rather than using planes, the component surfaces are used as a basis for investigating the internal stresses of the component. An approach like this would effectively eliminate the need for making an offset part for each original part, and not having to follow all the Abaqus-steps presented in Appendix A. In addition, the mesh would not need to be as dense as for the offset procedure, because the elements do not have to fit between the outer surface and the partition surface. The mesh would only need to be dense enough for the surface stresses to converge.

11 Conclusion

The aim of this thesis was to investigate the applicability of the TCD for fatigue assessment of AMed Inconel 718 specimens, as well as proposing an alternative engineering approach based on the TCD. The applicability of the TCD was determined based on fatigue data obtained from literature, as well as data obtained through fatigue tests presented in this work. This fatigue data includes both heat treated and as-built specimens.

- The critical distance of as-built Inconel 718 decreases with number if cycles to failure.

- Both the PM and LM were successfully employed to predict the fatigue limit of the semicircular and blunt V-notched specimens with an absolute error below 20 %.

- The fatigue limit prediction is less accurate for specimens whose failure location is further away from the notch root, as was seen for the semicircular specimens.

- By modifying the fatigue data of as-built AMed Inconel 718, based on the average $L/2$ value obtained according to the PM, the resulting plot shows little scatter. The modified fatigue data can be used for fatigue assessment without having to consider the component geometry.

- Heat treatment seemed to cause an increase in grain size, and removed the build-layers from the AMed specimens. The heat treated specimens did however contain elongated grains in the build-direction, and the hatching lines and some melt pools were still visible after heat treatment. In addition, the heat treatment process did not affect the presence of pores.

- After heat treatment, the critical distance increases with respect to the as-built specimens, for lower number of cycles to failure. At higher N_f, the difference in critical distances between as-built and heat treated specimens decreases. At $N_f = 2 \times 10^6$, the critical distances of as-built and heat treated specimens are almost identical.

- A procedure for investigating the stresses at a distance from the surface of a component was proposed. The offset procedure can be used to assess the stresses at an offset distance from the surface without creating node paths.

- A combination of the offset procedure and the modified fatigue data was presented and discussed in terms of its applicability for fatigue assessment of a given component.

- The offset procedure can be used to identify the critical regions of a component, based on TCD principles. This is done by identifying the region of the component where the stress at the half of the materials' critical distance is largest.

- The offset procedure can be used as a basis for making design decisions, such as shape optimization of a component.

- The offset procedure has certain limitations when applied to large components made of materials with a short critical distance. In these situations, the mesh needs to be dense and the computational time will in consequence be large. In addition, the offset procedure has limitations when the component in question contains sharp edges.

Further Work

In order to further investigate the applicability of the PM and LM for fatigue assessment of AMed Inconel 718, more specimens with different geometries should be fatigue tested. This would give a better foundation for determining whether the TCD approaches are suitable, and to investigate factors influencing the accuracy. For instance, the accuracy of the fatigue limit predictions seemed to decrease when the failure location was located further away from the notch root, as was seen for the semicircular specimens. Additional specimens whose failure location is even further away from the notch root could be tested and assessed. This would allow for an investigation of the sensitivity of the TCD approaches towards the position of the failure location. By testing additional specimens with different geometries, the effect on the scatter of the modified fatigue data could also be studied. It would be of interest to investigate if the scatter parameter decreases or increases as more fatigue data is added to the modified fatigue plot.

The effect of heat treatment was investigated in this work, however, additional testing of heat treated specimens should be conducted. This includes heat treatment of sharp notched specimens to more accurately determine the critical distance values after heat treatment, as well as a more thorough investigation of the microstructural features caused by heat treatment and their effect on the critical distance. The effect of the presence of pores also needs further investigation, as pores were detected in the material both before and after heat treatment. It is well known that pores and other defects close to the surface of the component can serve as initiation points for fatigue cracks, and it is thus important to relate the size and shape of these defects to the TCD.

As for the offset procedure, further testing and validation is necessary. This can be done by applying the procedure on real life problems and comparing with physical results, similar to what was done for the vehicle component tested by Taylor et al. [31], presented in section 10.5.1. The testing and validation should also include an investigation of the ability of the procedure to cope with multiaxial loads, since this has not been addressed in this work and multiaxial loads are often present in real engineering components.

In terms of improving the offset procedure, a possible improvement involving implementation in the visualization module in Abaqus has already been introduced in section 10.5.3. Implementing such a feature in Abaqus would be of interest because it will reduce the computational power for each analysis, effectively enabling the possibility of analyzing larger components with short critical distances. The Abaqus implementation would also be more flexible considering that it would not be necessary to follow all the steps associated with the offset procedure presented in this work.

References

[1] Special Metals Corporation. *Inconel Alloy 718*. accessed: 07/11/2018. 2007. URL: http://www.specialmetals.com/assets/smc/documents/inconel_alloy_718.pdf.

[2] D. Taylor. *The Theory of Critical Distances: A New Perspective in Fracture Mechanics*. Elsevier Science, 2007. ISBN: 9780080444789.

[3] Marius Hornnes. "Structural Integrity of Additively Manufactured Inconel 718". *Norwegian University of Science and Technology*. 12/12/2018.

[4] *Diagram covers AM machines and processes | Materials Today*. 29/10/2018. 2015. URL: https://www.materialstoday.com/additive-manufacturing/news/diagram-covers-am-machines-and-processes/.

[5] *Binder Jetting | Additive Manufacturing Research Group | Loughborough University*. 2018-10-28. URL: http://www.lboro.ac.uk/research/amrg/about/the7categoriesofadditivemanufacturing/binderjetting/.

[6] *Sheet Lamination | Additive Manufacturing Research Group | Loughborough University*. 2018-10-28. URL: http://www.lboro.ac.uk/research/amrg/about/the7categoriesofadditivemanufacturing/sheetlamination/.

[7] *Powder Bed Fusion | Additive Manufacturing Research Group | Loughborough University*. 06/11/2018. URL: %5Curl%7Bhttp://www.lboro.ac.uk/research/amrg/about/the7categoriesofadditivemanufacturing/powderbedfusion/%7D.

[8] Stella Holzbach OLIARI, Ana Sofia Clímaco Monteiro D'OLIVEIRA, and Martin SCHULZ. "Additive Manufacturing of H11 with Wire-Based Laser Metal Deposition". In: *Soldagem & Inspeção* 22.4 (2017), pp. 466–479. ISSN: 0104-9224. DOI: https://dx.doi.org/10.1590/0104-9224/si2204.06. URL: %5Curl%7Bhttp://www.scielo.br/scielo.php?script=sci_arttext&pid=S0104-92242017000400466%7D.

[9] Ahmad Zadi-Maad. "The development of additive manufacturing technique for nickel-base alloys: A review". In: vol. 1945. Mar. 2018. DOI: 10.1063/1.5030286.

[10] *DMLS vs SLM 3D Printing for Metal Manufacturing*. 06/11/2018. URL: https://www.element.com/nucleus/2016/06/29/dmls-vs-slm-3d-printing-for-metal-manufacturing.

[11] *Electron Beam Melting - EBM Process, Additive Manufacturing*. 06/11/2018. URL: http://www.arcam.com/technology/electron-beam-melting/.

[12] W. J. Sames et al. "The metallurgy and processing science of metal additive manufacturing". In: *International Materials Reviews* 61.5 (2016), pp. 315–360. DOI: https://doi.org/10.1080/09506608.2015.1116649. URL: https://www.tandfonline.com/doi/full/10.1080/09506608.2015.1116649.

[13] Chor Yen Yap et al. "Review of selective laser melting: Materials and applications". In: *Applied Physics Reviews* 2 (Dec. 2015), p. 041101. DOI: 10.1063/1.4935926.

[14] M. Brandt. *Laser Additive Manufacturing: Materials, Design, Technologies, and Applications.* Woodhead Publishing Series in Electronic and Optical Materials. Elsevier Science, 2016. Chap. 2.2.1. ISBN: 9780081004340. URL: https://books.google.no/books?id=H32nCgAAQBAJ.

[15] M. Brandt. *Laser Additive Manufacturing: Materials, Design, Technologies, and Applications.* Woodhead Publishing Series in Electronic and Optical Materials. Elsevier Science, 2016. Chap. 2.4.4. ISBN: 9780081004340. URL: https://books.google.no/books?id=H32nCgAAQBAJ.

[16] Jason C. Fox, Shawn P. Moylan, and Brandon M. Lane. "Effect of Process Parameters on the Surface Roughness of Overhanging Structures in Laser Powder Bed Fusion Additive Manufacturing". In: *Procedia CIRP* 45 (2016). 3rd CIRP Conference on Surface Integrity, pp. 131–134. ISSN: 2212-8271. DOI: https://doi.org/10.1016/j.procir.2016.02.347. URL: http://www.sciencedirect.com/science/article/pii/S2212827116006429.

[17] K. Solberg and F. Berto. "Notch-defect interaction in additively manufactured Inconel 718". In: *International Journal of Fatigue* 122 (2019), pp. 35–45. ISSN: 0142-1123. DOI: https://doi.org/10.1016/j.ijfatigue.2018.12.021. URL: http://www.sciencedirect.com/science/article/pii/S0142112318307382.

[18] C. Li et al. "Residual Stress in Metal Additive Manufacturing". In: *Procedia CIRP* 71 (2018). 4th CIRP Conference on Surface Integrity (CSI 2018), pp. 348–353. ISSN: 2212-8271. DOI: https://doi.org/10.1016/j.procir.2018.05.039. URL: http://www.sciencedirect.com/science/article/pii/S221282711830667X.

[19] N. E Dowling. *Mechanical behavior of materials: Engineering methods for deformation, fracture, and fatigue.* Boston: Pearson, 2013. ISBN: 9780273764557.

[20] *The tension test - LS-DYNA Support | The tension test.* 29/10/2018. URL: https://www.dynasupport.com/tutorial/computational-plasticity/the-tension-test.

[21] R. He and H. Wang. "Deformation behavior in high-frequency fatigue failure of laser melting deposited Ti-6Al-2Zr-Mo-V alloys". In: *Xiyou Jinshu Cailiao Yu Gongcheng/Rare Metal Materials and Engineering* 39.2 (2010). cited By 6, pp. 288–291. URL: %5Curl%7Bhttps://www.scopus.com/inward/record.uri?eid=2-s2.0-77950555291&partnerID=40&md5=20763dffd99f353bb0efad13a72a4452%7D.

[22] *Siemens PLM Community.* 30/10/2018. 2018. URL: https://community.plm.automation.siemens.com/t5/Testing-Knowledge-Base/What-is-a-SN-Curve/ta-p/355935.

[23] T. L. Anderson. *Fracture Mechanics: Fundamentals and Applications, Third Edition.* New York, NY: Taylor & Francis, 2005.

[24] P. Lazzarin and S. Filippi. "A generalized stress intensity factor to be applied to rounded V-shaped notches". In: *International Journal of Solids and Structures* 43.9 (2006), pp. 2461–2478. ISSN: 0020-7683. DOI: https://doi.org/10.1016/j.ijsolstr.2005.03.007. URL: http://www.sciencedirect.com/science/article/pii/S0020768305001186.

[25] SIMULA. *Abaqus 2016 Documentation.* Version 2016. 29/04/2019. URL: http://130.149.89.49:2080/v2016/books/usi/default.htm.

[26] SIMULA. *Abaqus 2016 Documentation*. Version 2016. 29/04/2019. URL: `%5Curl%7Bhttp://130.149.89.49:2080/v2016/books/usb/default.htm?startat=pt04ch13s02aus88.html%7D`.

[27] David Taylor. "CHAPTER 2 - The Theory of Critical Distances: Basics: An Introduction to the Basic Methodology of the TCD". In: *The Theory of Critical Distances*. Ed. by David Taylor. Oxford: Elsevier Science Ltd, 2007, pp. 21–31. ISBN: 978-0-08-044478-9. DOI: `https://doi.org/10.1016/B978-008044478-9/50003-X`. URL: `http://www.sciencedirect.com/science/article/pii/B978008044478950003X`.

[28] David Taylor. "Applications of the theory of critical distances in failure analysis". In: *Engineering Failure Analysis* 18.2 (2011). The Fourth International Conference on Engineering Failure Analysis Part 1, pp. 543–549. ISSN: 1350-6307. DOI: `https://doi.org/10.1016/j.engfailanal.2010.07.002`. URL: `http://www.sciencedirect.com/science/article/pii/S1350630710001287`.

[29] R. Louks and L. Susmel. "The linear-elastic Theory of Critical Distances to estimate high-cycle fatigue strength of notched metallic materials at elevated temperatures". In: *Fatigue & Fracture of Engineering Materials & Structures* 38.6 (), pp. 629–640. DOI: `10.1111/ffe.12273`. eprint: `https://onlinelibrary.wiley.com/doi/pdf/10.1111/ffe.12273`. URL: `https://onlinelibrary.wiley.com/doi/abs/10.1111/ffe.12273`.

[30] David Taylor. "CHAPTER 3 - The Theory of Critical Distances in Detail: The History, Background and Precise Definition of the TCD". In: *The Theory of Critical Distances*. Ed. by David Taylor. Oxford: Elsevier Science Ltd, 2007, pp. 33–49. ISBN: 978-0-08-044478-9. DOI: `https://doi.org/10.1016/B978-008044478-9/50004-1`. URL: `http://www.sciencedirect.com/science/article/pii/B9780080444789500041`.

[31] D. Taylor, P. Bologna, and K. Bel Knani. "Prediction of fatigue failure location on a component using a critical distance method". In: *International Journal of Fatigue* 22.9 (2000), pp. 735–742. ISSN: 0142-1123. DOI: `https://doi.org/10.1016/S0142-1123(00)00062-1`. URL: `http://www.sciencedirect.com/science/article/pii/S0142112300000621`.

[32] M. Benedetti and C. Santus. "Notch fatigue and crack growth resistance of Ti-6Al-4V ELI additively manufactured via selective laser melting: A critical distance approach to defect sensitivity". In: *International Journal of Fatigue* 121 (2019), pp. 281–292. ISSN: 0142-1123. DOI: `https://doi.org/10.1016/j.ijfatigue.2018.12.020`. URL: `http://www.sciencedirect.com/science/article/pii/S0142112318307084`.

[33] C. Santus, D. Taylor, and M. Benedetti. "Determination of the fatigue critical distance according to the Line and the Point Methods with rounded V-notched specimen". In: *International Journal of Fatigue* 106 (2018), pp. 208–218. ISSN: 0142-1123. DOI: `https://doi.org/10.1016/j.ijfatigue.2017.10.002`. URL: `http://www.sciencedirect.com/science/article/pii/S0142112317303948`.

[34] B. ATZORI, G. MENEGHETTI, and L. SUSMEL. "Material fatigue properties for assessing mechanical components weakened by notches and defects". In: *Fatigue & Fracture of Engineering Materials & Structures* 28.12 (2005), pp. 83–97. DOI: `10.1111/j.1460-2695.2004.00862.x`. eprint: `https://onlinelibrary.wiley.com/doi/pdf/10.1111/j.1460-2695.2004.00862.x`. URL: `https://onlinelibrary.wiley.com/doi/abs/10.1111/j.1460-2695.2004.00862.x`.

[35] Qiang Chen, Norio Kawagoishi, and Hironobu Nisitani. "Evaluation of notched fatigue strength at elevated temperature by linear notch mechanics". In: *International Journal of Fatigue* 21.9 (1999), pp. 925–931. ISSN: 0142-1123. DOI: `https://doi.org/10.1016/S0142-1123(99)00081-X`. URL: `http://www.sciencedirect.com/science/article/pii/S014211239900081X`.

[36] David Taylor. "The Theory of Critical Distances Applied to the Prediction of Brittle Fracture in Metallic Materials". In: *Struct. Integrity Durab.* 1 (June 2005).

[37] T. Yokobori and S. Konosu. "Effects of ferrite grain size, notch acuity and notch length on brittle fracture stress of notched specimens of low carbon steel". In: *Engineering Fracture Mechanics* 9.4 (1977), pp. 839–847. ISSN: 0013-7944. DOI: `https://doi.org/10.1016/0013-7944(77)90006-6`. URL: `http://www.sciencedirect.com/science/article/pii/0013794477900066`.

[38] R. Negru et al. "Application of TCD for brittle fracture of notched PUR materials". In: *Theoretical and Applied Fracture Mechanics* 80 (2015). 1st Multi-lateral workshop on Fracture and Structural Integrity related issues, pp. 87–95. ISSN: 0167-8442. DOI: `https://doi.org/10.1016/j.tafmec.2015.05.005`. URL: `http://www.sciencedirect.com/science/article/pii/S0167844215202054`.

[39] David Taylor. "CHAPTER 9 - Fatigue: Predicting Fatigue Limit and Fatigue Life". In: *The Theory of Critical Distances*. Ed. by David Taylor. Oxford: Elsevier Science Ltd, 2007, pp. 163–196. ISBN: 978-0-08-044478-9. DOI: `https://doi.org/10.1016/B978-008044478-9/50010-7`. URL: `http://www.sciencedirect.com/science/article/pii/B9780080444789500107`.

[40] David Taylor. "Analysis of fatigue failures in components using the theory of critical distances". In: *Engineering Failure Analysis* 12.6 (2005). Papers presented at the First International Conference on Engineering Failure Analysis (Lisbon, Portugal, 12 14 July 2004). Part II, pp. 906–914. ISSN: 1350-6307. DOI: `https://doi.org/10.1016/j.engfailanal.2004.12.007`. URL: `http://www.sciencedirect.com/science/article/pii/S1350630705000324`.

[41] Sean Gribbin et al. "Low cycle fatigue behavior of direct metal laser sintered Inconel alloy 718". In: *International Journal of Fatigue* 93 (2016), pp. 156–167. ISSN: 0142-1123. DOI: `https://doi.org/10.1016/j.ijfatigue.2016.08.019`. URL: `http://www.sciencedirect.com/science/article/pii/S0142112316302614`.

[42] Zhou, Zhongjiao et al. "The effect of texture on the low cycle fatigue property of Inconel 718 by selective laser melting". In: *MATEC Web Conf.* 165 (2018), p. 02007. DOI: `10.1051/matecconf/201816502007`. URL: `https://doi.org/10.1051/matecconf/201816502007`.

[43] G.Appa Rao et al. "Effect of standard heat treatment on the microstructure and mechanical properties of hot isostatically pressed superalloy inconel 718". In: *Materials Science and Engineering: A* 355.1 (2003), pp. 114–125. ISSN: 0921-5093. DOI: https://doi.org/10.1016/S0921-5093(03)00079-0. URL: http://www.sciencedirect.com/science/article/pii/S0921509303000790.

[44] I.A Choudhury and M.A El-Baradie. "Machinability of nickel-base super alloys: a general review". In: *Journal of Materials Processing Technology* 77.1 (1998), pp. 278–284. ISSN: 0924-0136. DOI: https://doi.org/10.1016/S0924-0136(97)00429-9. URL: http://www.sciencedirect.com/science/article/pii/S0924013697004299.

[45] T. Gladman. "Precipitation hardening in metals". In: *Materials Science and Technology* 15.1 (1999), pp. 30–36. DOI: 10.1179/026708399773002782. eprint: https://doi.org/10.1179/026708399773002782. URL: https://doi.org/10.1179/026708399773002782.

[46] Z.S. Yu et al. "Microstructural evolution and mechanical properties of Inconel 718 after thermal exposure". In: *Materials Science and Engineering: A* 634 (2015), pp. 55–63. ISSN: 0921-5093. DOI: https://doi.org/10.1016/j.msea.2015.03.004. URL: http://www.sciencedirect.com/science/article/pii/S0921509315002099.

[47] M.C. Chaturvedi and Y. Han. "Creep deformation of alloy 718". In: *Superalloy 718-metallurgy and Applications* (1989). cited By 7, pp. 489–498.

[48] Saied Azadian, Liu-Ying Wei, and Richard Warren. "Delta phase precipitation in Inconel 718". In: *Materials Characterization* 53.1 (2004), pp. 7–16. ISSN: 1044-5803. DOI: https://doi.org/10.1016/j.matchar.2004.07.004. URL: http://www.sciencedirect.com/science/article/pii/S1044580304001603.

[49] M.M. Kirka et al. "Effect of anisotropy and texture on the low cycle fatigue behavior of Inconel 718 processed via electron beam melting". In: *International Journal of Fatigue* 105 (2017), pp. 235–243. ISSN: 0142-1123. DOI: https://doi.org/10.1016/j.ijfatigue.2017.08.021. URL: http://www.sciencedirect.com/science/article/pii/S014211231730350X.

[50] Katia Cristiane Gandolpho Candioto et al. "Characterization of the Superalloy Inconel 718 After Double Aging Heat Treatment". In: *Mechanical and Materials Engineering of Modern Structure and Component Design*. Ed. by Andreas Öchsner and Holm Altenbach. Cham: Springer International Publishing, 2015, pp. 293–300. ISBN: 978-3-319-19443-1. DOI: 10.1007/978-3-319-19443-1_24. URL: https://doi.org/10.1007/978-3-319-19443-1_24.

[51] M.E. Aydinöz et al. "On the microstructural and mechanical properties of post-treated additively manufactured Inconel 718 superalloy under quasi-static and cyclic loading". In: *Materials Science and Engineering: A* 669 (2016), pp. 246–258. ISSN: 0921-5093. DOI: https://doi.org/10.1016/j.msea.2016.05.089. URL: http://www.sciencedirect.com/science/article/pii/S0921509316306062.

[52] H.Y. Zhang et al. "Deformation characteristics of δ phase in the delta-processed Inconel 718 alloy". In: *Materials Characterization* 61.1 (2010), pp. 49–53. ISSN: 1044-5803. DOI: https://doi.org/10.1016/j.matchar.2009.10.003. URL: http://www.sciencedirect.com/science/article/pii/S1044580309003180.

[53] Shang Sui et al. "The influence of Laves phases on the high-cycle fatigue behavior of laser additive manufactured Inconel 718". In: *Materials Science and Engineering: A* 695 (2017), pp. 6–13. ISSN: 0921-5093. DOI: https://doi.org/10.1016/j.msea.2017.03.098. URL: http://www.sciencedirect.com/science/article/pii/S0921509317304148.

[54] A. S. Wilson. "Formation and effect of topologically close-packed phases in nickel-base superalloys". In: *Materials Science and Technology* 33.9 (2017), pp. 1108–1118. DOI: 10.1080/02670836.2016.1187335.

[55] B.P. Bewlay et al. "Solidification processing of high temperature intermetallic eutectic-based alloys". In: *Materials Science and Engineering: A* 192-193 (1995). 3rd International Conference on High Temperature Intermetallics, pp. 534–543. ISSN: 0921-5093. DOI: https://doi.org/10.1016/0921-5093(95)03299-1. URL: http://www.sciencedirect.com/science/article/pii/0921509395032991.

[56] CH RADHAKRISHNA and Prasad Kalvala. "The formation and control of Laves phase in superalloy 718 welds". In: *Journal of Materials Science* 32 (Apr. 1997), pp. 1977–1984. DOI: 10.1023/A:1018541915113.

[57] Matthew J. Donachie and Stephen J. Donachie. *Superalloys: A Technical Guide, 2nd Edition*. Jan. 2002, p. 439. ISBN: 9781615030644.

[58] R Cozar and Andre Pineau. "Morphology of y' and y" precipitates and thermal stability of inconel 718 type alloys". In: *Metallurgical Transactions* 4 (Jan. 1973), pp. 47–59. DOI: 10.1007/BF02649604.

[59] *Hot Isostatic Pressing (HIP) | European Powder Metallurgy Association (EPMA)*. 12/11/2018. URL: https://www.epma.com/hot-isostatic-pressing.

[60] D. Wells. *Overview of Fatigue and Damage Tolerance Performance of Powder Bed Fusion Alloy N07718*. 2018-10-29. 2016. URL: https://ntrs.nasa.gov/archive/nasa/casi.ntrs.nasa.gov/20160007069.pdf.

[61] O. Scott-Emuakpor et al. "Bending fatigue life characterisation of direct metal laser sintering nickel alloy 718". In: *Fatigue & Fracture of Engineering Materials & Structures* 38.9 (), pp. 1105–1117. DOI: 10.1111/ffe.12286. eprint: https://onlinelibrary.wiley.com/doi/pdf/10.1111/ffe.12286. URL: https://onlinelibrary.wiley.com/doi/abs/10.1111/ffe.12286.

[62] Laith Abdullah Al-Juboori, Thomas Niendorf, and Florian Brenne. "On the Tensile Properties of Inconel 718 Fabricated by EBM for As-Built and Heat-Treated Components". In: *Metallurgical and Materials Transactions B* (Sept. 2018). ISSN: 1543-1916. DOI: 10.1007/s11663-018-1407-4. URL: https://doi.org/10.1007/s11663-018-1407-4.

[63] M. M. Kirka et al. "Microstructure Development in Electron Beam-Melted Inconel 718 and Associated Tensile Properties". In: *JOM* 68.3 (Mar. 2016), pp. 1012–1020. ISSN: 1543-1851. DOI: 10.1007/s11837-016-1812-6. URL: https://doi.org/10.1007/s11837-016-1812-6.

[64] Ahmad Mostafa et al. "Structure, Texture and Phases in 3D Printed IN718 Alloy Subjected to Homogenization and HIP Treatments". In: *Metals* 7.6 (2017). ISSN: 2075-4701. DOI: 10.3390/met7060196. URL: http://www.mdpi.com/2075-4701/7/6/196.

[65] Shi-Hai Sun et al. "Electron beam additive manufacturing of Inconel 718 alloy rods: Impact of build direction on microstructure and high-temperature tensile properties". In: *Additive Manufacturing* 23 (2018), pp. 457–470. ISSN: 2214-8604. DOI: https://doi.org/10.1016/j.addma.2018.08.017. URL: http://www.sciencedirect.com/science/article/pii/S2214860417303214.

[66] L. Rickenbacher et al. "High temperature material properties of IN738LC processed by selective laser melting (SLM) technology". In: *Rapid Prototyping Journal* 19.4 (2013), pp. 282–290. DOI: 10.1108/13552541311323281. eprint: https://doi.org/10.1108/13552541311323281. URL: https://doi.org/10.1108/13552541311323281.

[67] Radomila Konečná et al. "Microstructure and directional fatigue behavior of Inconel 718 produced by selective laser melting". In: *Procedia Structural Integrity* 2 (2016). 21st European Conference on Fracture, ECF21, 20-24 June 2016, Catania, Italy, pp. 2381–2388. ISSN: 2452-3216. DOI: https://doi.org/10.1016/j.prostr.2016.06.298. URL: http://www.sciencedirect.com/science/article/pii/S2452321616303092.

[68] Yoichi Yamashita et al. "Defect analysis and fatigue design basis for Ni-based superalloy 718 manufactured by selective laser melting". In: *International Journal of Fatigue* 117 (2018), pp. 485–495. ISSN: 0142-1123. DOI: https://doi.org/10.1016/j.ijfatigue.2018.08.002. URL: http://www.sciencedirect.com/science/article/pii/S0142112318303438.

[69] D.B. Witkin, D.N. Patel, and G.E. Bean. "Notched fatigue testing of Inconel 718 prepared by selective laser melting". In: *Fatigue & Fracture of Engineering Materials & Structures* 0.0 (). DOI: 10.1111/ffe.12880. eprint: https://onlinelibrary.wiley.com/doi/pdf/10.1111/ffe.12880. URL: https://onlinelibrary.wiley.com/doi/abs/10.1111/ffe.12880.

[70] Mohamed R. Bayoumi and A.K. Abdellatif. "Effect of surface finish on fatigue strength". In: *Engineering Fracture Mechanics* 51.5 (1995), pp. 861–870. ISSN: 0013-7944. DOI: https://doi.org/10.1016/0013-7944(94)00297-U. URL: http://www.sciencedirect.com/science/article/pii/001379449400297U.

[71] John J. Lewandowski and Mohsen Seifi. "Metal Additive Manufacturing: A Review of Mechanical Properties". In: *Annual Review of Materials Research* 46.1 (2016), pp. 151–186. DOI: 10.1146/annurev-matsci-070115-032024. eprint: https://doi.org/10.1146/annurev-matsci-070115-032024. URL: https://doi.org/10.1146/annurev-matsci-070115-032024.

[72] *Standard Practice for Microetching Metals and Alloys*. Standard ASTM E407-07(2015)e1. West Conshohocken PA: ASTM International, 2015. DOI: https://doi.org/10.1520/E0407-07R15E01.

[73] *Standard Test Methods for Tension Testing of Metallic Materials*. Standard ASTM E8/E8M-16a. West Conshohocken PA: ASTM International, 2016. DOI: https://doi.org/10.1520/E0008_E0008M-16A.

[74] Taylor and Wang. "The validation of some methods of notch fatigue analysis". In: *Fatigue & Fracture of Engineering Materials & Structures* 23.5 (2000), pp. 387–394. DOI: 10.1046/j.1460-2695.2000.00302.x. eprint: https://onlinelibrary.wiley.com/doi/pdf/10.1046/j.1460-2695.2000.00302.x. URL: https://onlinelibrary.wiley.com/doi/abs/10.1046/j.1460-2695.2000.00302.x.

[75] C. Santus, D. Taylor, and M. Benedetti. "Experimental determination and sensitivity analysis of the fatigue critical distance obtained with rounded V-notched specimens". In: *International Journal of Fatigue* 113 (2018), pp. 113–125. ISSN: 0142-1123. DOI: https://doi.org/10.1016/j.ijfatigue.2018.03.037. URL: http://www.sciencedirect.com/science/article/pii/S0142112318301294.

[76] J.-R. Poulin, V. Brailovski, and P. Terriault. "Long fatigue crack propagation behavior of Inconel 625 processed by laser powder bed fusion: Influence of build orientation and post-processing conditions". In: *International Journal of Fatigue* 116 (2018), pp. 634–647. ISSN: 0142-1123. DOI: https://doi.org/10.1016/j.ijfatigue.2018.07.008. URL: http://www.sciencedirect.com/science/article/pii/S0142112318302925.

[77] R. Kelkar et al. "Alloy 718: Laser Powder Bed Additive Manufacturing for Turbine Applications". In: *Proceedings of the 9th International Symposium on Superalloy 718 & Derivatives: Energy, Aerospace, and Industrial Applications*. Ed. by Eric Ott et al. Cham: Springer International Publishing, 2018, pp. 53–68. ISBN: 978-3-319-89480-5.

List of Figures
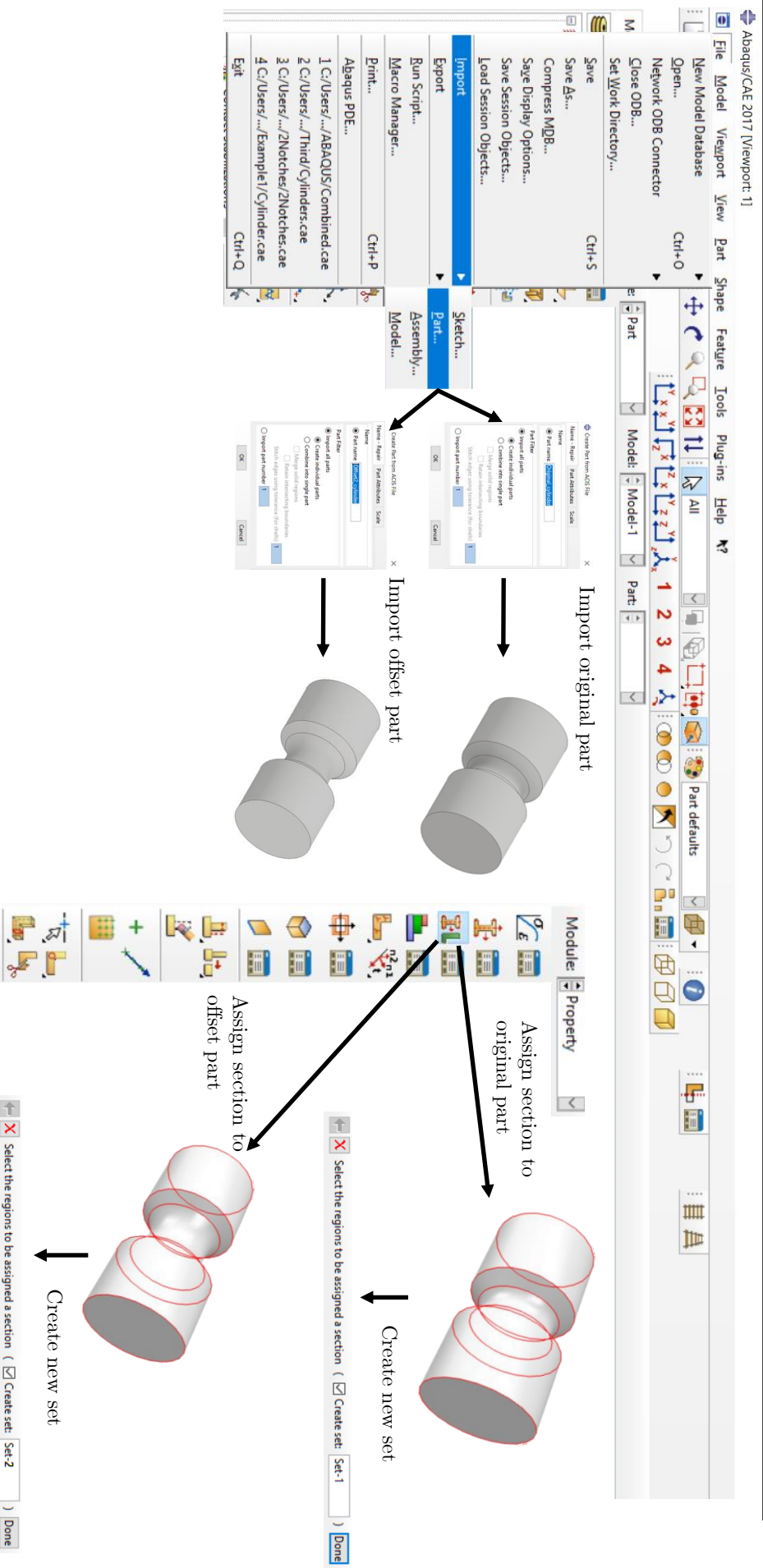
List of Tables

A   Offset Procedure

Creating an offset part in Inventor

The offset part is created by using the Thicken/Offset command and selecting all external faces of the original part. All faces of the original part are selected and distance is selected as inwards. Performing a cut will remove the material outside the offset surface, and the offset part is created. Both the original part and offset part are saved as .sat files for importing to Abaqus. The offset distance is here set to an arbitrary value of 2 mm.

Save original part as .sat file

Select all faces

Perform a cut

Save offset part as .sat file
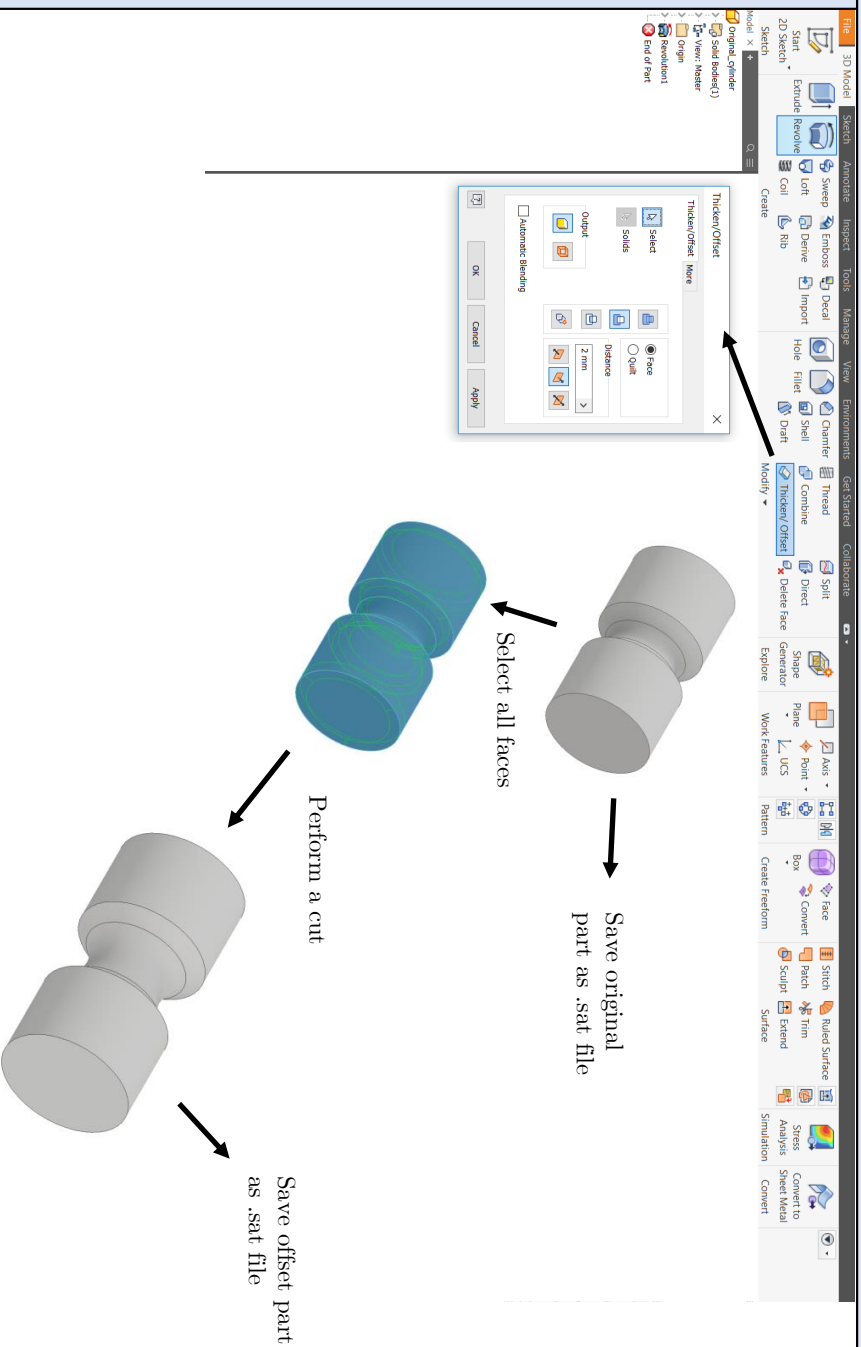
Importing parts and assigning sections in Abaqus

Having saved the original and the offset part as .sat files, the parts are imported to Abaqus as individual parts. In the property module, the parts are assigned sections individually, and a new set is created for each section.


Import offset part

Import original part

Assign section to offset part

Assign section to original part

Create new set

Create new set

Creating a partitioned part in Abaqus

After assigning sections to both the original and the offset part, the parts are merged in the Assembly module. First, a new instance is created based on the two parts. After creating a new instance, a combined part is created by using the Merge/Cut Instances command. It is important that the intersecting boundaries are retained. This step creates a partition surface at the offset distance, which makes sure that the elements follow this surface when the combined part is meshed. The combined part is identical to the original part, with the partition surface as the only difference.

New instance
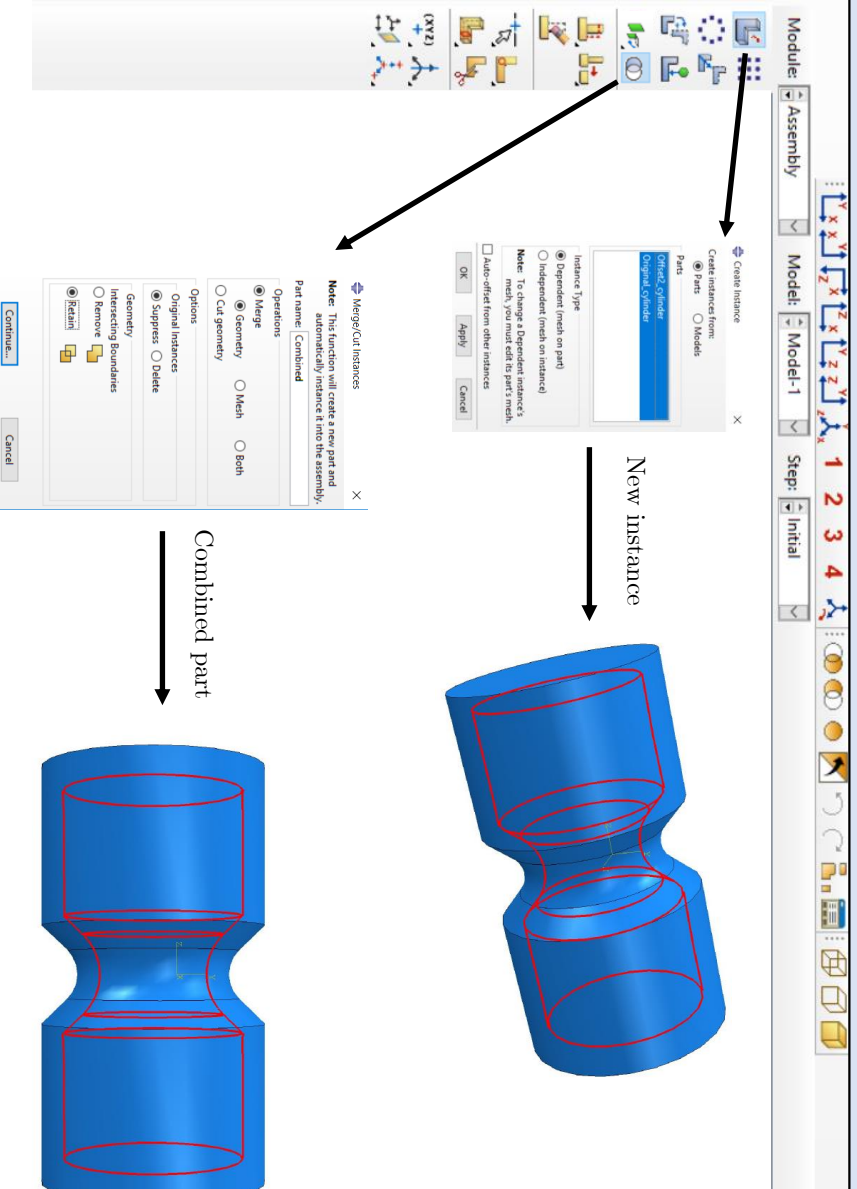
Combined part
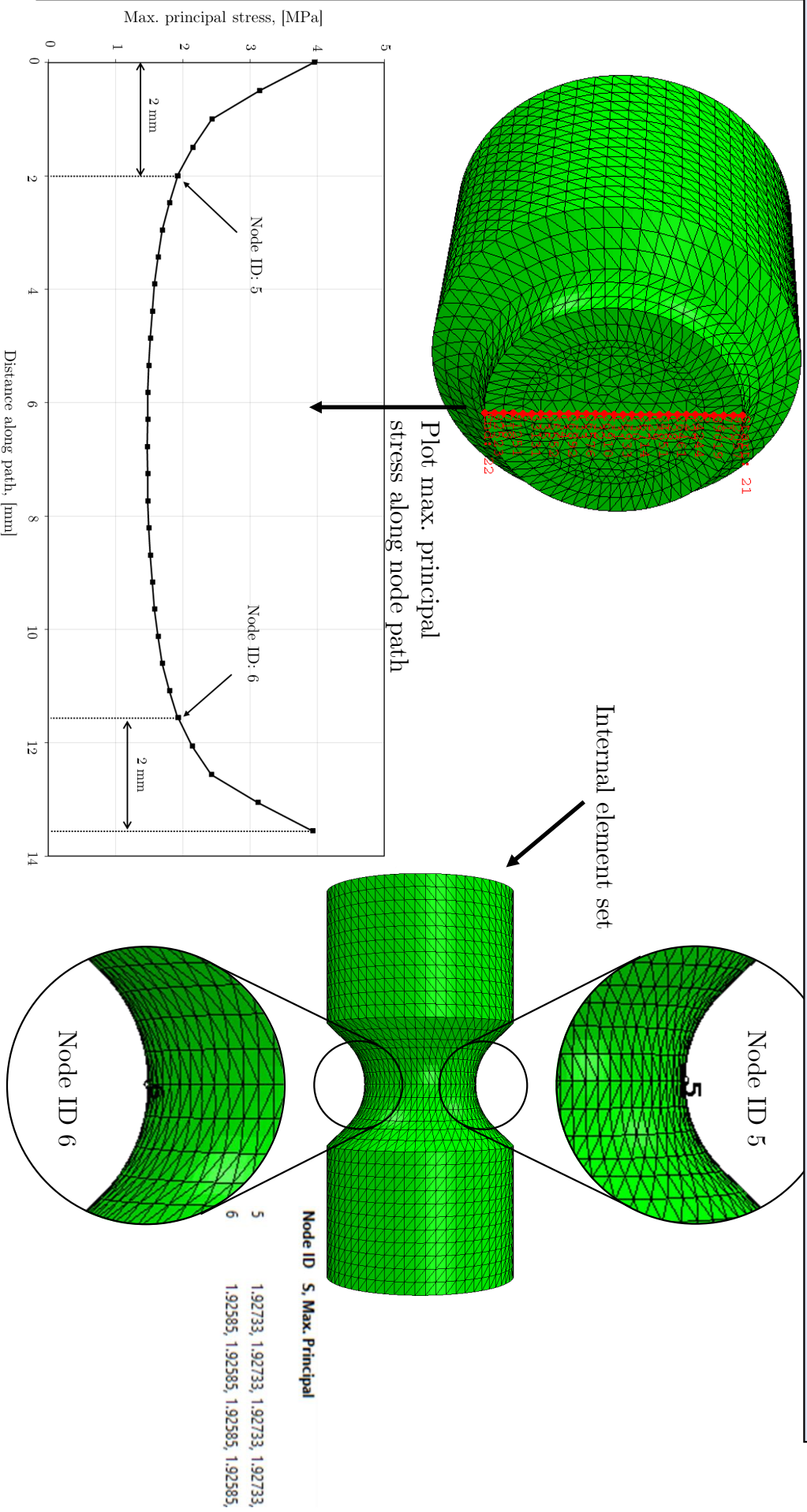
Analyzing the combined part in Abaqus

After meshing the combined part, the part can be subjected to the desired loads, and the resulting stresses can be analyzed in the visualization module. In order to study the stresses at the offset distance from the surface, the external element set can simply be removed. The element sets created by the partition procedure are available in the Output Databases.

Element sets without stresses

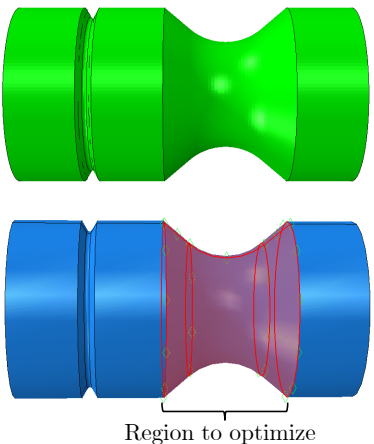Element sets with stresses

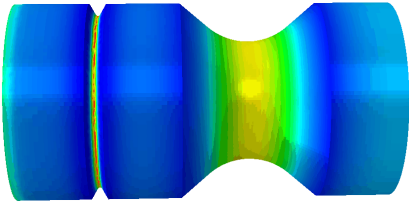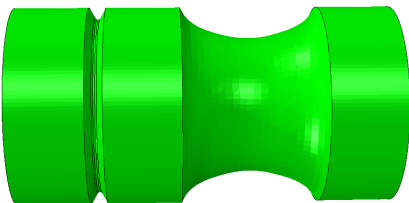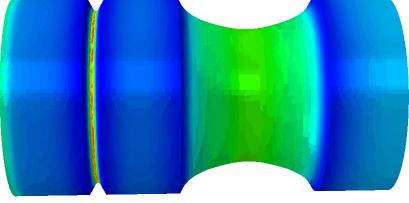COMBINED-1.SET-1
COMBINED-1.SET-2
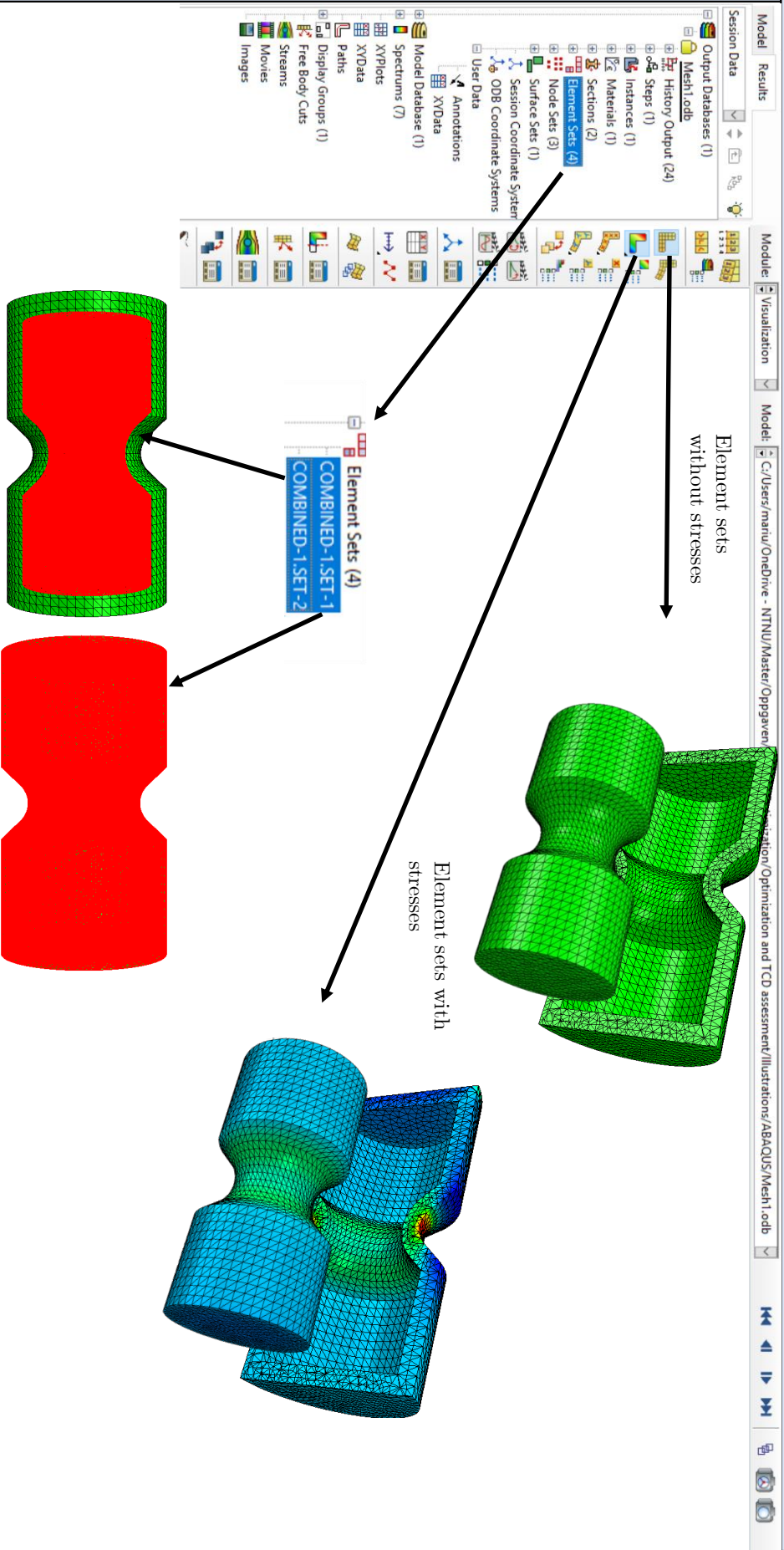
In order to verify that the offset procedure gives a correct representation of the stresses at the desired offset distance, a node path is created in the smallest cross section of the original part. The max. principle stresses are plotted for the entire node path with an applied unit load, and the nodes at the offset distance of 2 mm are identified. The ID's of these two nodes are 5 and 6.

The same nodes are found on the surface of the internal element set, with the same stresses as in the node path plot, indicating that the offset procedure is able to correctly represent the stresses at the offset distance. The stresses on node 5 and 6 are found by using the Probe function.
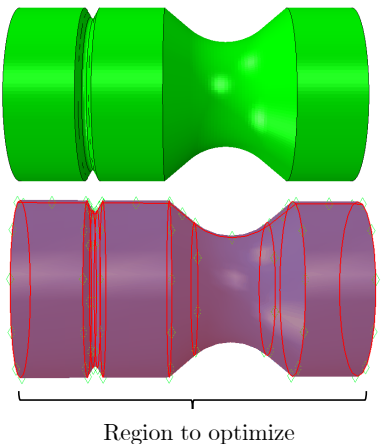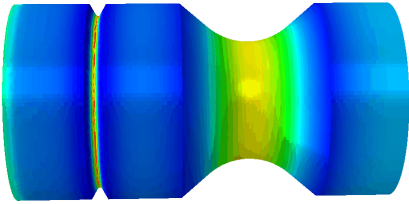

Plot max. principal stress along node path

Internal element set

Node ID 5

Node ID 6

Node ID 5

Node ID 6

Node ID	S, Max. Principal
5	1.92733, 1.92733, 1.92733, 1.92733,
6	1.92585, 1.92585, 1.92585, 1.92585,
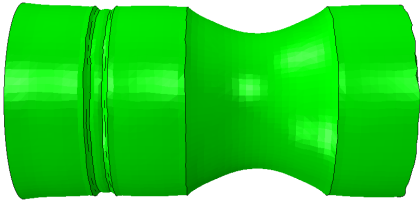
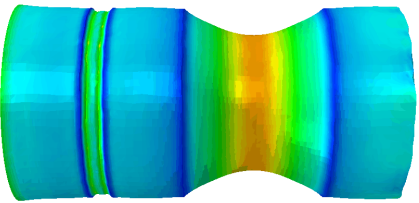# B Shape Optimization

B.1 Optimization of the Critical Notch

	Part	Stress	Optimization process
Original part	Region to optimize		**Number of iterations:** 10 **Change in volume:** 0 % **Elapsed time:** 105 min **Reduction in max stress:** Sharp notch: 0 % Blunt notch: 26 %
Optimized part			

B.2 Optimization of Entire Cylinder

	Part	Stress	Optimization process
Original part	Region to optimize		**Number of iterations:** 10 **Change in volume:** 0 % **Elapsed time:** 194 min **Reduction max in stress:**
Optimized part			Sharp notch: 47 % Blunt notch: 26 %

C   Mesh Sensitivity of Offset Procedure
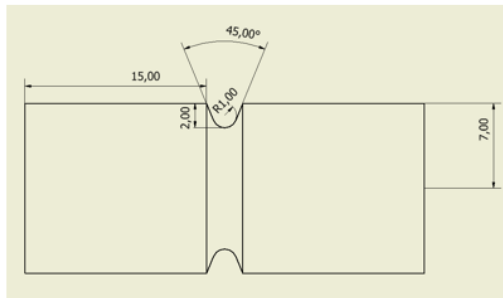
a) Cylinder Dimensions
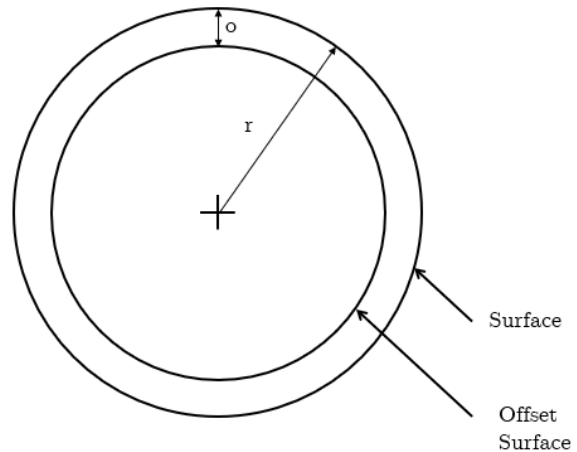
b) Smallest Cross Section of Cylinder

Figure C.1: Cylinder used for mesh sensitivity analysis. a) shows dimensions of cylinder. b) shows smallest cross section of cylinder where stresses are measured. Outer surface, offset surface, offset distance, o, and radius, r, are indicated.

Table C.1: Stresses at surface and offset surface of cylinder for different mesh sizes and offset distances.

| | o/r=0.2 | | | o/r=0.16 | | | o/r=0.12 | | | o/r=0.08 | | |
| | Max. Principal Stress [MPa] | | | Max. Principal Stress [MPa] | | | Max. Principal Stress [MPa] | | | Max. Principal Stress [MPa] | | |
Mesh Size	Surface	Offset Surface	Distorted Elements	Surface	Offset Surface	Distorted Elements	Surface	Offset Surface	Distorted Elements	Surface	Offset Surface	Distorted Elements
5	3.333	2.677	142									
4.5	3.173	2.000	84	3.466	2.151	204	9.073	2.536	362			
4	3.009	2.047	63	3.710	2.746	149	6.063	2.657	324	6.639	2.406	434
3.5	2.998	2.142	52	3.036	2.043	64	4.589	2.672	247	3.671	2.285	299
3	7.523	1.871	5	2.781	2.017	128	2.929	2.216	169	3.473	2.265	201
2.5	7.645	1.948	9	7.883	2.084	6	8.264	2.406	45	6.130	1.870	10
2	7.653	1.945	7	7.951	2.108	8	8.373	2.371	23	6.382	2.316	20
1.5	4.457	1.937	0	5.299	2.090	0	4.843	2.338	8	4.871	2.491	0
1	4.748	1.974	0	4.979	2.115	0	4.936	2.337	0	4.824	2.564	9
0.8	4.786	1.923	7	4.749	2.158	30	4.861	2.390	9	5.090	2.533	10
0.6	4.980	1.936	4	4.941	2.095	0	4.957	2.387	0	4.901	2.528	3
0.4	4.939	1.921	5	4.902	2.07	1	4.931	2.341	1			

Marius Hornnes

Master's Thesis at NTNU

NTNU
Norwegian University of
Science and Technology